UNIVERSIDADE FEDERAL DO CEARÁ
CENTRO DE CIÊNCIAS
DEPARTAMENTO DE FÍSICA
PROGRAMA DE PÓS-GRADUAÇÃO EM FÍSICA

FRANCISCO WELLERY NUNES SILVA

STRUCTURAL, ELECTRONIC AND TRANSPORT PROPERTIES OF NANOSCALED SYSTEMS

FORTALEZA

2016

FRANCISCO WELLERY NUNES SILVA

STRUCTURAL, ELECTRONIC AND TRANSPORT PROPERTIES OF NANOSCALED SYSTEMS

Tese de Doutorado apresentada ao Programa de Pós-Graduação em Física da Universidade Federal do Ceará, como requisito parcial para a obtenção do Título de Doutor em Física. Área de Concentração: Física da Matéria Condensada.

Orientador: Prof. Dr. Eduardo Bedê Barros

FORTALEZA
2016

FRANCISCO WELLERY NUNES SILVA

STRUCTURAL, ELECTRONIC AND TRANSPORT PROPERTIES OF NANOSCALED SYSTEMS

Tese de Doutorado apresentada ao Programa de Pós-Graduação em Física da Universidade Federal do Ceará, como requisito parcial para a obtenção do Título de Doutor em Física. Área de Concentração: Física da Matéria Condensada.

Aprovada em 26/08/2016.

BANCA EXAMINADORA

Prof. Dr. Eduardo Bedê Barros (Orientador)
Universidade Federal do Ceará (UFC)

Prof. Dr. Andrey Chaves
Universidade Federal do Ceará (UFC)

Prof. Dr. João Milton Pereira Junior
Universidade Federal do Ceará (UFC)

Prof. Dr. Eduardo Costa Girão
Universidade Federal do Piauí (UFPI)

Profa. Dra. Andrea Brito Latge
Universidade Federal Fluminense (UFF)

Dados Internacionais de Catalogação na Publicação
Universidade Federal do Ceará
Biblioteca Universitária
Gerada automaticamente pelo módulo Catalog, mediante os dados fornecidos pelo(a) autor(a)

S58s Silva, Francisco Wellery Nunes .
Structural, Electronic and Transport Properties of NanoScaled Systems / Francisco Wellery Nunes Silva. – 2016.
94 f. : il. color.

Tese (doutorado) - Universidade Federal do Ceará, Centro de Ciências, Programa de Pós-Graduação em Física, Fortaleza, 2016.
Orientação: Prof. Dr. Eduardo Bedê Barros

1. DFT. 2. Electronic Structure. 3. Graphene. 4. nanoribbon. 5. MoS2. I. Título.

CDD 530

"If your wish is to become really a man of science, and not merely a petty experimentalist, I should advise you to apply to every branch of natural philosophy, including mathematics."
Mary Shelley

ACKNOWLEDGMENTS

I thank mom and dad...

I thank professor Eduardo Bedê Barros, for all his patience and advices given to me over the last years.

I thank Dr. Eduardo Cruz-Silva, for all his time and patience, during the time in which we worked together at PSU.

I thank professor Mauricio Terrones, for allowing me to join his group and helping me during my time at PSU.

I thank professor Humberto Terrones for every orientation and advices along all this time.

I thank professor Antônio Gomes de Souza Filho, for all support and comprehension and for all advices and orientations as well along my journey at UFC.

I thank "shihan" Josué Mendes Filho, for a life dedicated to this department, and for every thing which I have learned just observing him, who is a truthful master.

I thank professor Alexandre Araújo Costa, who gave me indispensable support in a crucial moment of this step.

I thank Dr. Peter Koval for all good conversations about the SIESTA method.

I thank Dr. Andrei Postnikov for every tool shared for him, and for precious advices about the SIESTA method.

I thank professor Eduardo Costa Girão, for allowing our group to use his transport program.

I thank my room mates, Rafael, Bruno and of course Bruno "senpai", for every happy moment which came from a joke.

I thank Centro Nacional de Super Computação CESUP, for every computational support.

I thank Centro Nacional de Processamento de Alto Desempenho em São Paulo, for computational support.

I thank Coordenação de Aperfeiçoamento de Pessoal de Nível Superior CAPES, for all Financial support.

Pesquisa desenvolvida com o apoio do Centro Nacional de Supercomputação (CESUP), Universidade Federal do Rio Grande do Sul (UFRGS).

RESUMO

Métodos para cálculos de estrutura de banda são aplicados neste trabalho, a fim de estudar as propriedades eletrônicas e de transporte de sistemas em nanoescala. A teoria do funcional da densidade (DFT) foi empregada para estudar as propriedades eletrônicas de uma ilha hexagonal de nitreto de boro (h-BN) embutida em nanofitas de grafeno (GNRs), considerando ambas as quiralidades de bordas, zigzag e armchair. Além disso, a contribuição do spin foi levada em conta no nosso cálculo eletrônico. Os resultados referentes aos sistems não dopados mostraram a existência de uma polarização de spin natural associado a sistemas de borda zigzag, enquanto os sistemas de borda armchair são encontrados com spin degenerados no estado fundamental. Nós também investigamos os efeitos devido à dopagem com carbono no anel mais interno de um cluster de h-BN, onde o átomo C toma o lugar de um átomo de Boro ou de um átomo de Nitrogênio. A dopagem conduz a uma estrutura de bandas ainda mais polarizada, para energias próximas ao nível de Fermi. As propriedades de transporte eletrônico foram estudadas aplicando o formalismo de Landauer-Büttiker, para todos os sistemas propostos, e a condutância quântica também apresenta uma dependência de spin. Uma aplicação dos sistemas, como sensores moleculares dependentes de spin também é considerada. Nós adsorvemos diferentes moléculas em dispositivos ricos/deficientes de elétrons e observamos que a condutância eletrônica pode ser modulada por esses sistemas moleculares. Além disso, a fim de verificar a estabilidade termodinâmica dos sistemas adsorvidos realizamos cálculos de dinâmica molecular sob o algoritmo de termostato proposto por Nosé . Nessa tese, nós também estudamos as propriedades eletrônicas dos metais de transição dicalgogenados (TMDCs) por meio do método *tight-binding* como proposto por Slater-Koster, aplicado à estrutura eletrônica. As propriedades de transporte eletrônico das nanofitas de dissulfeto de molibdênio (MoS_2NRs) são consideradas, e os nossos resultados mostram que as bordas das fitas desempenham um papel importante no quadro da condutância. Os nossos resultados mostram que mesmo um pequeno defeito devido a falta de um trío de MoS_2 na borda é suficiente para levar a uma forte supressão da condutância ao longo do sistema. Além disso, efeitos de interferência devido aos defeitos, sugerem que MoS_2NRs podem ser aplicadas como nanodiodos.

Palavras-chave: DFT Estrutura Eletronica Grafeno nanoribbonMoS2

ABSTRACT

Band structure methods are applied in this work in order to study electronic and transport properties in nano-scaled systems. Density Functional Theory (DFT) has been employed in order to study the electronic properties of a hexagonal island of boron nitrite (h-BN) embedded into graphene nanoribbons (GNRs) in both edge chiralities, zigzag and armchair. Furthermore, in our electronic calculation the spin contribution has been taken into account. The results regarding the non-doped systems revealed that a natural spin splitting is associated to the zigzag edged systems, while the armchair one is found to have a spin degenerated ground state. We also investigate the effects due carbon doping in the innermost ring of the h-BN cluster, where the C atom take the place either the Boron or Nitrogen atom. The doping lead to an even more polarized band structure, for energies nearby the Fermi level. The electronic transport properties have been studied applying the Landauer-Büttiker formalism, for all proposed systems, and the quantum conductance also exhibit a spin dependence. An application of the systems, as spin dependent molecular sensors is also considered. We have adsorbed different molecules onto electron rich/deficient devices and observed that the electronic conductance may be modulated by those adsorbed systems. Also, in order to verify the thermodynamic stability of the adsorbed systems we have performed Molecular Dynamics calculations under the Nosé thermostat algorithm. In this thesis, we also have studied the electronic properties of the transition metal dichalcogenides (TMDCs) by means the Slater-Koster tight-binding method for the electronic structure. The electronic transport properties of molybdenum disulfide (MoS_2) nanoribbons (MoS_2-NR) is considered, and our results show that the edges of the ribbons play an important role in the conductance framework. Our results show that even a small defect due the lack of a MoS_2 triplet in the edge is sufficient to lead to a strong suppression of the conductance over the system. Furthermore, interference effects due to defects suggest that MoS_2-NR may be applied as nano-diodes.

Keywords: DFT Electronic Structure Graphene nanoribbon MoS2

LIST OF TABLES

LIST OF FIGURES

CONTENTS

1 INTRODUCTION

In view of the splendid technological development of the world one of the question that arises is how is it possible to maintain the current rate of advances in the electronic based industry. These advances are expected to reach a limit soon, as the silicon based technology development departs from Moore's law. Many research groups around the world have been worked strongly to answer this question, and one promising way seems to be through the carbon based technology. The paper by Kroto *et al* [4] published in 1985 is remarkable because we can say that the research in carbon nano-structures had its beginning from that point.

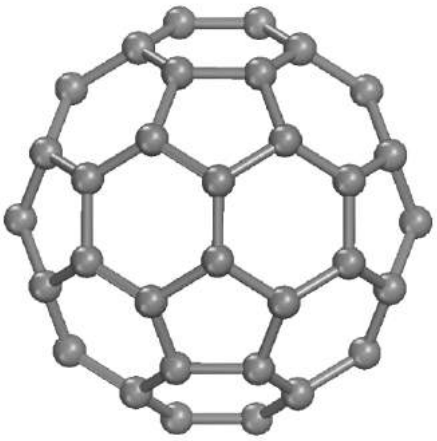

Figure 1: Fullerene Molecule C_{60} with a soccer ball format proposed by Kroto *et al* in 1985, in his paper where they assume that carbon prefer to be in C_{60} form, as observed in their mass spectroscopy measurements.

Few years after Kroto's seminal paper, another carbon allotrope was highly studied, the carbon nanotubes observed by Sumio Ijima [1], in 1991. This is another remarkable point in the nanotechnology world, since this quasi-unidimensional crystal showed promising physical properties. In a didactic model, the carbon nanotube may be understood as a single graphite layer rolled up to form a cylindrical structure, known as single walled carbon nanotube (SWCNT).

Following Ijima's paper, many articles about carbon nanotubes have been published, proposing different applications in several areas, including biological applications [5] and many other applications in physics and chemistry. Another perspective to industry usage for carbon nanotubes was proposed by Tans *et al* [6], where they manufactured a transistor based in a single walled carbon nanotube, working at room temperature. Results showed in Ref. [6] show that it is possible to use the great electronic properties of carbon nanotubes (CNTs) for the miniaturization of this kind of devices. This will be

Figure 2: Schematic representation of a singlewalled Carbon nanotube, Like the structural model proposed by Ijima in 1991 ref. [1].

the main topic of this thesis, the search by new nanostructures in which the electronic properties may be applied in novel types of electronic devices or which may be useful in the newly emerging area of spintronics [7].

1.1 The Graphene Systems

The year was 2004, when a paper by Novoselov *et al* [8], employing the scotch tape method for exfoliation, demonstrated the existence of a single graphite layer, the so called graphene. Such monoatomic thin layer formed only by carbon atoms, is endowed with surprising physical properties, such as high electrical and thermal conductivities as observed experimentally. Since the beginning of the 2000's, graphene has been the gold mine for many researches, in physics and chemistry especially.

Graphene is a remarkable material because it was the first 2D crystal to overcome the Mermin-Wagner theorem, which states that a 2D crystal looses its long-range order, thus melting the entire lattice, under any temperature above zero K, due to thermal fluctuations. However, what facts are behind graphene's interesting properties? To answer this question we should first look at the carbon atom. Carbon can be hybridized in three different forms, sp^1, sp^2 and sp^3. Here we will take into account just the sp^2 hybridization, which is the one in which graphene is found to be. In that case the orbital 2s and two components of 2p are superposed, where we can represent them in the Dirac notation as $|2p_x\rangle$ and $|2p_y\rangle$ states, in such way that we obtain a planar hybridization. Thus the three quantum-mechanical states are given as following:

$$|sp_1^2\rangle = \frac{1}{\sqrt{3}}|2s\rangle - \sqrt{\frac{2}{3}}|2p_y\rangle$$

$$|sp_2^2\rangle = \frac{1}{\sqrt{3}}|2s\rangle + \sqrt{\frac{2}{3}}\left(\frac{\sqrt{3}}{2}|2p_x\rangle + \frac{1}{2}|2p_y\rangle\right)$$

$$|sp_3^2\rangle = -\frac{1}{-\sqrt{3}}|2s\rangle + \sqrt{\frac{2}{3}}\left(\frac{\sqrt{3}}{2}|2p_x\rangle + \frac{1}{2}|2p_y\rangle\right)$$

These orbitals are oriented in the xy-plane and they have a 120^o angle separation between each other. Because of this hibridization, graphene is condensed in a honeycomb lattice, on which the two neighboring carbon atoms are not equivalent, what leads graphene to have a non-Bravais lattice. Indeed we can consider graphene as being composed of two triangular Bravais lattices intertwined, they are the sublattices **A** and **B** [9, 10]. The distance between two subsequent carbon atoms is 1.42 Å, this value is approximately an average of a single carbon bond C-C and a double carbon bond C=C distances.

The three vectors which connect an atom in lattice **A** to the other in the lattice **B** are given by:

$$\vec{V_1} = \frac{a}{2}\left(\sqrt{3}\hat{i} + \hat{j}\right) \qquad \vec{V_2} = \frac{a}{2}\left(-\sqrt{3}\hat{i} + \hat{j}\right) \qquad \vec{V_3} = -a\hat{j}$$

And the real space lattice vector which span the graphene's hexagonal lattice are expressed as,

$$\vec{a_1} = \left(\frac{\sqrt{3}}{2}a\hat{i}, \frac{a}{2}\hat{j}\right) \qquad \vec{a_2} = \left(\frac{\sqrt{3}}{2}a\hat{i}, -\frac{a}{2}\hat{j}\right)$$

Where a=$|\vec{a_1}| = |\vec{a_2}| = 1.42 \times \sqrt{3} = 2.46$ Å, this value is the lattice constant for two dimensional graphite. In Figure 3 we can see the schematic view of sp^2 hybridization as well as for the honeycomb lattice.

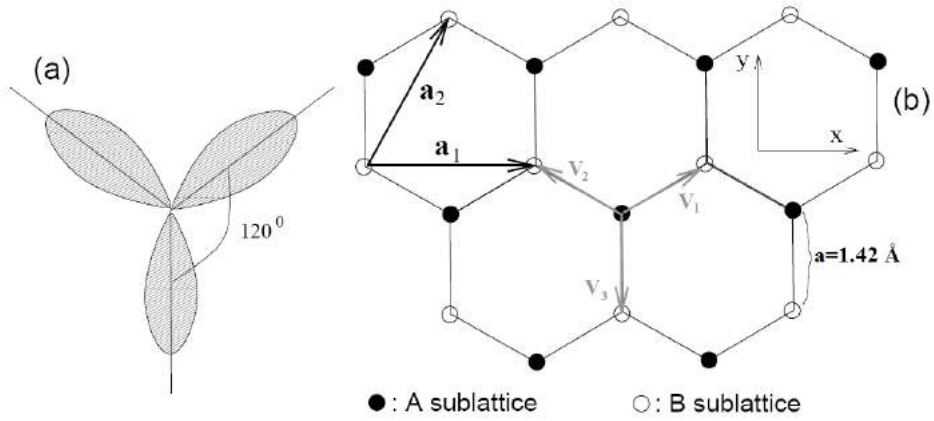

Figure 3: a) representation for atomic orbitals in the sp^2 hybridization for carbon case, which has a 120^o between each other. b)Honeycomb lattice, the vectors V_1, V_2 and V_3 are connecting an atom in the sublattice **A** with it's neighbours in the sublattice **B** separated by a distance of 1.42 Å. The vectors a_1 and a_2 are the base vectors which span the graphene structure.

Graphene is catalogued as a semi-metal, since it has a zero gap at k-point

of its hexagonal Brillouin zone. Also, a linear energy-momentum dispersion around what is called Dirac cone [11] is observed. Because of this property, low energy electrons in graphene may behave like relativistic particles [12, 13] thus allowing graphene to show outstanding ballistic transport properties, with a long coherence length, which makes graphene an excellent platform for studying many physical phenomena. Therefore, graphene is known to have a very high measured carrier mobility, up to $15 \times 10^2\ cm^3/Vs$ [14]. In addition to this, graphene still has a high Young's modulus and strength and its thermal conductivity is comparable to those associated to carbon nanotubes [15–17].

All those outstanding properties associated to graphene places this 2D-crystal among the most promising materials candidates for replacing silicon in electronic applications for the future. In such asin devices like high frequency transistors, supercapacitors or touch screens [18]. However a pristine graphene sheet have no band gap as we can see in the band structure plot depicted in Figure 4.

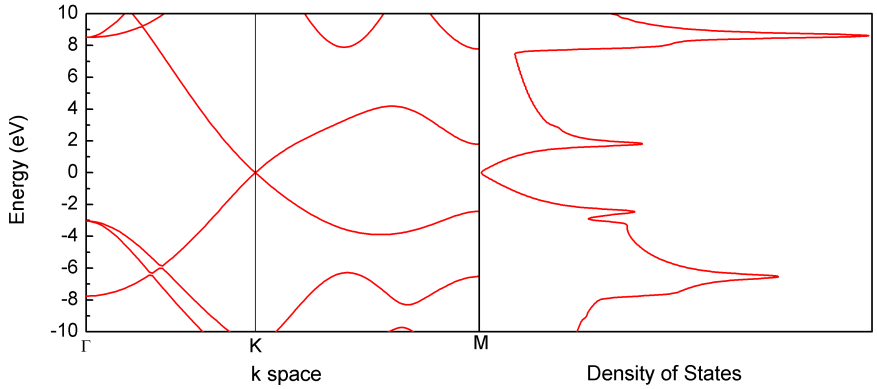

Figure 4: Graphene band structure in the k-space and the respective Density of States, calculated using the Density Functional Theory (**DFT**). The Fermi energy was set up in the zero.

We can observe the link between the valence band and conduction band, exactly in the **K** point in the reciprocal space. Since many electronic devices interesting for technological applications are dependent of a switching character, the absence of a band gap in graphene is not desirable for some relevant applications, such as in transistors situation. Then for a real use of graphene in electronic applications, something must be done to find out a way to open a band gap in graphene based systems.

1.1.1 Graphene Nanoribbons

There are many ways to open the gap in a graphene system, such as chemical, mechanical, and topological methods. If you take an ideal graphene sheet and make it in strips with a very narrow finite width and infinite along the perpendicular direction,

a graphene nanoribbon is built. Theoretical calculations have predicted that this kind of carbon structure exhibit electronic properties which make them attractive for the fabrication of nanoscale devices [19, 20]. It is also known in the literature, that the size of the energy gap and ribbon width are inversely proportional to each other [21, 22], and also depend on the chemical nature of the edges of the ribbon. This limits the range of widths for which the semiconducting behaviour is found. In general, graphene nanoribbons with widths smaller than ten nanometers are able to show semiconducting properties [2].

The edge termination exerts a strong influence in nanomaterials. The two most studied types of edge terminations in the graphene nanoribbon are the zigzag graphene naonoribon (**ZGNR**) and armchair graphene nanoribbon (**AGNR**) [23]. Figure 5 depicts an exemplification of these structures. In order to perform calculations based in this kind of periodic structure, periodic boundary conditions are usually applied.

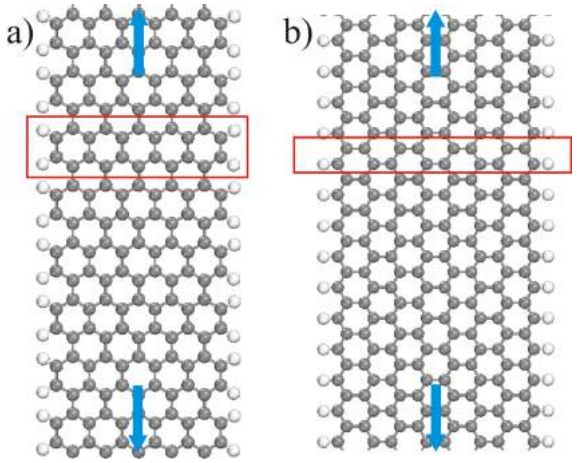

Figure 5: a) Periodic AGNR the arrows indicate the continuousness, and the red box shows the unit cell for computation. b) The ZGNR depicted as in the previous case.

From the experimental point of view, there are several methods to fabricate a GNR including unzipping a carbon nanotube, lithographic methods, and recently a chemical method based in an intermolecular colligation using polymers as precursors for the bottom-up fabrication, have been proposed, as presented in Ref. [23]. The paper by Cai and co-workers opened precedents for the fabrication not only of a linear GNR, but also for, other types of configurations such as Chevron-type structure and the junction of two or more ribbons.

Figure 6 depicts STM images for several structures obtained via chemical synthesis, from Ref. [23]. For these systems the advances in the experimental field have been reached in the last few years, the fabrication of ribbons with width below 10 nm, configure nowadays a significant challenge to material engineering. Thus the exploration of electronic properties of graphene nanoribbons is hampered by this limitation.

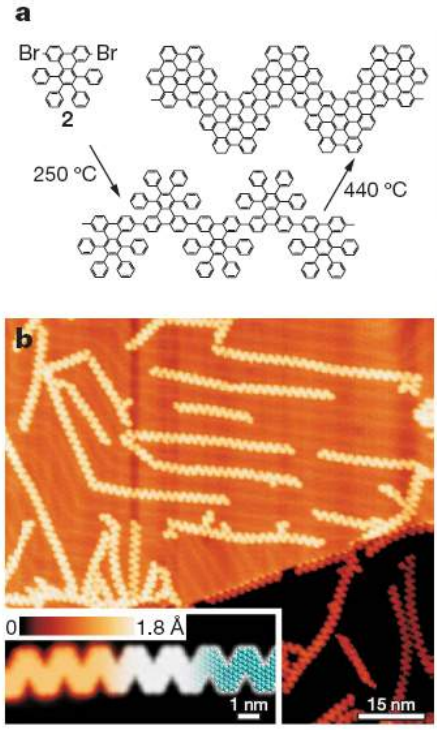

Figure 6: a) Reactions scheme using 6,11-dibromo-1,2,3,4-tetraphenyltriphenilene monomer passing by different temperatures to form a new GNR. b) STM images containing several Chevron-type GNRs, adapted from Ref. [2]

1.2 Boron Nitride

Boron Nitride **BN** is found in nature, in several different structural configurations, such as diamond like, cubic, wurtzite and also in a hexagonal phase similar to that of the graphite, called hexagonal boron nitride, **h-BN**. It is in the last structure that lies the focus of this work, Boron and Nitrogen forming covalent bonds. However there is a considerable difference in the Pauli electronegativity between the two atoms, thus this bond has some ionic features, existing an intrinsic electric dipole though the bonding. This leads to a charge transfer, where the electrons tend to be more localized in N atom. Moreover h-BN is known to have a huge electronic gap of the order of 5-6 eV [24]. The first applications of BN date from the 1940's, in the cosmetic industry [25], as lubricants, due to its high stability at room temperature and due to its insulating properties, being useful as a substitute for graphite [26]. Chemical vapor deposition **CVD** growth of h-BN has been reported since the 70's [27] and the primary evidence about single layer h-BN dates from 1990 [28].

The atomic structure for h-BN monolayer is very similar to the graphene case, and can be compared by Figure 3 b), however, the bond length for B-N is around 1.45 Å and the lattice parameter for the primitive cell is close to the graphene case. Indeed in

h-BN composites the B atom is found at a sp^2 hybridization and regarding the primitive cell of both cases, they are isoelectronic, containing 12 electrons. In geometrical picture a h-BN single layer has an energy gap larger than the bulk phase for this material, once the Van der Waals interaction is missing.

In Figure 7 we can see a plot of Density of States (DOS) for an infinite h-BN sheet. The gap presented in that calculation is 5.80 eV, where it has been predicted by an *ab-initio* calculation. All those characteristics mentioned previously, makes h-BN a very good insulator in relation to graphene or even the ideal substrate for the latter. After the successfully growth of a pristine h-BN single layer, other geometrical configurations became possible, like the boron nitride nanoribbons BNNRs, boron nitride nanotubes BNNT, nanocages and other, which brought a enormous possibilities of technological applications to this material. As graphene, h-BN also have many physical properties very interesting, such as half metallicity which is a property very desired for spintronics purposes.

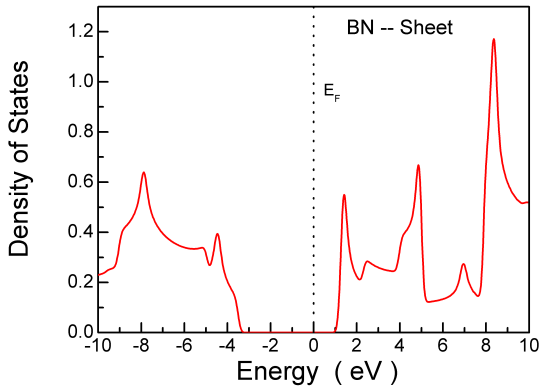

Figure 7: DOS of a BN sheet carried out using DFT method and under GGA picture. Here we can see the huge electronic gap presented by this 2D crystal. It has made BN a good ultra-violet light emitter [3]

Nowadays even hybrid systems composed by B, N and C atoms have its electronic and transport properties being studied, and it is very promising since experimental data, points to the possibility of constructing hetero-junctions between graphene and h-BN [29, 30]. However, once an infinite sheet is just an approximation, its necessary to study systems with a finite size, in different shapes. It is known, that some triangular islands of h-BN are more stable in a certain configuration than other. Symmetric shapes also are important, especially the hexagonal clusters of h-BN. When we are regarding on finite systems the edges also plays an important role, because its chemical activity when a dangling bond is present. In that point many times a passivation brings new and interesting characteristics in relation to the bare system.

Using passivation it is possible to change the electronic properties of these materials, as inserting new electronics states inside the gap for example. Among many possibilities to interfere in the electronic properties, the insertion of heteroatoms and topological defects like Stone-Wales open the horizons for several physics which are not known in this present times. Another point where passivation is important for flat systems, lies in the fact that without dangling bond saturation the geometric reconstruction takes place [31, 32], and such effect is not so interesting for some device applications. It reflects strongly in the band gap engineering of this kind of material, since switching devices for example, require the existence of a band gap. Therefore materials based on h-BN, like those shown in Figure 8 have been received more and more attention, in condensed matter research under a theoretical point of view or even in a experimental way, since the laboratory techniques are in constant improvement, like CVD method, which is seen as a promising tool, for growing such nanomaterials in a large scale framework.

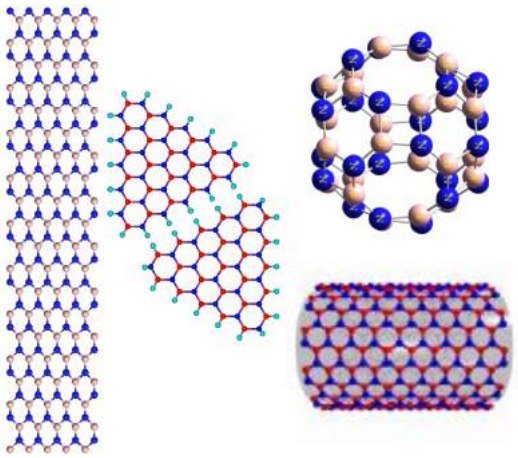

Figure 8: Some nanostructures based on Boron Nitride which can be eventually applied in a such electronic/opto-electronic device, or even spintronics can be explored in the systems, by means of gap modulation using an external electric field.

1.3 Transition Metal Dichalcogenides (TMDCs)

Graphene and boron nitride are not the only examples which we might refer among the vast family of materials that can be peeled off from its bulk phase into few or single layers. Several examples from the transition metal dichalcogenides (TMDCs) set might be cited. These are Van Der Waals stacked crystals in which several layers of the same material form the whole bulk structure. Each mono-layer is formed by three atomic layers, where a transition metal is placed in the middle of two other chalcogen layer, as illustrated in Figure 9. Generically, TMDCs are represented by the MX_2 formula, where M stands by the metal, while X for the chalcogen atom. More than forty species compose

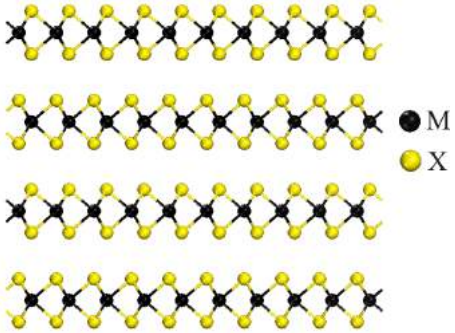

Figure 9: General staking of a TMDC in the trigonal prismatic phase. The black sphere represent the metal, the yellow refers to the chalcogen atom.

the TMDCs group [33], and from the electronic point of view, they show elements with insulating character such as HfS_2, passing by the semiconductors like, MoS_2, to the fully metallic as in the NbS_2 case [33]. We have focused this work on the semiconductor ones, in special on the molybdenum disulfide (MoS_2) and tungsten diselenide (WSe_2), since our research aims to model and propose new possibilities for semiconducting devices.

MoS_2 has been studied both experimentally and theoretically. In its bulk form MoS_2 is known to possess an indirect band gap or approximately 1.2 eV according to density functional theory calculations [34]. It is also predicted theoretically that a transition from indirect to direct gap is found from the bulk form to the monolayer [34]. Such prediction is confirmed by experiments, it has been found a strong photoluminescence associated to the monolayer case [35]. Furthermore recent experiments using the angle-resolved photoemission spectroscopy (ARPES), where further confirm the direct band gap for the single layer MoS_2 [35], with a theoretical value of 1.9 eV [34]. Geometrically identical to MoS_2, WSe_2 also presents an indirect to direct transition in its bulk form to monolayer, however WSe_2 is found to present a smaller band gap in its single layer form than MoS_2, approximately 1.6 eV [36]. Furthermore, WSe_2 exhibits a better electronic transport when compared to MoS_2, since its carrier mobility is said to be higher than the later case. More than this WSe_2 is also more resistant to oxidation in humid atmospheres that MoS_2 [37], which converts WSe_2 in an interesting candidate for future practical applications.

The TMDCs are very sensitive to the geometrical arrangement of the atoms, in special those specimens discussed here so far. Despite showing a semiconducting character in the hexagonal 2H (trigonal prismatic) phase, the electronic structure of MoS_2 and WSe_2 changes drastically from the 2H to the octahedral 1T phase, where they turn to metallic behaviour [36, 38]. The geometries for monolayer of both phases are shown in Figure 10. The coexistence of both phases in the same sample [36, 38] of these two materials is promising, since by means of nanofabrication techniques, it would be possible

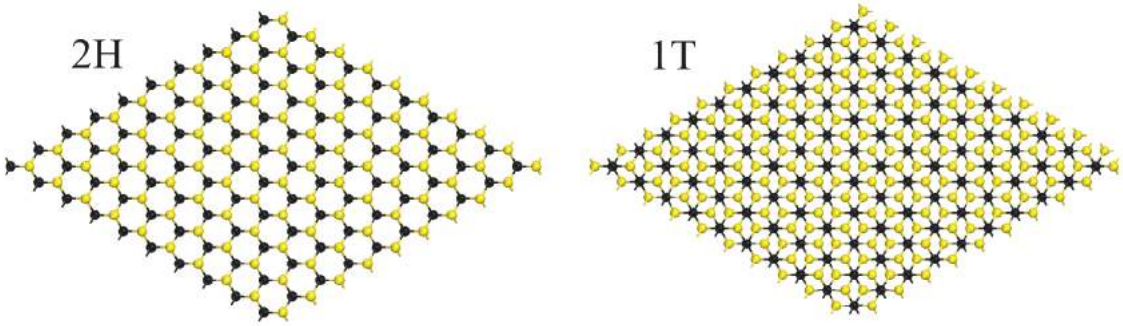

Figure 10: 2H and 1T phases of a generic TMDC.

in the future, engineering a device where a semiconductor is placed between metallic contacts, having the same active material, for instance MoS_2 or WSe_2, thus theoretically reducing the effects from the coupling between metal/semiconductor, which are usually faced in the actual mode of nano-production.

2 THEORETICAL BACKGROUND

The theoretical model approach employed for calculating the electronic structure of the materials studied in this work are discussed in this chapter. It is known that solving the Schrödinger equation is not an easy task for multi-electronic systems. Thus, along the twentieth century a few approaches were proposed in order to calculate the electronic structure of solids. Nowadays, two of those methods have been more applied in computational physics, the density functional theory (DFT) and the tight-binding (TB) method. In the following section we describe the quantum problem for many electron systems, the DFT formalism and the different approaches related to it. Then, we introduce our particular TB method based in a sp3d5 basis set. Finally, only the techniques for calculating electronic transport properties in nano-scaled devices within the ballistic transport regime are discussed in the final section.

2.1 The Quantum Problem

In quantum mechanics the systems are described in terms of their quantum states, such description is carried out using the Schrödinger equation, as :

$$i\frac{\partial\Psi}{\partial t} = \widehat{H}\Psi. \tag{2.1}$$

The wave-particle duality observed for quantum particles in interference experiments, for instance, led to the postulate that the quantum state might be described by a wave function Ψ. Despite Ψ having no physical meaning by itself several information about the observable may be obtained from it using the quantum operators. In order to characterize the total energy of the system, the Hamiltonian operator $\widehat{H}$ acts in the wave function. In the multi-electronic framework the Hamiltonian operator is written in atomic units as:

$$\widehat{H} = -\frac{1}{2}\sum_i \nabla_i^2 - \frac{1}{2}\sum_j \frac{\nabla_A^2}{2M_A} - \sum_i\sum_A \frac{Z_A}{r_{iA}} + \sum_i\sum_{j>i}\frac{1}{r_{ij}} + \sum_A\sum_{B>A}\frac{Z_A Z_B}{R_{AB}}. \tag{2.2}$$

The first term yields the kinetic energy for the electrons $\widehat{T}_e$. The second term is related to the kinetic energy from the nuclei $\widehat{T}_n$. The third factor is the attraction potential between electron-nuclei $\widehat{V}_{e-n}$, the fourth term is related to the potential resultant from the interaction between electrons $\widehat{E}_{e-e}$ and the last represents the nuclei-nuclei repulsion $\widehat{V}_{n-n}$. Thus, Eq. 2.2 may be written as:

$$\widehat{H} = \widehat{T}_e + \widehat{T}_n + \widehat{V}_{e-n} + \widehat{E}_{e-e} + \widehat{V}_{n-n}. \tag{2.3}$$

Considering the time independence of the Hamiltonian operator, one could perform a variable separation in the wave function Ψ which exhibits a time dependence, thus:

$$\Psi(\vec{r},t) = \Phi(\vec{r})\Theta(t). \tag{2.4}$$

Such mathematical practice yields two equations:

$$\widehat{H}\Phi = E\Phi, \tag{2.5}$$

$$i\frac{\partial\Theta}{\partial t} = E\Theta. \tag{2.6}$$

Equation 2.5 is known as the time independent Schrödinger equation. Rewriting this equation in the form $(\widehat{H} - \Psi)E = 0$ leads to an eigenvalue problem for the Hamiltonian operator to be solved. Equation 2.6 represents the evolution of the temporal phase factor for the wave function. The solution to this equation is:

$$\Theta(t) = Aexp(-iEt), \tag{2.7}$$

with Eq. 2.7 A is a normalization constant. For time independent problems in this framework only the spacial part of the wave function $\Phi(\vec{r})$ needs to be considered. Observing the Hamiltonian operator (Eq. 2.2) we find that the third therm referring to the electron-nuclei coulombic interaction, turns the solubility of the problem difficult, thus it is needed to find out a valid approximation which enable us to separate the motions of the the electronic and nuclei parts since we are supposing to be working with many atoms in the system, and not just a simple problem like a single hydrogen atom. The solution to this problem, which allows decoupling the two motions is the Born-Oppenheimer approximation. This theory is also known as adiabatic approximation and it is based on the fact that the difference between electron and nuclei masses is high.

2.2 The Born-Oppenheimer Approximation

The Born-Oppenheimer approximation has considerable importance in condensed matter physics. It is the starting point to several other approximations which aims to describe the electronic structure of the matter. This approximation was proposed by M. Born and J.R. Oppenheimer in 1927 [39]. This approach is based on the fact that the rate between the electron mass and the electronic nuclei mass is very small. Such observation allows to consider that the nuclei can not move as fast as the electrons, thus considering the nuclei at rest. Therefore, the term $\widehat{T}_n$ in 2.3 becomes negligible. In other words the electronic cloud which is much lighter than the nuclei reorganizes almost instantaneously for any change in the configuration of the atoms. Such feature allows the decoupling of the motions of the nuclei and electrons. Thus, the the wave function may

be written as:

$$\Phi(\vec{r}) = \psi(\vec{r}_e)\Omega(\vec{r}_N). \tag{2.8}$$

Substituting 2.8 in 2.5 we have,

$$\widehat{H}\psi(\vec{r}_e)\Omega(\vec{r}_N) = E\psi(\vec{r}_e)\Omega(\vec{r}_N). \tag{2.9}$$

where the positions of the electrons are labelled as $\vec{r}_e$ and for the nuclei positions $\vec{r}_N$.

At this point we are able to solve the electronic problem. Since we are assuming that the nuclei positions does not changes in time. The interaction nuclei-nuclei can be taken as a parameter of the system, thus disregarding it as a variable. Furthermore the kinetic energy related to the nuclei is not taken into account, then we can reduce our problem to,

$$\widehat{H}_e\phi(\vec{r}_e) = E_e\phi(\vec{r}_e). \tag{2.10}$$

It is important to emphasize the fact that in the electronic problem the function $\Omega(\vec{r}_N)$ is a constant, since the nuclear positions are kept frozen. Here $\widehat{H}_e$ is called electronic Hamiltonian operator. It is written as

$$\widehat{H}_e = \widehat{T}_e + \widehat{V}_{e-n} + \widehat{E}_{e-e}. \tag{2.11}$$

After this simplification we can solve the electronic problem and find the wave function $\psi(\vec{r}_e)$ which corresponds to the electrons of the system, and consequently the electronic energy E_e.

Even considering only the electronic problem it is still a difficult problem to be solved specially for system containing many electrons. Nowadays there are many methods to calculate the electronic structure of the matter, among the most applied are the Tight-Binding (TB) [40] and the Hartree-Fock (HF) based methods [41]. In these two examples the electron-electron interaction is not totally considered, what leads to a loss in the knowledge of the fine structure of the system. Thus in order to obtain more accuracy, we decided to employ in some sections of this work the **Density Functional Theory (*DFT*)** [10]. DFT has been employed in the study of molecules and solids since the nineties. Its use has been growing steadily due to the advances of computational tools and to its relatively low computational cost compared to other HF based methods.

2.3 DFT Method

Among the possibilities to deal with the many electron problem, DFT has been the most employed in the last years. This is because the theory has yielded satisfactory results when describing electronic properties of atoms, molecules and solids in its ground state. Therefore DFT applications extends to several areas of the science such

as physics, chemistry, material sciences and engineering. A very interesting example of DFT application is the work by Umemoto, Wentzcovitch and Allen [42], where they have used DFT to model planetary formation. The DFT approach is based in obtaining the electronic density associated to the problem, which reduces the problem to a variable that depends only on the three spatial coordinates. Differently from the HF which depends on 3N variables, where N in the number of electrons. Such property of the DFT framework is very important from the practical point of view, since it allows for the lowering of the computational cost.

Density Functional Theory has been proposed within two seminal papers in the sixties, by Hohenberg and Kohn [43] and Kohn and Sham [44] where they describe the details of the theory and a methodology to apply it. However the basics of DFT lies in a theory proposed in the late twenties, the so called Thomas-Fermi approximation [45], which was proposed independently by Thomas in 1927 and Fermi in 1928. Thus due to the importance of Thomas-Fermi model to DFT we will make an introduction to this subject.

2.3.1 The Thomas-Fermi Theory

Historically L.H. Thomas was the first researcher to propose what we know as the Tomas-Fermi model, in 1926. His work aimed to develop a theory which was based on approximate fields for heavy atoms, in order to model quantum observables. This theory is based in four assumptions, which are:

1. Relativity corrections are negligible.

2. In the atom there is an effective field given by potential the $\mathbf{V}$, depending only on the distance $\mathbf{r}$ from the nuclei, such that
   $\mathbf{V} \longrightarrow 0$ as $\mathbf{r} \longrightarrow \infty$
   $\boldsymbol{V_r} \longrightarrow \boldsymbol{Z_e}$, the nuclear charge, as $\mathbf{r} \longrightarrow 0$

3. The electrons are uniformly distributed in the phase space with six dimensions. Each electron pair occupies a volume of h^3, where h is the Planck's constant.

4. The potential $\mathbf{V}$ is itself determined by the nuclear charge and the corresponding electronic distribution.

If we take an electron gas as a physical system enclosed onto a cubic box with a volume v, we could apply the periodic boundary conditions such that,

$$exp(ik_x v^{\frac{1}{3}}) = exp(ik_y v^{\frac{1}{3}}) = exp(ik_z v^{\frac{1}{3}}) = 1. \tag{2.12}$$

Thus starting from the plane wave solution to the free particle,

$$\phi_k(r) = \frac{1}{v^{\frac{1}{2}}} exp(iK \cdot r). \tag{2.13}$$

Where the energy is given by,

$$\epsilon_k = \frac{\hbar^2 k^2}{2m}. \tag{2.14}$$

Then we can find, that $k_x = n_x 2\pi/v^{\frac{1}{3}},\ k_y = n_y 2\pi/v^{\frac{1}{3}},\ k_z = n_z 2\pi/v^{\frac{1}{3}}$, where $n_x, n_y\ and\ n_z$ are integers. The possible wave vectors are those which in the k space are given by multiples of $2\pi/v^{\frac{1}{3}}$, and each k point occupies a volume Ω_k given by,

$$\Omega_k = \frac{8\pi^3}{v}. \tag{2.15}$$

The total volume in reciprocal space will be given by a sphere of radius k_F:

$$\Omega_t = \frac{4}{3}\pi k_F^3. \tag{2.16}$$

Considering the number of electrons (N), and that each state k has two spin components, spin α and spin β we have,

$$N = 2\frac{\Omega_t}{\Omega_k} = \frac{k_F^3 v}{3\pi^2}. \tag{2.17}$$

Now we can write down an expression for the electronic density:

$$\rho = \frac{N}{v} = \frac{k_F^3}{3\pi^2}. \tag{2.18}$$

If we write down the classical equation to the electron in a k state, under a electrostatic potential u(r), we will realize that within the volume of an atom the vector k must be related to the energy by,

$$\epsilon_F = \frac{\hbar^2 k_F^2}{2m} - eu(r). \tag{2.19}$$

Since there are no singularities in the charge density for $R \leq r$, the potential u(r) and electric field shall be continuous, so

$$u(r) = \frac{Z_{ef} e}{r}, \qquad for \qquad r > R. \tag{2.20}$$

Where R is the radius for a positive ion with the charge Z_{ef} to be determined. Thus the relations for r=R must be,

$$u(R) = \frac{Z_{ef} e}{R} \qquad and \qquad \left.\frac{du(r)}{dr}\right|_{r=R} = -\frac{Z_{ef} e}{R^2}. \tag{2.21}$$

Once an inner electron must be bound, its energy is less than the potential energy $-eu(r)$ at the surface of the shell. In this situation we have,

$$\frac{\hbar^2 k_F^2}{2m} = e[u(r) - u(R)]. \tag{2.22}$$

At this point we can derive an expression to the electronic density, using the Poisson relation,

$$\nabla^2 u(r) = -4\pi e\rho(r), \tag{2.23}$$

$$\rho(r) = \frac{1}{3\pi^2}\left[\frac{2me}{\hbar^2}\right]^{\frac{3}{2}} [u(r) - u(R)]^{\frac{3}{2}}. \tag{2.24}$$

It is important to note here, that the equation 2.24 should be used when $u(r) \geq u(R)$ otherwise the density will be equal to zero. In order to simplify the calculations we could translate 2.24 to spherical coordinates, thus resulting in:

$$\tilde{u}(r) \equiv \frac{r}{Ze}[u(r) - u(R)], \tag{2.25}$$

performing a simple change of variables, where $x = \frac{r}{a}$ and,

$$a = \left(\frac{9\pi^2}{128Z}\right)^{\frac{1}{3}} \frac{\hbar^2}{me^2} = 0.88534 Z^{-\frac{1}{3}} \frac{\hbar^2}{me^2}. \tag{2.26}$$

We obtain the *Thomas-Fermi relation* if we take the second derivative, such that

$$\frac{d^2\tilde{u}}{dx^2} = \frac{\tilde{u}^{\frac{3}{2}}}{\sqrt{x}}. \tag{2.27}$$

Applying the boundary condition, we have

$$\tilde{u}(0) = 1. \tag{2.28}$$

For $x = R/a$, we will have $\tilde{u}(x) = 0$, and from 2.25 we know,

$$\left.\frac{d\tilde{u}(r)}{dr}\right|_R = \left.\frac{u(r) - u(R)}{Ze}\right|_R + \left.\frac{ru'(r)}{Ze}\right|_R. \tag{2.29}$$

The first term in the right side of the equation 2.29 is zero when $r = R$ and knowing that $u'(R) = -Z_{ef}e/R^2$,

$$xu'(x) = \frac{-Z_{ef}}{Z}. \tag{2.30}$$

At this point, under this conditions we can obtain the number of electrons inside the sphere. Combining 2.24 and 2.25 we find,

$$4\pi \int_0^R \rho(r) r^2 dr = Z \int_0^x x\sqrt{x}\tilde{u}(x)^{\frac{3}{2}} dx, \tag{2.31}$$

and paying attention to the fact that $\sqrt{x}\tilde{u}'' = \tilde{u}^{\frac{3}{2}}$, we have:

$$Z \int_0^x x\tilde{u}'' dx = Z\tilde{u}(0) + \tilde{u}(x). \tag{2.32}$$

Now combining equations 2.28 and 2.30 It results in,

$$4\pi \int_0^r \rho(r) r^2 dr = Z - Z_{ef}. \tag{2.33}$$

The expression to the charge density (Eq. 2.24) can be derived by the variational principle, in which the total energy is a functional of the electronic density ρ, written in the form:

$$E[\rho] = \xi \int \rho^{\frac{5}{3}} d^3r - e \int \rho u_N d^3r - \frac{1}{2} e \int \rho u_e d^3r + U_{NN}. \tag{2.34}$$

Here

$$\xi = \frac{3h^2}{10m}\left(\frac{3}{8\pi}\right)^{\frac{2}{3}}, \tag{2.35}$$

and u_N is the potential related to the nuclei, u_e is the potential due to the electrons. The first integral in 2.34 corresponds to the kinetic energy term for the electrons, the second integral is the energy due to the electron-nuclei interaction, the third integral is the term which describes the electron-electron interaction, and U_{NN} is the interaction between nuclei.

Now we can write the Thomas-Fermi relation. Whether the energy $E[\rho]$ has a stationary value in relation to the density ρ and the number of electrons is kept constant in relation to the time. We obtain the following relation:

$$\frac{\delta}{\delta\rho}\left\{E[\rho] - u(R)\int \rho d^3r\right\} = 0. \tag{2.36}$$

To finalize this exposure about this pioneer theory, we write the Thomas-Fermi-Dirac functional $E[\rho]$, which include the exchange term proposed by Dirac in 1930,

$$E[\rho] = \xi\int \rho^{\frac{5}{3}}d^3r - e\int \rho u_N d^3r - \frac{1}{2}e\int \rho u_e d^3r + U_{NN} - \frac{3}{4}e^2\left(\frac{3}{\pi}\right)^{\frac{1}{3}}\int \rho^{\frac{4}{3}}d^3r. \tag{2.37}$$

If $E[\rho]$ is stationary in relation to variations of the electronic density ρ we have the equation of Thomas-Fermi-Dirac to the electronic density.

$$\rho = \frac{8\pi}{3h^2}(2me)^{\frac{3}{2}}\left[\frac{(2me^3)^{\frac{1}{2}}}{h} + \left(u - u(R) + \frac{2me^3}{h}\right)^{\frac{1}{2}}\right]^3. \tag{2.38}$$

2.3.2 The Fundamental Theorems

Density Functional Theory is based on two elementary theorems, proposed by Honhenberg and Kohn in 1964 [43] as an improvement of the Thomas-Fermi method. The first theorem states,

"The ground state energy from Schrödinger's equation is a unique functional of the electron density."

Considering a number of electrons N, inside a large box and moving under the influence of an external potential $u(r)$, and taking into account the coulombic repulsion, we can prove this theorem by *reductio ad absurdum*. Since the Hamiltonian for this system has the form:

$$\widehat{H} = \widehat{T} + \widehat{V} + \widehat{U}. \tag{2.39}$$

where,

$$\widehat{T} \equiv \frac{1}{2}\int \nabla\psi^*(\vec{r})\nabla\psi(\vec{r})d\vec{r}, \tag{2.40}$$

$$\widehat{V} \equiv \int u(\vec{r})\psi^*(\vec{r})\psi(\vec{r})d\vec{r}, \tag{2.41}$$

$$\widehat{U} = \frac{1}{2}\int \frac{1}{|\vec{r}-\vec{r'}|}\psi^*(\vec{r})\psi^*(\vec{r'})\psi(\vec{r})\psi(\vec{r'})d\vec{r}d\vec{r'}. \tag{2.42}$$

Assuming for simplicity that the ground state ψ is not degenerate we can define the electronic density as:

$$\rho(\vec{r}) = \sum_i \psi^*(\vec{r})\psi(\vec{r}) = \langle\psi|\sum_i \delta(\vec{r}-\vec{r_i})|\psi\rangle. \tag{2.43}$$

Now if we consider another external potential $u'(\vec{r})$, leading to a new Hamiltonian $\widehat{H}$ and to a new ground state $\psi(\vec{r'})$. By the hypothesis in which the potentials lead to the same

electronic density $\rho(\vec{r})$, then:

$$E = \langle\psi|\widehat{T} + \widehat{V} + \widehat{U}|\psi\rangle < \langle\psi'|\widehat{T} + \widehat{V} + \widehat{U}|\psi'\rangle,$$
$$E' = \langle\psi'|\widehat{T} + \widehat{V}' + \widehat{U}|\psi'\rangle < \langle\psi|\widehat{T} + \widehat{V}' + \widehat{U}|\psi\rangle.$$

Consequently,

$$\langle\psi|\widehat{H}|\psi\rangle < \langle\psi|\widehat{H}'|\psi\rangle = \langle\psi'|\widehat{H}'|\psi'\rangle + \langle\psi'|\widehat{V} - \widehat{V}'|\psi'\rangle. \tag{2.44}$$

Writing Eq. 2.44 in terms of the energy we will see that,

$$E < E' + \int [u(\vec{r}) - u'(\vec{r})]\rho(\vec{r})d(\vec{r}). \tag{2.45}$$

Thus for the term $\langle\psi'|\widehat{H}'|\psi'\rangle$,

$$E' < E + \int [u'(\vec{r}) - u(\vec{r})]\rho(\vec{r})d(\vec{r}). \tag{2.46}$$

In other words,

$$E + E' < E' + E. \tag{2.47}$$

Thus, if we had assumed the same electronic density $\rho(\vec{r})$, with $u \neq u'$, we are facing an absurd, since $\psi \neq \psi'$. This shows that the first theorem is valid.

The second theorem states that

"The electronic density that minimizes the energy of the overall functional is the true electronic density corresponding to the complete solution of the Schrödinger equation."

This statement is proven in the following steps,

$$E[\rho] = \langle\psi|\widehat{T} + \widehat{U} + \widehat{V}|\psi\rangle. \tag{2.48}$$

In that case we set $\rho(\vec{r})$ as an electronic density for a given state ψ, which is not necessarily the true density that comes from $\widehat{H} = \widehat{T} + \widehat{U} + \widehat{V}$ that will be called ρ_0, thus:

$$\rho \neq \rho_0 \Longrightarrow \psi \neq \psi_0, \qquad then, \qquad E > E_0$$
$$\rho = \rho_0 \Longrightarrow \psi = \psi_0, \qquad then, \qquad E = E_0$$

If we re-write the equation 2.48 we can have it in the form,

$$E[\rho] = \langle\psi|\widehat{T} + \widehat{U}|\psi\rangle + \langle\psi|\widehat{V}|\psi\rangle, \tag{2.49}$$

or just,

$$E[\rho] = F[\rho] + \langle\psi|\widehat{V}|\psi\rangle. \tag{2.50}$$

Here $F[\rho]$ is an **universal functional** that is valid for every Coulomb system and the term $\langle\psi|\widehat{V}|\psi\rangle$ depending on the system. In an analogue way we can write the same thing to the exact electronic density, therefore

$$E[\rho_0] = F[\rho_0] + \langle\psi_0|\widehat{V}|\psi_0\rangle. \tag{2.51}$$

Then, if ψ_0 represents the true ground state, and ψ another state, consequently ρ_0 and ρ are defined by any external potential. From the variational theorem we have:

$$E[\psi_0] < E[\psi], \tag{2.52}$$

$$\langle\psi_0|\widehat{T}+\widehat{U}|\psi_0\rangle+\langle\psi_0|\widehat{V}|\psi_0\rangle<\langle\psi|\widehat{T}+\widehat{U}|\psi\rangle+\langle\psi|\widehat{V}|\psi\rangle, \tag{2.53}$$

$$F[\rho_0]+\langle\psi_0|\widehat{V}|\psi_0\rangle<F[\rho]+\langle\psi|\widehat{V}|\psi\rangle. \tag{2.54}$$

Thus,

$$E[\rho_0]<E[\rho]. \tag{2.55}$$

So now we have proven the second Hohenberg-Kohn theorem.

2.3.3 The Kohn-Sham Equations.

So far we have discussed a theory which can leads to a solution for the electronic structure problem. However one year after the Hohenberg-Kohn work, another paper by Kohn-Sham was published [44]. To solve the ground state problem self-consistently including the exchange interaction. Thus according to the Ref. [43] the ground state energy for an electron gas, where the particles are interacting with each other is given by:

$$E=\int u(\vec{r})\rho(\vec{r})d\vec{r}+\frac{1}{2}\int\int\frac{\rho(\vec{r}')\rho(\vec{r})}{\vec{r}-\vec{r}'}d\vec{r}d\vec{r}'+G[\rho]. \tag{2.56}$$

In equation 2.56 $u(\vec{r})$ is the static potential which is external to the electron gas, $\rho(\vec{r})$ is the electronic density and the term $G[\rho]$ is an universal functional of density, defined as:

$$G[\rho]\equiv T_s[\rho]+E_{xc}[\rho]. \tag{2.57}$$

In the Kohn-Sham formalism, the $T_s[\rho]$ term stands for the kinetic energy related to a non-interacting system, and the term $E_{xc}[\rho]$ is the exchange and correlation interaction of an interacting system. Then, if the density can vary slowly it is possible to write down the following equation to the exchange-correlation term:

$$E_{xc}[\rho]=\int\rho(\vec{r})\epsilon_{xc}(\rho(\vec{r}))d\vec{r}. \tag{2.58}$$

In this case $\epsilon_{xc}(\rho(\vec{r}))$ is the exchange and correlation energy per electron in an uniform electron gas where the density is $\rho(\vec{r})$. By the variational theorem, the minimization for Eq. 2.56 requires the following condition:

$$\int\delta\rho(\vec{r})d\vec{r}=0. \tag{2.59}$$

Leading to,

$$\int\delta\rho(\vec{r})\left\{\varphi(\vec{r})+\frac{\delta T_s[\rho]}{\delta\rho(\vec{r})}+\mu(\rho(\vec{r}))\right\}d\vec{r}=0. \tag{2.60}$$

In Eq. 2.60,

$$\varphi(\vec{r})=u(\vec{r})+\int\frac{\rho(\vec{r}')}{\vec{r}-\vec{r}'}d\vec{r}'. \tag{2.61}$$

and

$$\mu(\rho(\vec{r})) = \frac{d(\rho\epsilon_{xc}(\rho(\vec{r})))}{d\rho}. \tag{2.62}$$

Solving Eq. 2.60 it is possible to find an expression similar to the Schrödinger equation, involving eigenvalues. Such equation has the form:

$$\left(-\frac{1}{2}\nabla^2 + u^{KS} \right)\psi_i(\vec{r}) = \varepsilon_i\psi_i(\vec{r}). \tag{2.63}$$

Once,

$$u^{KS} = \varphi(\vec{r}) + \mu(\rho(\vec{r})). \tag{2.64}$$

u^{KS} and $\mu(\rho(\vec{r}))$ are respectively the Kohn-Sham effective potential and the chemical potential of the system. The density can be obtained as,

$$\rho(\vec{r}) = \sum |\psi_i(\vec{r})|^2. \tag{2.65}$$

The equation 2.63 must be solved self-consistently. In Figure 11 we have a schematic graphic where the self-consistent cycle is described. Finally, the Kohn-Sham energy is

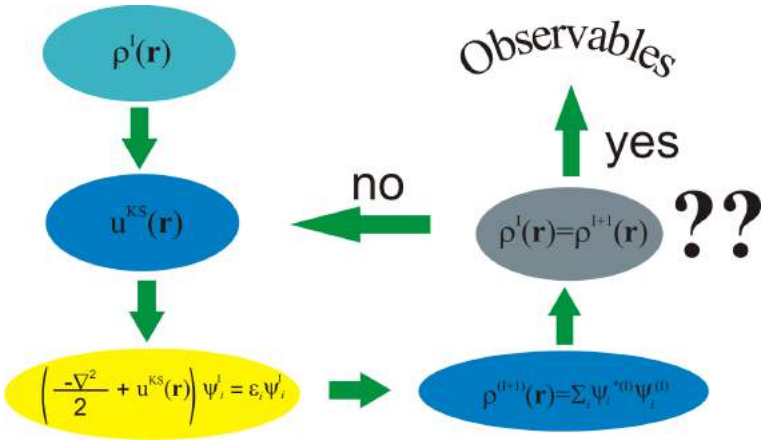

Figure 11: Self-Consistent cycle to solve the Kohn-Sham equations. It begins from a trial electronic density $\rho(\vec{r})$ for the system. Thus the orbitals $\psi_i(\vec{r})$ are obtained. After that it is possible to get a second value to the electronic density. The cycle is kept until a threshold value is reached for convergence.

given by,

$$E_{KS} = \sum \varepsilon_i - \frac{1}{2}\int\int \frac{\rho_0(\vec{r}')\rho_0(\vec{r})}{\vec{r}-\vec{r}'}d\vec{r}d\vec{r}' + \int \rho(\vec{r})[\epsilon_{xc}(\rho(\vec{r})) - \mu(\rho(\vec{r}))]\epsilon_{xc}(\rho(\vec{r})), \tag{2.66}$$

once,

$$\sum \varepsilon_i = T_s[\rho(\vec{r})] + \int u^{KS}\rho(\vec{r})d\vec{r}. \tag{2.67}$$

2.3.4 Exchange-Correlation Term

One of the open issues regarding the DFT technique is related to the exchange-correlation term (xc) which has no analytic form which can be applied for every systems. If we observe carefully equation 2.66 we will note that $\epsilon_{xc}(\rho(\vec{r}))$ is not known and probably it never will be exactly found for all tractable systems. However there are some

approximations which have been used for obtaining acceptable results for several systems. The first of those approaches is the **Local Density Approximation (LDA)**, where the exchange-correlation energy for a system with a local density ρ is proposed to be the same as in an electron gas with the same density [46]. It's important to emphasize that for this approximation to be valid the density must vary smoothly around a given space position. Then we can write down the following equation:

$$E_{xc}^{LDA}[\rho] = \int \rho(\vec{r})\epsilon_{xc}^{LDA}(\rho(\vec{r}))d\vec{r}. \tag{2.68}$$

The function $\epsilon_{xc}^{LDA}(\rho(\vec{r}))$, can be divided in two parts, one refers to the exchange and the other to the correlation, so:

$$\epsilon_{xc}^{LDA}(\rho(\vec{r})) = \epsilon_x(\rho(\vec{r})) + \epsilon_c(\rho(\vec{r})). \tag{2.69}$$

Then, the corresponding exchange-correlation potential for the LDA approach is given by,

$$u_{xc}^{LDA}[\rho] = \frac{dE_{xc}^{LDA}}{d\rho(\vec{r})} = \epsilon_{xc}(\rho(\vec{r})) + \rho(\vec{r})\frac{d\epsilon_{xc}^{LDA}(\rho(\vec{r}))}{d\rho(\vec{r})}. \tag{2.70}$$

Now, getting back to the equation 2.69, the exchange term $\epsilon_x(\rho(\vec{r}))$ can be extracted from Hartree-Fock theory. If we take into account the Slater contribution it can be obtained for a homogeneous electron gas that,

$$\epsilon_x(\rho(\vec{r})) = \frac{-3Ne^2k_F}{4\pi}. \tag{2.71}$$

Once we know that $k_F = (3\pi^2\rho)^{\frac{1}{3}}$, the energy per volume is,

$$\epsilon_x(\rho(\vec{r})) = \frac{E_x}{V} = \frac{-3e^2(2\pi)^{\frac{1}{3}}\rho^{\frac{4}{3}}}{4\pi}. \tag{2.72}$$

Writing the density ρ as a function of the Winger radius r_s We get,

$$\rho(\vec{r}) = \frac{3}{4\pi r_s}. \tag{2.73}$$

Finally we have,

$$\epsilon_x(\rho(\vec{r})) = \frac{-0.4582}{r_s}. \tag{2.74}$$

The correlation term $\epsilon_c(\rho(\vec{r}))$ has a high degree of complexity and has no analytical solution even for an ideal electron gas. Despite of this, in 1981 Ceperley and Alder [47] published results from a quantum Monte Carlo calculation, which yields accurate values for the correlation interaction in many different systems. After this first proposal, Perdew and Zunger [48] took the work in Ref. [47] as parameter to deal with high ($r_s < 1$) and low ($r_s > 1$) densities.

Then the expression that describes low densities for each electron according Ref. [48] is given by:

$$\epsilon_c^i = \frac{\gamma_i}{1 + \beta_1^i\sqrt{r_s} + \beta_2^i r_s}. \tag{2.75}$$

On the other hand, the expression to high densities is written as,

$$\epsilon_c^i = A_i ln[r_s] + B_i + C_i r_s ln[r_s] + D_i r_s. \tag{2.76}$$

In the equations 2.75 and 2.76 the parameters for the homogeneous electron gas are given by, $\gamma = -0.1423$, $\beta_1 = 1.0529$, $\beta_2 = 0.3334$, $C = 0.0020$, $D = -0.0116$, $A = 0.0311$, $B = -0,048$ in the situation where there is no polarization. There are some particularities about the LDA which might be mentioned, for example it's known that LDA overestimates the atomic distances and the dissociation energies. Also, the bulk modulus is overestimated by 8 to 18 % and the band gap in semiconductors is underestimated by about 50 %.

However, when we are working with real atomic systems, the electronic density is not in general constant. Thus, in order to improve the LDA a new approach was proposed known as the **Generalized Gradient Approximation (GGA)**. In this picture the gradient of density is taken into account to obtain the exchange functional $E_{xc}[\rho]$. There are different proposals for how the gradient term is included in the GGA term, some of the most applied formalism in several software packages are based on the works of Perdew-Burke-Erzenhof [49] and Lee-Yang-Parr [50]. In a general way the exchange-correlation functional in the GGA is written as:

$$E_{xc}^{GGA}[\rho] = \int f(\rho(\vec{r}), \nabla\rho(\vec{r}))d\vec{r}. \tag{2.77}$$

Since the main source of uncertainty in DFT is associated to the Exchange-Correlation Functional, the GGA approach brought more accuracy to the calculations, and nowadays it is a widely employed tool in atomic-molecular modelling.

2.3.5 The Pseudopotential Approach

In principle, when we are working with atomic species in the DFT framework all electrons should be considered. However for the chemical bonding process only the outermost electrons are important. In a practical way a DFT calculation is performed considering every electron in the system. For this reason, it is sometimes useful to perform the calculation considering only the valence electrons. This means replacing the inner electrons by a pseudopotential (**PP**), which must be as accurate as the contribution from the real electrons. This process is called a frozen core calculation. Nowadays the frozen core framework is widely more employed than all-electrons calculations. A immediate reason for this is that the computational effort is far more economic than in an AE calculation. And the results are as accurate as in an all-electrons calculation.

A pseudopotential can be built using empirical parameters, obtained from experimental. Alternatively, a DFT calculation for the single atom where all electrons were considered is used to build the pseudopotential. This is known as the *ab-initio* method for obtaining a pseudopotential. This second procedure is seen in the literature more frequently than the first one. The most relevant works in this area came from Bachelet,

Hamann and Schlüter [51] and Troullier-Martins [52]. These particular constructions are said to be Norm-Conserving pseudopotential [53], but there are pseudopotentials where the norm is not conserved, like the one proposed by Vanderbilt [54]. An *ab-initio* pseudopotential in its construction always starts from an all electron calculation, and the PP must keep some important properties in order to conserve the norm:

1. The eigenvalues ε_i from an All-Electron (**AE**) calculation must be identical to the eigenvalues ε_i^{PP} from pseudopotential.

2. The eigenvectors from AE calculation and those from PP must be the same for $r > r_c$ where r_c here is the core radius.

3. The integrals from 0 upto r, $r > r_c$, related with charge density of AE calculation must be equal to the obtained with the PP.

4. The logarithmic derivative of pseudo-eigenstate must converge to the AE eigenstate when $r > r_c$.

Properties 3 and 4 are closely related with the pseudopotential *transferability* [55], which is the capability of a pseudopotential to be used in different kinds of chemical environments, since atoms in crystals, molecules or even in a gas phase may not behave equally. Figure 12 shows the schematic behavior as expected for a PP. Showing the expected relation for the pseudo eigenstate and the AE eigenstate as well as the potentials from pseudopotential and AE calculation.

Since we are interested in *ab-initio* pseudopotentials, then we should begin from the Kohn-Sham equation,

$$[T + u^{KS}(\vec{r})]\psi_i(\vec{r}) = \varepsilon_i\psi_i(\vec{r}). \tag{2.78}$$

Adopting spherical coordinates to solve Eq. 2.78, we can write down the following expression:

$$\left(-\frac{1}{2}\frac{d^2}{d\vec{r}^2} + \frac{l(l+1)}{2\vec{r}^2} + u^{KS}[\rho, \vec{r}] \right)\vec{r}R_{nl}(\vec{r}) = \varepsilon_{nl}\vec{r}R_{nl}(\vec{r}). \tag{2.79}$$

Where $u^{KS}[\rho, \vec{r}]$ is the self-consistent potential for one electron. For sake of simplicity we will refer to this term as $u[\rho, \vec{r}]$, and it is given as:

$$u[\rho, \vec{r}] = \frac{-Z}{\vec{r}} + u_H[\rho, \vec{r}] + u_{xc}[\rho(\vec{r})], \tag{2.80}$$

where $\rho(\vec{r})$ is the sum of whole electronic density and $u_H[\rho, \vec{r}]$ is the Hartree potential which is related to every $R_{nl}(\vec{r})$ state. The last term $u_{xc}[\rho(\vec{r})$ is the potential due to the exchange-correlation interaction. It varies depending on the approximation which has been chosen for this interaction.

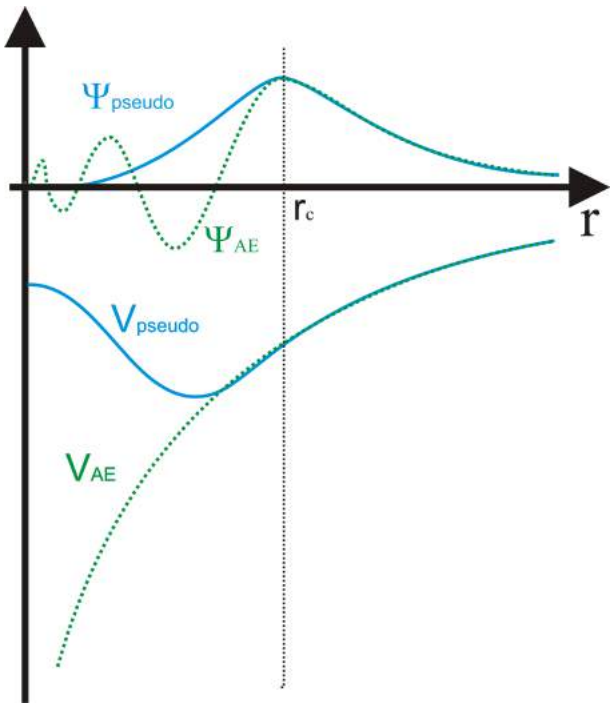

Figure 12: Schematic representation for the pseudopotential (full line in blue) and AE potential (dot line in green), and the corresponding eigenstates. The vertical dot line in black represents the core radius, satisfying the conditions 1 and 2.

After doing this this calculations, we obtained the eigenvectors of the all-electron calculation $R_l^{AE}(\vec{r})$ and its respective eigenvalues ε_l^{AE}. Thus it is possible to start a parametrization of the pseudopotential, following the properties listed above. Therefore the property 1 is written mathematically as,

$$R_l^{PP}(\vec{r}) = R_l^{AE}(\vec{r}) \qquad when \qquad r > r_c. \tag{2.81}$$

For property 2 we have,

$$\int_0^{r_c} |R_l^{PP}(\vec{r})|^2 \vec{r}^2 d\vec{r} = \int_0^{r_c} |R_l^{AE}(\vec{r})|^2 \vec{r}^2 d\vec{r} \tag{2.82}$$

and finally,

$$\varepsilon_l^{PP} = \varepsilon_l^{AE} \tag{2.83}$$

After we have obtained the AE potential and eigenfunctions we can set up an analytic cutoff function $\boldsymbol{f(\vec{r})}$, going to 0 when $\vec{r} \to 0$, and tending to 1 as fast as $\vec{r}^3$. A r_c must be chosen for each l, in general 0.5 to 1.0 times the radius r_{ml} of the outermost peak of u_l. Then we can construct the following potential:

$$u_{1l}^{PP} = u\left(1 - f\left(\frac{\vec{r}}{r_c}\right)\right) + c_l f\left(\frac{\vec{r}}{r_c}\right), \quad where = \begin{cases} f(\frac{\vec{r}}{r_c}) \to 1 & \text{if} \quad \vec{r} \to 0. \\ f(\frac{\vec{r}}{r_c}) \to 0 & \text{if} \quad \vec{r} \to \infty. \end{cases} \tag{2.84}$$

There are several forms for $\boldsymbol{f(\vec{r})}$ in the literature which can be used depending on what conditions are desired for the PP. Here u is the AE potential displayed in Eq. 2.80, which is the base for parametrization of a smooth PP and without nodes, and c_l represents an

adjustment constant in order to ensure the absence of singularities.

Thus a pseudo-eigenvector w_{1l}^{PP} can be proposed and fitted to coincide with the radial solution of Kohn-Sham equation, following the property 1 if we make use of a fitting constant γ_l as following,

$$\gamma_l w_{1l}^{PP}(\vec{r}) \rightarrow R_l^{AE} \qquad for \qquad \vec{r} \geq r_c. \tag{2.85}$$

Then to have the other properties satisfied 2-4, we need normalize w_{1l}^{PP}, so we will have a definitive pseudo-eigenvector labelled as R_l^{PP}

$$R_l^{PP} = \gamma_l \left[w_{1l}^{PP} + \delta_l \vec{r}^{l+1} f\left(\frac{\vec{r}}{r_c}\right) \right]. \tag{2.86}$$

Where δ_l is the smallest solution for the normalization equation,

$$\gamma_l^2 \int_0^\infty \left[w_{1l}^{PP} + \delta_l \vec{r}^{l+1} f\left(\frac{\vec{r}}{r_c}\right) \right]^2 d\vec{r} = 1. \tag{2.87}$$

Now that we have the knowledge about the pseudo-eigenfunction we can obtain a potential related to this one, by an inversion of a Schrödinger type equation. It is important to emphasizes the fact that the potential like this is not a ionic potential, this is the screened potential (scr).

$$u_{scr,l}^{PP} = \varepsilon_l - \frac{l(l+1)}{2\vec{r}^2} + \frac{1}{2\vec{r} R_l^{PP}(\vec{r})} \frac{d^2}{d\vec{r}^2} [\vec{r} R_l^{PP}(\vec{r})]. \tag{2.88}$$

So far we have an atomic pseudopotential. To make it useful for another self-consistent process it is needed to find out an ionic PP from equation 2.88. It is important to the improvement of transferability of the PP, allowing its employment in several chemical environments. The ionic PP is obtained removing the Hartree potential $u_H^{PP}(\vec{r})$ and the exchange-correlation term $u_{xc}^{PP}(\vec{r})$ from the screened potential,

$$u_{ion,l}^{PP}(\vec{r}) = u_{scr,l}^{PP}(\vec{r}) - u_H^{PP}(\vec{r}) - u_{xc}^{PP}(\vec{r}). \tag{2.89}$$

Here is not hard to realize, that each component of the angular momentum of the wave function, feels a different potential. In that case we should set-up an ionic pseudopotential operator like,

$$\widehat{u}_{ion}^{PP}(\vec{r}) = u_{ion,local}^{PP}(\vec{r}) + \sum_l u_{nonlocal,l}^{PP}(\vec{r}) \widehat{P}_l. \tag{2.90}$$

Where $u_{ion,local}^{PP}(\vec{r})$ is a local potential. The non-local potential comes as a projection of l-th angular momentum of the wave function, then it is defined as,

$$u_{nonlocal,l}^{PP}(\vec{r}) = u_{ion,l}^{PP}(\vec{r}) - u_{ion,local}^{PP}(\vec{r}). \tag{2.91}$$

Indeed the potential presented in Eq. 2.91 is a semi-local potential.

Generally, the local potential can be set arbitrarily, since the value for l is truncated at some finite point. It is important to make sure that the local potential reproduces the features of the atomic scattering for all the higher angular momentum channels. For sake of convenience, we will show in this section the Kleiman and Bylander

[56] formulation for $u^{PP}_{nonlocal,l}(\vec{r})$ term, which states that non-local term has the form:

$$u^{KB}_{nonlocal,l}(\vec{r}) = \frac{|u^{PP}_{nonlocal,l}(\vec{r})\Phi^{PP,0}_{l}(\vec{r})\rangle\langle\Phi^{PP,0}_{l}(\vec{r})u^{PP}_{nonlocal,l}(\vec{r})|}{\langle\Phi^{PP,0}_{l}(\vec{r})|u^{PP}_{nonlocal,l}(\vec{r})|\Phi^{PP,0}_{l}(\vec{r})\rangle}. \tag{2.92}$$

Where $\Phi^{PP,0}_{l}(\vec{r})$ is the pseudo-function used as atomic reference, including the angular momentum component. In summary a very good strategy to construct the PP is to make it as close as possible to the conditions on what it will be employed. Further reading can be found in the references [51, 56].

2.3.6 Base Functions

After defining the pseudopotentials, and the orbitals via DFT, the space related to the orbitals radius has no limitations extending to infinite. Indeed It turns the calculation hard to be carried out. It is very convenient to define a cutoff radius for each orbital, thus imposing a confinement. The calculation become much more easy to be carried out. Such feature may be obtained using a basis set, based on multiple ζ theory [57, 58]. Then the interaction between atomic orbitals is reduced for those, in which there is an overlap between its wave functions. Numerically this procedure is observed as a reduction of the terms in the Hamiltonian matrix which are different from zero, as well as in overlap matrix. The diminution in the terms to be calculated in the matrix, brings the possibility of working with systems containing a considerable number atoms, the so called Order-N calculation [59]. The atomic orbital is given by the product of a radial function and a spherical harmonic function:

$$\phi_{lmn} = R_{ln}Y_{lm}. \tag{2.93}$$

The radial function is centred in the atomic nucleus. Increasing the number of functions to describe the radial part, the complexity and accuracy of the orbitals increases as well.

The first function in that family is the single-ζ (SZ), It is the most simple function in this context, and they are obtained from the Schrödinger equation solution for a single atom, based in the pseudopotential corresponding to the specific chemical specie,

$$\left(-\frac{1}{2r}\frac{d^2}{dr^2}r + \frac{l(l+1)}{2r^2} + U_l(r)\right)\phi_l(r) - (\epsilon_l + \delta\epsilon_l)\phi_l(r). \tag{2.94}$$

When we cutoff the range of the atomic orbital, we are limiting the action of that state, which in principle should be infinite. Then we are neglecting a small amount of energy. Thus to equilibrate this problem a small value in the energy $\delta\epsilon_l$ is added to the orbital energy in Eq. 2.94. This energy shift keeps the wave function normalization and it is a good way to impose the confinement.

Some different schemes are present in the literature to construct the second order function, the double-ζ. However, the most used in this kind of application is the

split valence framework [60]. Here the orbitals are given by a fixed linear combination of Gaussians. In that sense the second ζ orbital $\phi^{2\zeta}$ is a continuity of $\phi^{1\zeta}$ for a given range, as following:

$$\phi_l^{2\zeta}(r) = \begin{cases} r^l(a_l - b_l r^2) & \text{if} \quad r < r_l^s \\ \phi_l^{1\zeta}(r) & \text{if} \quad r \geq r_l^s \end{cases} \tag{2.95}$$

Where a_l and b_l are continuity constants, determined at r_l^s, then it is defined the first and second order ζ functions. This second order function is that was widely employed in this theses through the Spanish Initiative for Electronic Simulations with Thousands of Atoms **SIESTA** method to carry out the results presented here, further information about the package can be found in Ref. [61].

2.4 Slater-Koster Tight Binding

To solve the secular equation associated to atomic systems is not an easy task even nowadays. As proposed originally by Block [62] the linear combination of atomic orbitals (LCAO) method, may imply in a significative challenger for the modern super computers. Facing the same difficulties in the fifties, Slater and Koster (SK) proposed a simplified version of LCAO, in their seminal work [63]. In a rigorous application of LCAO, one must define an atomic function $\chi_\mu(\vec{r} - \vec{R})$, for every atom in the unit cell located at position $\vec{R}$. Thus the linear combination ϕ_μ of those atomic orbitals may be written as follows:

$$\phi_\mu(\vec{K}, \vec{r}) = \frac{1}{\sqrt{N}} \sum_R e^{i\vec{k}\cdot\vec{R}} \chi_\mu(\vec{r} - \vec{R}). \tag{2.96}$$

Therefore the Hamiltonian matrix elements are given by:

$$H_{\mu\nu}(\vec{k}) = \int \phi_\mu^*(\vec{K}, \vec{r}) \widehat{H} \phi_\nu(\vec{K}, \vec{r}) d^3r. \tag{2.97}$$

Here $\chi_\mu(\vec{r} - \vec{R})$ is constructed in the same form as in Eq. 2.93, which means that for every Hamiltonian element, an integral like in Eq. 2.97 must be solved. If we consider systems where the d orbitals play important role, the Hamiltonian matrix rank might become very large, resulting in a challenging computational work.

On the other hand, when the SK method is applied, the integral is substituted by a fitted potential (parameter), furthermore one may choose the most interesting energy range for any problem, for instance the energy involving the valence or conduction bands in a crystal, then discarding many integrals. Considering the orbitals s, p and d, between atoms of the same chemical type, ten hopping (overlap) are considered $V_{ss\sigma}, V_{sp\sigma}, V_{pp\sigma}, V_{sd\sigma}, V_{pd\sigma}, V_{dd\sigma}, V_{pp\pi}, V_{pd\pi}, V_{dd\pi}, V_{dd\delta}$, the same set of potentials should be obtained for the overlap parameters in the non-orthogonal tight binding case. The reader interested into the application of the SK equations in a computational code, must be

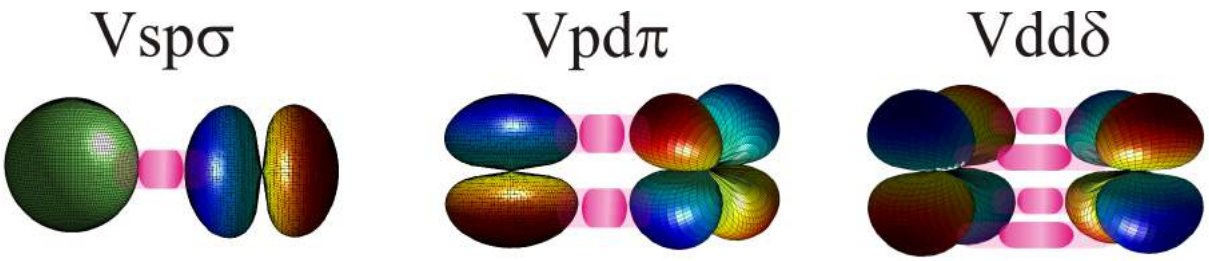

Figure 13: Different bonding types, σ, π, δ, represented in hopping energies $V_{sp\sigma}$, $V_{pd\pi}$ and $V_{dd\delta}$.

aware that when dealing with interaction between different chemical species, the number of parameters is fourteen due the anti-symmetric directed orbitals, $ps\sigma, ds\sigma, dp\sigma, dp\pi$. In figure 13 the different bonding types are sketched, using the $V_{sp\sigma}$, $V_{pd\pi}$ and $V_{dd\delta}$ hopping energies.

In the appendix A, the entire set of SK equations is written for the sp^3d^5 orbitals. It is also important to mention that the parity of the integral is given according the following rule:

$$\langle L|\widehat{H}|L'\rangle = (-1)^{L+L'}\langle L|\widehat{H}|L'\rangle. \tag{2.98}$$

Where L represents the angular momentum of each orbital. In the equations discussed in the appendix A, l, m, n, stands for the direction cosines, of the involved bond.

2.5 Ballistic transport

Figure 14: Two 2DEG separated by a narrow channel, the left 2DEG has a small difference in the chemical potential $\delta\mu$ in relation to the right one.

Let's imagine two reservoirs containing a two dimensional electrons gas (2DEG) each, spatially separated by empty space. Assuming that the first reservoir has a small difference in the electron density (δn) in relation to the second one, then we link both 2DEG by a narrow channel. Thus a diffusion current $\vec{J}$ should flow through the channel, carried by the electrons in the energy range between E_f (Fermi level) and $E_f + \delta\mu$. In this context we can define the small difference in the electron density ($\delta\mu$) as being the chemical potential difference between the reservoirs. One could describe the conductance in such system, by generalizing the Einstein relation [40], as following:

$$\sigma = e^2\rho(E_f)D. \tag{2.99}$$

Where σ is the electronic conductivity, D is the diffusion constant and $\rho(E_f)$ is the density

of states at the Fermi level. Whether we are in a situation in which the width (W) and the length (L) of the system is minor than the electron mean free path (l) then the ballistic transport takes is place, thus Eq. 2.99 is generalized as:

$$G = e^2\rho(E_f)\tilde{\mathrm{D}}. \tag{2.100}$$

Where G is the electronic conductance through the system [64] and $\tilde{\mathrm{D}}$ is the diffusance, which is related to $\vec{J} = \tilde{\mathrm{D}}\delta n$, thus $\delta\mu = \frac{\delta n}{\rho(E_f)}$. The density of states at the Fermi level may be written as:

$$\rho(E_f) = g_s g_v \left[2\pi \frac{dE_n(k)}{dk}\right]^{-1}. \tag{2.101}$$

Here g_s and g_v are integers related to the spin and valley degeneracy respectively. The current density $\vec{J}$ also may be written in therms of the drift velocity as,

$$\vec{J} = \rho(E_f)\nu_n(k), \tag{2.102}$$

where $\nu_n(k)$ is the drift velocity in the channel, given by,

$$\nu_n(k) = \frac{dE_n(k)}{\hbar dk} \tag{2.103}$$

Finally integrating in the energy range between $E_f + \delta\mu$ and E_f, the current in the channel is,

$$\vec{J_n} = \int_{E_f}^{E_f+\delta\mu} g_s g_v \left[2\pi \frac{dE_n(k)}{dk}\right]^{-1} \frac{dE_n(k)}{\hbar dk}. \tag{2.104}$$

Thus,

$$\vec{J_n} = \frac{g_s g_v}{h}\delta\mu. \tag{2.105}$$

Recording that the electron travelling through the narrow channel, may suffer back scattering then part of the total current gets back to the source. Therefore the equation 2.105 shall be written in therms of the electronic transmission probability in the channel T_n then,

$$\vec{J_n} = \frac{2}{h}\delta\mu \sum_{n=1}^{N} T_n. \tag{2.106}$$

Where we have considered a twofold degeneracy for spin and a single valley in this case, N is the number of channels (modes) accessible for electronic transport in the device. Recurring to the fact that, $\delta\mu = \frac{\delta n}{\rho(E_f)}$ and $\vec{J} = \tilde{\mathrm{D}}\delta n$ we may write the Eq. 2.106 as,

$$\tilde{\mathrm{D}}\delta n = \tfrac{2}{h}\tfrac{\delta n}{\rho(E_f)} \textstyle\sum_{n=1}^{N} T_n. \tag{2.107}$$

Thus isolating $\tilde{\mathrm{D}}$ from Eq. 2.100 and replacing into Eq. 2.107 we have,

$$\frac{G}{e^2\rho(E_f)}\delta n = \frac{2}{h}\frac{\delta n}{\rho(E_f)} \sum_{n=1}^{N} T_n.$$

Finally the conductance G is given by:

$$G = \frac{2e^2}{h} \sum_{n=1}^{N} T_n. \tag{2.108}$$

The equation 2.108 is the *Landauer formula* for the ballistic transport.

2.5.1 Green's Functions Formalism

Looking at Eq. 2.108, we see that it is dependent on the electronic transmission, which is the probability of an electron with a given energy, injected in a lead to be transmitted to another lead. Lets make our model simple, thus dividing the entire system in three basic regions, as shown in Fig. 15. The conductor (C) is represented by the

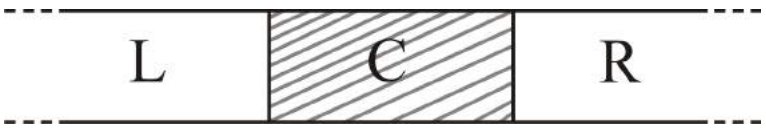

Figure 15: Simplified model, for a system formed by two contacts (L and R) separated by a conductor (C).

shaded area in Fig. 15, it is attached to the left semi-infinite lead (L) and to the right one (R). The method presented here may be applied for a generic Hamiltonian matrix, obtained from numerical orbital basis functions, as suggested in Ref. [65]. Therefore the entire matrix may be splitted in sub matrices for each singular part of the device. Thus the transmission in 2.108 is given in therms of the Green's functions as the trace from the resulting matrix, according:

$$T = Tr(\Gamma_L \mathfrak{G}_C^r \Gamma_R \mathfrak{G}_C^a). \tag{2.109}$$

In Eq. 2.109, $\mathfrak{G}_C^{r,a}$ are the retarded and advanced Green's function related to the conductor therms, also $\Gamma_{L,R}$ are the coupling matrices between the leads and the conductor. Thus the Green's functions for the entire system may be obtained as,

$$(\epsilon - H)\mathfrak{G} = I. \tag{2.110}$$

Where H is the Hamiltonian matrix for the entire system, $\epsilon = E + i\eta$ in this case η is a small valued and arbitrary defined term, finally I is the identity matrix. Whether the basis set for each atom in the system is known, and the atoms are geometrically arranged in such way that the atoms are sort as atoms from left lead, atoms from conductor and atoms from the right lead. Then the entire H matrix may be seen as composed by block related to the different areas of the device, as illustrated in Fig. 16. Mathematically one may write, the matrix equation as,

$$\begin{pmatrix} G_L & G_{LC} & G_{LCR} \\ G_{CL} & G_C & G_{CR} \\ G_{LCR} & G_{RC} & G_R \end{pmatrix} = \begin{pmatrix} (\epsilon - H_L) & H_{LC} & 0 \\ H_{LC}^\dagger & (\epsilon - H_C) & H_{CR} \\ 0 & H_{CR}^\dagger & (\epsilon - H_R) \end{pmatrix}^{-1}. \tag{2.111}$$

In Eq. 2.111 $(\epsilon - H_C)$ stands for the conductor hamiltonian matrix, while $(\epsilon - H_{R,L})$, are related to the semi-infinite leads and H_{CR}, H_{LC} represents the coupling matrices between the leads and the conductor. Therefore, the Green's function for the conductor is taken

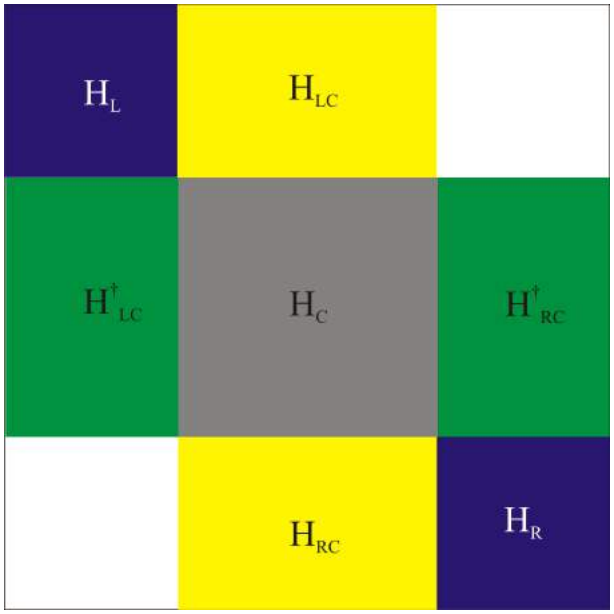

Figure 16: Schematic representation of the block Hamiltonian matrix, when the basis set of every atom is known and the ordering of the atoms is performed as described in the text.

from the matrix equation above [66], and it is written as:

$$\mathfrak{G}_C = (\epsilon - H_C - \Sigma_L - \Sigma_R)^{-1}. \tag{2.112}$$

Where, $\Sigma_{L,R}$ are the self-energy terms, associated to the semi-infinite contacts, and they are defined as, $\Sigma_L = H_{LC}^{\dagger}\mathfrak{g}_L H_{LC}$ and $\Sigma_R = H_{RC}^{\dagger}\mathfrak{g}_R H_{RC}$, with $\mathfrak{g}_{L,R} = (\epsilon - H_{L,R})^{-1}$. After obtaining all the Green's functions of the system, the coupling functions $\Gamma_{L,R}$, may be computed as:

$$\Gamma_{L,R} = i(\Sigma^r_{L,R} - \Sigma^a_{L,R}), \tag{2.113}$$

the advanced and retarded self energies $\Sigma^{a,r}_{L,R}$ are related as $\Sigma^a_{L,R} = (\Sigma^{r\dagger}_{L,R})$.

3 ELECTRONIC TRANSPORT THROUGH HEXAGONAL BORON NITRIDE CLUSTERS

In the past fifteen years two-dimensional materials have attracted attention from researchers in different areas such as Physics, Chemistry, and Materials Sciences. Ever since graphene was first isolated by Novoselov and co-workers [8], its outstanding properties, such as its high thermal conductance and charge carrier mobility have been widely studied [11, 17]. Moreover, it has been found that two-dimensional films can be obtained for other layered materials, such as hexagonal boron nitride (h-BN) [67, 68] or transition metal dichalcogenides [69, 70], and even from non-layered structures such as silicene [71], phosphorene, [72, 73] and stanene [74]. Among these 2D materials, h-BN stands out for its similarities to graphite. Each h-BN layer is composed by boron and nitrogen atoms arranged hexagonally in a honeycomb structure similar to that of graphene [3]. In spite of these similarities, the electronic properties of single-layer h-BN are drastically different from that of graphene. The electronic gap in h-BN is larger than 5.0 eV [3, 75], which characterizes it as an insulator.

Recently, the growth of hexagonally shaped h-BN islands was reported in the literature [76]. Furthermore, interesting experimental works have been reported for the successful synthesis of heterojunctions between graphene and h-BN domains. [77–79] These experimental results draw attention to the possibility of the design and fabrication of different hybrid systems with interesting electronic and transport properties. This is specially important in view of the fact that, although the silicon technology has dominated the practical applications in electronics for the past sixty years, a quantum barrier for the miniaturization of silicon based devices is soon to be reached, implying the need for the development of different solutions for improved electronic technology [80]. In this sense, modelling new electronic devices have been the aim of many theoretical studies, in order to find a possible replacement of silicon in such practical applications [81]. In the 70's, Aviram and Ratner [82] proposed the molecular junction rectifier, in which a single molecule presented diode characteristics, drawing attention of both experimental and theoretical physicist to the molecular electronic transport, [83] and opening new opportunities for studying electron transport in small-scale quantum systems.

Theoretical calculations predict that, separately, both graphene nanoribbons GNRs and boron nitride nanoribbons (BNNRs) can show spin dependent properties depending on the nanoribbon width and on how the dangling bonds in the edges of the ribbon are passivated [84–86]. For instance, band structure calculations of zigzag GNRs were

found to have an anti-ferromagnetic(AFM) ground state, and may present a half-metallic behaviour depending on the magnitude of the applied transverse electric field. [87,88] On the other hand, zigzag BNNRs are known to have a nonmagnetic ground state when their edges are passivated with hydrogen, [89] but may present magnetic properties in the case unpassivated edges. [90]. Additionally, density functional theory (DFT) calculations have predicted that a metallic behaviour is expected for BNNR if the dangling bonds at the edges are passivated either by either sulphur or oxygen [86]. Half-metallic behaviour can also be found in a BNNRs when only the boron edge is passivated by hydrogen, while the nitrogen edge is left bare. [91]

The properties of these nano-materials are very sensitive to the shape, edge functionalization, doping and external perturbations [88, 90–93]. The structural similarities between graphene and h-BN, combined with their dissimilar electronic properties, allow for the formation of stable hybrid systems that give rise to new electronic properties with novel electronic and spintronic applications. It has been shown that the hetero-junction between a zGNR and a zBNNR can act as a spin filter, presenting magneto-resistive effects [94]. Our work aims at obtaining a better understanding about the electronic and transport properties of systems based on graphene/h-BN hetero -junctions. Specifically, we study hexagonally shaped BN clusters embedded either into a 6-zGNR (zigzag-GNR) or a 11-aGNR (armchair-GNR). The electronic structure of these systems were calculated using DFT, and from these calculations we could further study the structural and transport properties of these hybrid nano-systems.

The calculated results show that the conductance through the h-BN cluster is fully spin dependent for the zGNR contacts, while for the aGNR contacts a spin dependent conductance only appears when the inner BN core is substitutionally doped with carbon atoms, creating an excess or a deficit of electrons depending on which site the C atoms are placed. Furthermore, the presence of the dopant induces a ferromagnetic ground state to the device. Finally, the investigation of the effects of adsorbed O_2 and CO molecules onto the doped hybrid systems indicate the possibility of applications in spintronics. The following sections of this thesis are dedicated to give an explanation about the models and methods employed in this work, in the sequence the calculated results are presented and discussed. In the final section we highlight the conclusions of this work.

3.1 Model and Methods

The system studied in this work consists of a circuncoronene-like h-BN cluster [95], which is composed of 27 boron atoms and 27 nitrogen atoms ($B_{27}N_{27}$) forming the two different triangular sub-lattices which compose the complete hexagonal mesh of atoms.

By embedding this h-BN cluster into a GNR, we simulate a scattering region in the BNC device, where the leads are considered to be the semi-infinite GNR segments. The GNR can be either a 6-zGNR or a 11-aGNR depending on the orientation of the cluster in relation to the GNR periodic axis. In order to avoid reactive dangling bonds, all of the edges are passivated with hydrogen.

Figure 17 depicts the BN cluster embedded into the aGNR (bottom) and zGNR (top) The inset in Figure 17(a-d) shows the studied doping configurations for the central

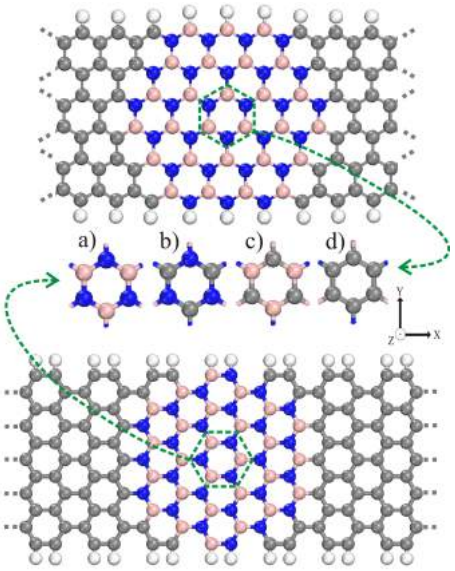

Figure 17: ($B_{27}N_{27}$) cluster embedded into the zGNR (top) and aGNR (bottom) contacts. The middle panel depicts four different configurations for the innermost hexagonal ring of the island, corresponding to (a) undoped **BN**, (b) negative doping **CN**, carbon substitution at boron site, (c) positive doping **BC**, carbon substitution at nitrogen site, (d) Complete substitution of the central ring by carbon atoms **CC**.

ring of the cluster. Figure 17 (a) shows the pristine ring configuration, while Figure 17 (b) shows the configuration on which the boron atoms in the central ring are replaced by carbon atoms. This configuration results in an excess of electrons in the π-orbital network. Figure 17 (c) shows the situation where nitrogen atoms are the ones replaced by carbon (which leads to a electron deficiency in the π bands) and Fig. 17 (d) depicts the configuration where the inner BN ring is totally replaced by C atoms, which restores the electron balance of the original system. For simplicity, we will use a reduced notation X_{YY}, where X=z or X=a represents the edge geometry of the GNR, and the subscript YY=BN, BC, CN, or CC represents the stoichiometry of the central ring in our BNC device.

The electronic structure calculations are carried out by means of the density functional theory [43, 44] as implemented in the SIESTA code [61], with exchange-correlation interaction calculated within the generalized gradient approximation (GGA)

Table 1: Lattice parameter (**a**) in the periodic direction for the systems studied in this paper.

System	**a** (Å)
Z_{BN}	54.088
Z_{CN}	54.088
Z_{BC}	54.088
Z_{CC}	54.088
a_{BN}	56.6
a_{CN}	56.6
a_{BC}	56.6
a_{CC}	56.6
$O_2@Z_{CN}$	54.088
$CO@Z_{BC}$	54.088
$O_2@a_{CN}$	56.6
$CO@a_{BC}$	56.6

parameterized by Perdew-Burke-Ernzerhof (PBE) [49]. The norm-conserving pseudopotential is employed in order to represent the inner core-electrons interactions, as proposed in the Troullier-Martins scheme [52] and the charge density is modeled using a 400 Ry mesh-cutoff radius to solve the integrals in the numerical grid. The wave functions are expanded in terms of double-ζ plus polarization orbitals (DZP) [58]. It is also important to mention that the spin contributions have been taken into account in all electronic structure calculations. Initially all electrons in the systems (including in the electrodes) are set with an Up spin, then they are allowed to relax during the self consistent field (SCF) cycle, which is considered converged when the difference between two SCF steps is bellow 10^{-4} eV. For each unit cell a vacuum distance of at least 15 Å was preserved between the mirror images in order to avoid spurious interactions along the non-periodic direction.

Due to the large size of the supercell, DFTB+ code was used for relaxing the atomic positions using the conjugated gradient algorithm for energy minimization [96,97], within the *matsci* parameterization [98]. Our analysis (not shown here) indicates that differences in the band structures calculations for BNC systems relaxed within DFTB+ approach and the SIESTA method are small. The structure is considered relaxed when the minimal force component drops below 0.01 eV/Å. For the structural relaxation, the Brillouin zone is sampled with a Monkhorst-Pack-like [99] grid using a $(10 \times 1 \times 1)$ k-grid. Additional information about the lattice parameters may be found in Table 1, where the lattice parameters are listed.

The electron transport calculations are carried out using the TRANSFOR code [100, 101] which uses the converged hamiltonian and overlap matrices from SIESTA

as a starting point. The used hamiltonian and overlap matrices can be separated into the contributions from both the region of the electrodes and the scattering region. After delimiting each sub-matrix responsible for the coupling terms contained in the original Hamiltonian matrix, we apply the Landauer-Büttiker formulation for ballistic transport [102]. Further information regarding the transport theory may be found in [65, 103–105] and in the references therein, a detailed description about the two probe model for ballistic transport is given in the next paragraph.

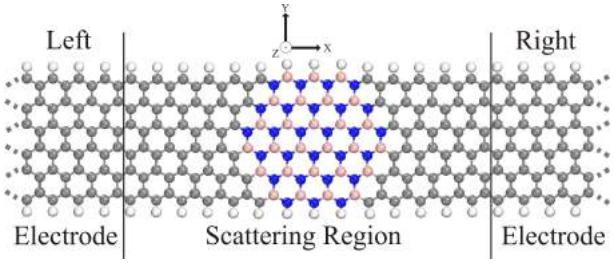

Figure 18: Schematic representation of the two probe device, employed in this paper.

Every conductance calculation presented in this work, has been carried out using a to probe model as shown in Figure 18. The entire supercell is periodic in the x direction and divided in three basic regions, the left electrode, the scattering region and the right electrode. A single electrode is composed by two principal layers (PLs), each PL is formed by four GNR primitive cells. Thus in the total, the length of the electrode is the same as in eight GNR primitive cells. The central region, is formed by the BN cluster embedded in the GNR, however it is important to consider the distance between electrodes, in order to avoid undesirable interactions between left and right. Thus at least four primitive cells are kept in both sides of the BN core as buffer region. After building the geometry, the relaxation and electronic structure calculations take their places as described in the methods section.

Also in order to verify the thermodynamic stability of the adsorbed molecules over the BN cluster, molecular dynamics (MD) calculations were performed under the Nosé thermostat procedure [106] and using the same DFTB+ parametrization set as applied for the structural relaxation of the hybrid systems, as mentioned above. The time step employed is equal to 1 fs and the simulation runs through over 1000 MD steps under a target temperature of 300 K. In the initial geometry, the molecules are placed 2 Å above the doped ring of the cluster.

3.2 Zigzag Systems

We start our discussion with the zigzag hybrid system. Figure 19 (a) shows the spin density distribution for the h-BN cluster inserted on a zigzag ribbon (6-zGNR). From

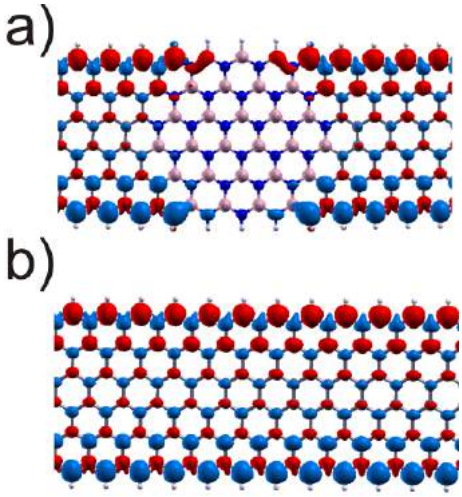

Figure 19: Spin density ($\rho_{up} - \rho_{down}$) for an hexagonal BN cluster inserted into a zGNR is shown in a), the spin density for the pristine zGNR is depicted in b).

this image we can see that the spin polarization vanishes at the BN core. For comparison, the spin density for the pristine 6-zGNR is shown in Figure 19 b). As expected, in both cases the zigzag graphene ribbon edges are spin polarized with the two borders showing opposite spins. It should be noted that the spin density plot, depicted in Fig. 19 b), the total density of states (DOS) and the conductance curves, shown as dotted lines in Figure 20 a) and b), for the pristine zigzag nanoribbon are in good agreement with previously published results [107, 108]. The presence of the BN cluster induces a break in the edge polarization, creating a spin-dependent scattering region for the electrons. This is in agreement with the high magneto-resistance predicted for graphene/BN junctions [94].

We follow up with the analysis of the carbon doped h-BN clusters on the zigzag edged nanoribbons. The density of states (DOS) and the conductance spectra related to the systems z_{BN}, z_{CN}, z_{BC} and z_{CC} are depicted in Figures 20 a-I), a-II), b-I), b-II), c-I), c-II) and d-I), d-II), respectively. For each case, we can observe a spin dependence in the transmission spectra, this difference in the spin components is mostly associated to the zigzag edges of the systems. For the z_{BN} system (20 a), on which we have an undoped h-BN cluster, it is possible to see that the conductance is highly dominated by the Down component, as evidenced by the wider peaks observed in the conductance spectra, Fig. 20 a-II) for the down component of the spin, with the up component being characterized by a very sharp conductance peak at around -0.7 eV.

The partial charge densities corresponding to the conductance peaks near -0.7 eV (red arrow) and 0.7 eV (blue arrow) are shown in Figures 20 a-IV) and a-III). For the Down component, Fig.20 a-III), it can be clearly seen that for the selected energy range the charge density is highly delocalized and extends over the entire scattering region, including the entire length of the boron edge of the cluster, thus bridging the two graphene

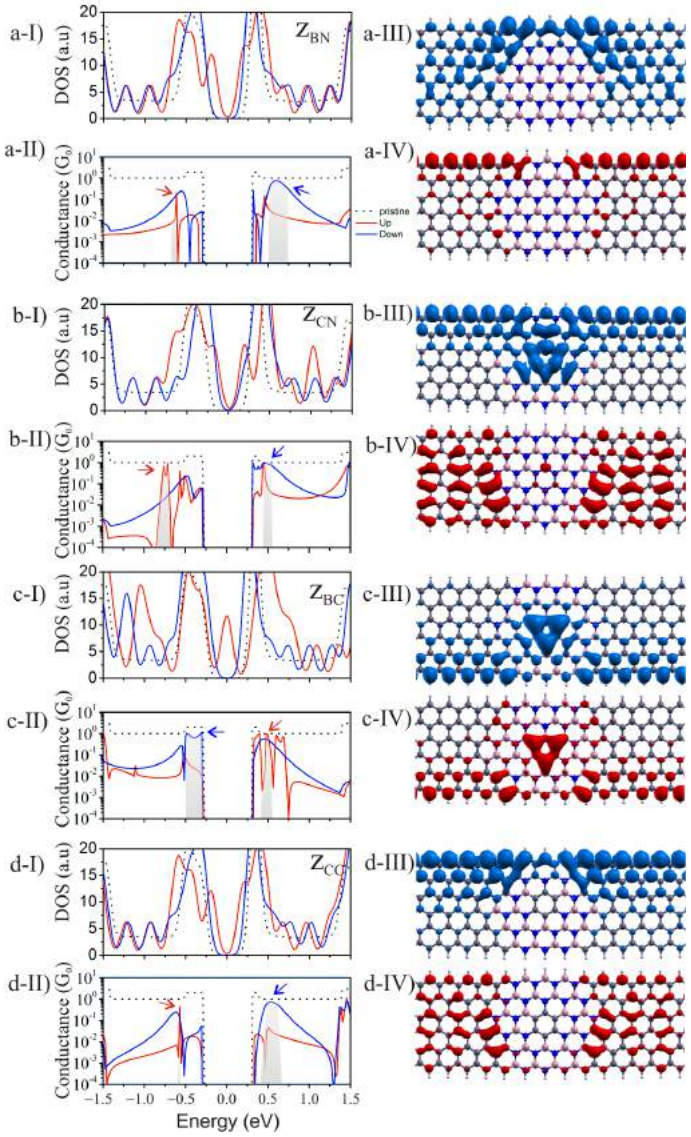

Figure 20: Density of States (I), conductance spectra (II) for the (a) Z_{BN}, (b) Z_{CN}, (c) Z_{BC} and Z_{CC} systems. We also show the Down (III) and the Up (IV) spin components of the charge density for energies near the regions of highest conductance peak for each of the systems. The selected energy range for each system is depicted by a shaded area in II. The DOS and the conductance spectrum of the pristine z-GNR are shown as doted black lines for reference. The Fermi energy is set to zero and the red and blue electronic clouds are related to the Up and Down spin components, respectively.

electrodes. This leads to the strong spin-Down conductance calculated for this energy. For the Up component, Fig.20 a-IV), the charge density vanishes completely at the h-BN cluster, so there is no efficient bridge between the two graphene electrodes, and the spin up conductance is weaker. The asymmetry in the Up and Down conductance reflects the combination of two factors: the spin polarization of the zigzag GNR with the edge asymmetry of the BN cluster, for which the edge near the Down component is terminated with boron atoms while the edge closer to the Up component is terminated with nitrogen atoms.

It is also interesting to note that the DOS for the BCN hybrid system is characterized by sharper localized peaks instead of the nearly continuous DOS obtained for the pristine ribbon (for example, see Fig. 3 a-I). This effect is related to the weaker interaction between the electrons on the different domains of the system, as previously reported on the literature [109–111].

The conductance for the z_{CN} system, characterized by a carbon substitution onto the B sites of the central BN ring, is displayed in Figure 20 b-II). It can be seen that for positive energy values the higher conductance peak is due to the Down component, while for negative values the major conductance peak is concentrated in the Up component. Since the carbon atoms have one electron more in their outermost electronic shell than the boron atom, we have increased the number of electrons in the innermost ring by 3 electrons, thus creating confined electronic states in the middle of the h-BN cluster. The strong difference in conductance for the negative and positive energy values can, in principle, be applied for a controllable spin filtering device. Also, the substitution of B atoms induces the entire system into a FM ground state, with a net magnet moment $\mu = 2.35\mu_B$ different from zero. The presence of the FM ground state is related to the lack of inversion symmetry of the BN cluster combined with the trigonal symmetry of the carbon doping configuration, which prevents an effective balance of the Up and Down spins.

There are two channels with a G_0 conductance for the Up component, indicating the presence of two different energy levels accessible for transport, one for negative electron energies (hole transport) and one for the positive electron energies (electron transport). On the other hand, the conductance for the Down component reaches its maximum values only for positive values of energy. The charge density plot for the Down component in this case, Fig. 20 b-III) shows that the conduction occurs through strongly delocalized states which spread from the center of the h-BN cluster to the B edge, thus involving the doped central ring.

For z_{BC} system, the carbon substitution is considered at the nitrogen sites, thus creating holes in the innermost ring, since now the C atom has one electron less than the N atom in its valence shell. As in the previous case, z_{BC} also presents a FM ground state, with magnetic moment equal to $2.99\mu_B$. The conduction plot for this system (Fig. 20 c-II) shows a Down component conductance with a set of peaks with $G \sim G_0$ on the negative energy side, while the Up component shows four sharp conductance peaks on the positive energy side. The DOS of the z_{BC} (Fig. 20 c-I) has a sharp peak centered at the Fermi energy for the Up spin component. However these states are localized onto the BN cluster and do not contribute to the conductance.

The last case for the zigzag GNR hybrid systems that we studied is the one on which we have the innermost ring totally substituted by carbon atoms (z_{CC}) Fig. 20 d-I,IV). This system has an AFM ground state and, at a first glance, does not present many changes near the Fermi level in comparison to the z_{BN} case. This is expected since they have the same number of electrons associated to the central ring. The main differences only occur for energies around 1.5 eV, where there was a considerable increase on both the Up and Down conductances as compared to the z_{BN} case. The partial charge densities associated with the conductance peak for the Down component (near 0.5 eV) and for Up component (around -0.55 eV) are depicted the Figure 20 d-III) and d-IV). It can be seen that they are very similar to those observed for the Z_{BN} system, implying that the main substitution of the inner BN hexagon by carbon atoms has very little effect on the electronic states and on the conductance of these systems.

In general, we can see that for the charge balanced systems (z_{BN} and z_{CC}), the conductance occurs mostly through one of the edges (the Boron terminated edge) of the cluster, while for the charge imbalanced systems (z_{CN} and z_{BC}), the electronic conducting states are found to pass also through the core of the BN cluster.

3.3 Armchair systems

Armchair graphene nanoribbons are known to have a spin degenerated ground state, exhibiting no ordered magnetism at the edges. This can be verified by observing Figs. 21 a-I) and b-I) in which we find that there is no spin dependent conduction for the a_{BN} and a_{CC} systems. An interesting effect comes into play when we introduce the carbon dopants into the central ring of the h-BN island. First of all, the calculated conductance for the a_{CN} system is fully spin dependent Fig. 21 c-II), showing discrete conductance peaks for the Up spin at approximately -0.3 eV, and one peak for the Down spin at around 0.3 eV. The DOS plot for both spins in the a_{CN} system are shown in Figure 21 C-I) both spin components have electronic states near the Fermi level. Such states nearby the Fermi energy do not contribute to the conductance of the junction as was also observed for the z_{BC} system. Figures 21 C-III) and 21 C-IV) show that the charge density related to the conductive states for the Down and Up spins are spread along the structure, but showing a large concentration near the center of the cluster due the charge localization caused by the doping charges. Again, the lack of inversion symmetry, together with the trigonal structure of the doping arrangement induces the formation of a FM ground state with a total magnetic moment of $\mu = 1.74\mu_B$ which, in turn, promotes the calculated spin polarized conductance. It is interesting to comment that this spin polarization is highly concentrated in the regions near the inner ring (a more detailed discussion of this effect

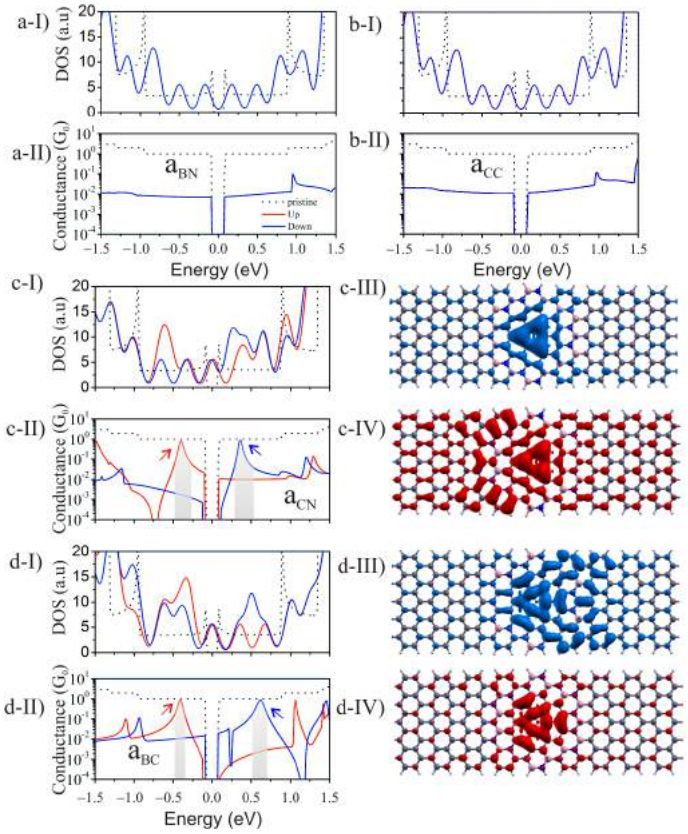

Figure 21: Figures a-I), a-II), b-I) and b-II) respectively represents the DOS and conductance spectra of a_{BN} and a_{CC}, systems. Figures c I to IV are showing the DOS, conductance, charge density for Down and Up peaks of the a_{CN} system, in the same order. Similarly Figures d I to IV are displaying the DOS, conductance, charge density for Down and Up peaks of the a_{BC} system.

can be found in the discussion of - Fig.22).

The a_{BC} system also shows a polarized conductance (Figure 21 d-I), for similar reasons. For both the a_{CN} and the a_{BC} devices the observed spin Up conductance peaks are related to states below the Fermi energy, while the spin Down conductance occurs mainly por positive values of energy. These results indicate the possibility of an electrostatic gate modulated spin valve [112, 113]. The charge densities for the peaks in a_{BC} system are shown in Figures 21 d-III) and d-IV) for both spin Up and spin Down. It can be seen from Figs. 21 d-III) and d-IV) that the charge densities are very delocalized through out the whole system, which justify observed the conductance peaks. Furthermore, the major part of the charge density is found to be spread over the innermost ring, thus leading to the expected conclusion that these transport peaks occur due to the coupling between electronic levels in the leads and in the h-BN cluster.

In order to clarify the origins of the spin splitting, we have plotted the partial density of states (PDOS) from the a_{CN} system, over the atoms which compose the doped BN cluster. Figure 22 shows the PDOS associated to different sets of atoms, which are

indicated by a color circle surrounding each atom of the set. In Fig. 22 a) the PDOS from the doping carbon atoms which are circled by green, is shown. We see that those atoms clearly present polarized states. Similar effects are seen for the nitrogen atoms bonded to the dopants, as well as for the atoms around the innermost ring of the BN core. However, the polarization is strongly suppressed for the BN atoms in the last shell of the cluster, as may be verified in Fig. 22 e). The PDOS is almost completely non-polarized, unless for some specific energies. Analysing the orbital contribution for PDOS (not shown), we have found that the polarization comes from the P_z component. This might be understood, from the fact that the electrons in P_x and P_y component are forming the σ-bond, thus due to the electron imbalance, there is one electron (or hole), weakly bonded to the atom, occupying the P_z orbital, then giving rise to the polarization.

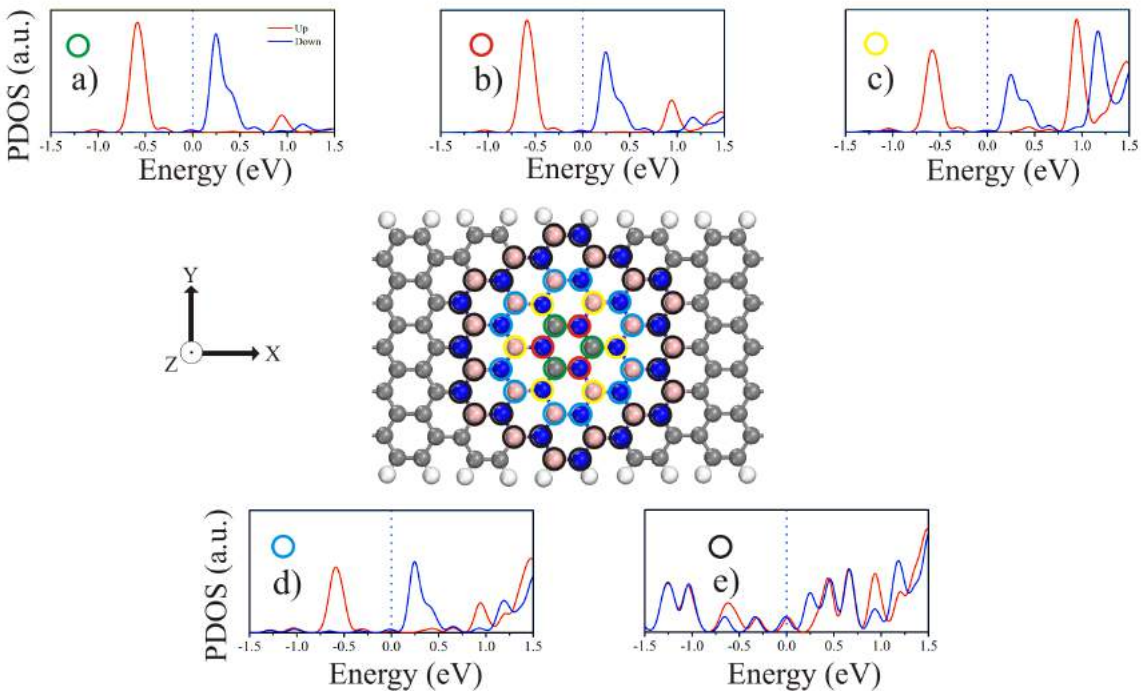

Figure 22: Partial density of states (PDOS), taken from a_{CN} system, the colored circle indicate the atoms which contributed for PDOS.

3.4 Spin Polarized Molecular Sensing

The observed spin-dependent transmission coefficient for the a_{CN}, a_{BC}, z_{BC} and z_{CN} systems, opens up the possibility of adsorbing different molecular groups onto the doped h-BN cluster. For that, we performed MD calculations which showed that O_2 and CO molecules are likely to adsorb onto the doped h-BN domain region. In view of this, we have chosen to focus on these two molecules. Specifically, we investigate the effects of adsorbing an O_2 molecule onto either the z_{CN} or the a_{CN} system, and

investigate the adsorption of a CO molecule onto the z_{BC} and a_{BC} systems. The choice of adsorbants/adsorbent pairs have based on the donor/acceptor nature of each system. For example, the systems in which the boron atoms are substituted by carbon atoms are donor like systems, thus being more appropriate for interacting with the O_2, which is a well known acceptor molecule. This prediction is also in agreement with our MD calculations for these systems. On the other hand, CO adsorption is expected to occur onto the systems in which we have C substituting the N atoms. These later systems have an acceptor-like nature and thus are appropriate for interacting with the CO molecule, which usually acts as a donor. Both the MD simulations and the DFT calculations corroborate these assumptions. The final geometry of the adsorbed systems are shown in Fig. 23.

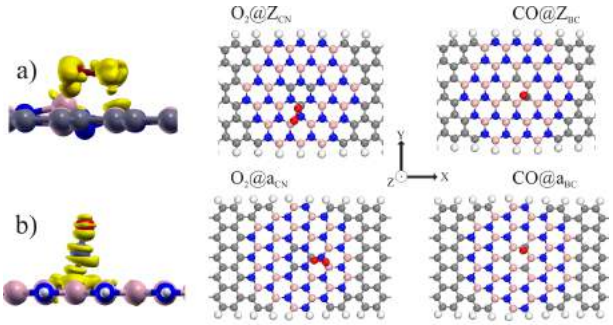

Figure 23: Adsorbed systems studied in Figure 24 of this chapter.

The adsorbed structures studied in Figure 24 of this chapter are shown in Fig 23. The charge transfer $\Delta\rho$ is shown in Fig. 23 a) and b) for $O_2@Z_{CN}$ and $CO@Z_{BC}$ in this same order. The charge difference is given by,
$\Delta\rho = \rho_{ads} - \rho_{rib} - \rho_{mol}$, where ρ_{ads} is the charge density of the adsorbed system, ρ_{rib} is the charge density of the substrate and ρ_{mol} is the charge density of the molecular group. For this analysis in order to minimize the basis set superposition error (BSSE) we have employed the ghost atom technique. From this density plots we may conclude that there were a chemisorption of the molecular system over the BN core. It might be understood from the fact of the existence of a electronic imbalance in those systems, in other words, there are localized charges in the neighborhood of the innermost ring of the core (electrons or holes). In the O_2 adsorption onto electron-reach systems $O_2@Z_{CN}$ and $O_2@a_{CN}$ is found that O_2 attaches to the systems, from a carbon atom in the innermost ring to a boron atom in a outer BN bond. In the other hand, the CO adsorption onto electron-deficient systems $CO@Z_{BC}$ and $CO@a_{BC}$, the CO molecule binds to a carbon atom in the innermost ring. A vertical position of the CO molecule in relation to the GNR plane is also observed in both cases.

Figure 24 a) displays the conductance for pristine z_{CN} and for O_2 adsorbed

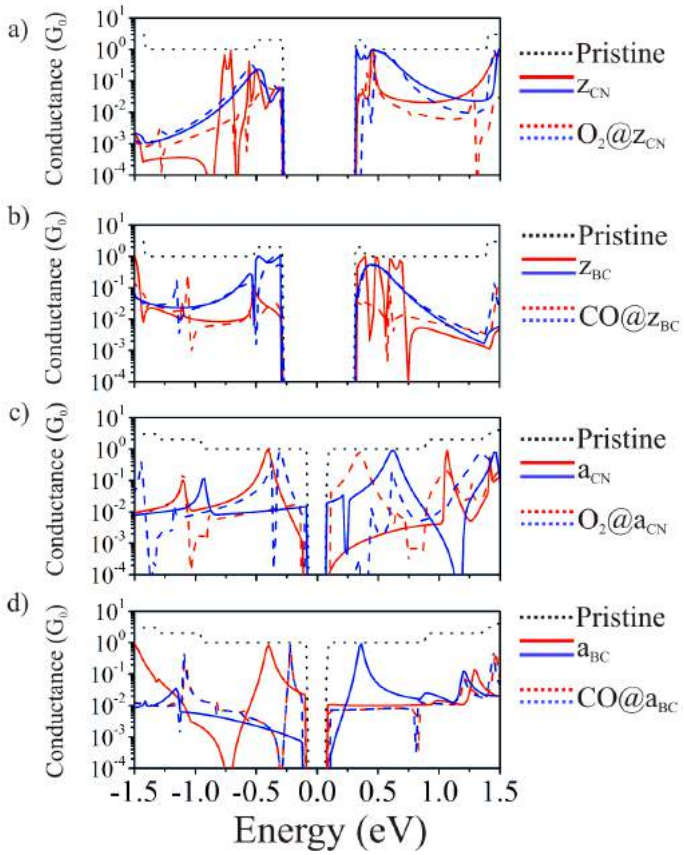

Figure 24: Spin polarized conductance and DOS for molecular groups adsorbed in the different devices, O_2 molecule were adsorbed in the systems z_{CN} and a_{CN} thus the new systems being labeled as O_2 @z_{CN} and O_2 @a_{CN} respectively. The red and blue color are associated to the Up and Down spin components in the same order. The solid line refer to a device without adsorption as the dashed line refers to a system in which there were adsorption of a molecular group. In the same way carbon monoxide molecule were adsorbed at z_{BC} and a_{BC}, therefore the new labels are $CO@z_{BC}$ and CO @a_{BC}.

onto z_{CN} ($O_2@z_{CN}$). As in the previous figures, Up and Down spin components are shown in red and blue respectively. It can be seen that for the Up spin component the conductance is strongly reduced.

For a more quantitative analysis we show in Table 2 the values of $\Delta I(e,h) = (I_{ad} - I_0)/I_0$ for the different studied systems. Here I_0 and I_{ad} are obtained by integrating the calculated conductances of the system before (I_0) and after (I_{ad}) the molecular adsorption. For electron conduction (e), the conductance is integrated from Ef to 1.5 eV, while for hole (h) conduction the integration is performed between Ef and -1.5 eV. Negative ratios indicate a drop in the quantum conductance for the system with the adsorbed molecule relative to the system without the molecule. On the other hand the positive ratios indicate a increase in the quantum conductance due to the molecular adsorption. The overall decrease in quantum conductance for the $O_2@z_{CN}$ system may be understood as the effect of the charge transfer between the adsorbate molecule and the z_{CN} system

due the high electronegativity of the oxygen atom. However, the conductance for the Down spin slightly increases in the negative range of energies, however this increase is small compared to the overall result.

We now move to the CO adsorption. The conductance spectrum for CO adsorbed onto the Z_{BC} device ($CO@z_{BC}$) is shown in Fig. 24 b). It can be seen that the Up spin component is greatly reduced compared to the z_{BC}, specially for energies near the Fermi level. On the other hand, the transmission for the Down component does not change much for the positive energies, indeed it has increased slightly by 2% in comparison to the case without the molecular adsorption. As it can be seen, the effects of both O_2 and CO adsorption onto zigzag type devices leads the system to a considerable loss in the quantum conductance specially for energies below the Fermi level.

The most striking results are found, however, for the adsorption of O_2 and CO molecules onto the armchair edged devices. For instance, in Fig. 24 c) it is possible to see that the O_2 adsorption shifts the Up spin transmission from being mainly hole-based to being basically mediated by electrons. This is evidenced by the observation that for the a_{CN} system (solid red line) the Up spin conductance peak is on the left (negative) side of E_F, while for the $O_2@a_{CN}$ (solid dashed line) the Up spin conductance is on the right side of E_F. The opposite behavior is seen for the Down spin component Fig. c) (solid and shaded blue lines), where the conductance shifts from electron-based to hole-based upon the O_2 adsorption. We thus conclude that the adsorbed O_2 molecule induces a change in quantum conductance behavior, since if we consider that an application of a gate bias could shift the Fermi level to energies -0.5 eV, we would have a spin Up polarized current before the adsorption, then after adsorbing the molecule, the electronic current would mostly be due the Down component. This effect can be better quantified by observing Table 2, where is is seen that the Up component current for the negative energy values (Ih) decreases by 79% while the Down component has a 3-fold increase. Also, for positive energy values the Up component increases 130% together with a small decrease on the Down component current. The observation of such a switch in the spin conductance with the O_2 adsorption indicates that the magneto-resistivity of this system can be controlled by the molecular adsorption. Magneto-resistivity have been reported for BNC hetero-junctions, as discussed in Ref. [94], where the effect is dependent on the polarization of the device edges. From the theoretical point of view our results are very exiting since they suggest the application of such systems in spintronics, such as in spin valves in which molecular groups could be employed to turn on/off the devices.

For the $CO@a_{BC}$ system the effect is again very different from the other cases. The CO adsorption removes most of the spin polarization of the system, specially near

Table 2: Comparison in percentage of the linear response current, at ±1.5 V, between the systems which suffered adsorption and its original ones. Also the magnet moments for the systems before (μ_0) and after (μ_{ad}) adsorption is shown.

	ΔIh		ΔIe			
	Up	Down	Up	Down	$\mu_0(\mu_B)$	$\mu_{ad}(\mu_B)$
$O_2@z_{CN}$	-79%	34%	-74%	-27%	2.35	0.97
$CO@z_{BC}$	-42%	-32%	-89%	2%	2.99	0.94
$O_2@a_{CN}$	-79%	332%	130%	-13%	1.74	0.80
$CO@a_{BC}$	-70%	374%	37%	-59%	1.82	0.04

the Fermi energy. This is evidenced by the fact that for the adsorbed system the magnetic moment decreases to 0.04 μ_B, leading to a considerable degeneracy spin up and spin down states. Considering the original spin polarized effect, this result also indicates a strong spin valve effect specially for energies below the Fermi level, for which the CO adsorption causes a considerable decrease on the Up component of the current and almost 4-fold increase on the Down component.

3.5 Conclusions of This Chapter

In summary we have studied a hexagonally shaped h-BN cluster embedded into armchair and zigzag graphene nanoribbons. We have observed that the insertion of the hexagonal h-BN cluster onto the zigzag edged ribbon creates a single spin polarized channel for charge transport localized near the edges of the nanoribbon. No spin polarization was found for the armchair edged devices without doping. We have also shown that the substitutional doping of carbon into the innermost atomic ring of the cluster leads to different regimes of quantum conductance even for the studied armchair edged systems. For instance, the carbon substitution into either the B or the N site led the armchair edged devices to show a spin dependent conductance spectra on which the Up spin is mainly associated with hole-based conductance and the Down spin with electron-based conductance. Finally, we have also studied the effects of oxygen (O_2) and carbon monoxide (CO) molecule adsorption onto the carbon doped devices (the a_{CN}, a_{BC}, z_{BC} and z_{CN} systems). The molecular groups were shown to be responsible for a loss in the net magnetic moment in the zigzag devices, leading to a considerable decrease in the quantum conductance for these systems. For the armchair edged devices, the molecular adsorption was found to greatly affect the spin polarization of the systems with a considerable decrease in the conductance. Furthermore, we observed that for the a_{BC} system, the O_2 adsorption causes a spin polarization switch between hole and electron conduction. The Up component switches from hole-based conductance to electron-based conductance, while the Down component behaves on the opposite way.

The properties observed for these systems may be suitable for applications as molecular sensors and also for spintronics. This work could be a good starting point for further theoretical studies and novel experimental developments in this area.

4 ELECTRONIC TRANSPORT IN MOS2/WS2 NANORIBBONS

The quest for device miniaturization and smaller dissipation of energy has led the electronics industry to face a quantum barrier for silicon technology applications [114]. Researchers suggest that the next generation of field effect transistors (FETs) should be scaled down to under 5 nm [115]. New possibilities for electronic device designs have emerged after the isolation of graphene, in 2004 by Novoselov *et al* [116], and the boost in the research of other two dimensional materials that followed it. One of the shortcomings of graphene that strengthened the research of other two dimensional materials is the lack of a band gap in the electronic structure of graphene, which prevents its application in devices where high switching ratios are needed. One of the classes of 2D materials with a large potential for applications in this area is that of the transition metal dichalcogenides (TMDCs). [117] The TMDC class is composed of more than forty different systems that are crystallized as layer stacked Van deer Walls materials [118]. Such stacking favors the peeling off of a few or even only a single layer of the bulk form of TMDCs. Each TMDC layer is composed of an atomically thin layer of a transition metal **M** placed between two other atomically thin layers of a chalcogen atom **X**, thus a general formula for the TMDCs may be written as MX_2. Depending on the choice of the transition metal and of the chalcogenide, the TMDC can be either metallic, semiconducting or insulating.

For electronic device applications, four family members have attracted a larger share of the attention, namely the MoS_2, $MoSe_2$, WS_2 and WSe_2 systems. It is well known that these materials, in their bulk form, are semiconductors with a considerably high indirect band gap. However, it has been predicted by *ab-initio* calculations that for a single layer of these materials a direct band gap emerges. [119,120] The band gap transition has been confirmed experimentally for monolayer MoS_2 by observing the intensification of its photoluminescence in comparison to the bi-layer, and bulk systems, [121] and also by Angle-Resolved Photoemission Spectroscopy (ARPES) measurements [122]. Similar studies regarding WSe_2 may be found elsewhere in the literature [123–125]. Another interesting feature associated to these TMDCs cited above is that a considerable spin splitting is also predicted for the electronic bands, specially at the K-point of the Brillouin zone [119,120]. This property highlights these bi-dimensional crystals as strong candidates for applications in the fast developing field of spintronics.

The recent proposal of different approaches which may allow for the controllable synthesis of MoS_2 nanoribbons (MoS_2NRs), one based on an etching technique [126] and the other based on a top-down fabrication method [127], brings forth the possibility

of the development of electronic and spintronic devices composed of TMDC nanoribbons. Thus, in this work we study the transport properties in zigzag MoS_2 and WSe_2 nanoribbons, using an effective tight-binding method based in the Slater-Koster simplification for LCAO. The quantum conductance is calculated using the Landauer-Büttiker formalism. The choice of the two specific TMDCs is based on the fact that both MoS_2 and WSe_2 have been applied effectively as active materials in electronic devices. [115, 128–130] The transport properties of these systems were also studied when a choice of experimentally observed defects was inserted onto the edges of TMDC ribbons [131] Our results reveal that the low-energy electrons always flows through the borders of the ribbons independently of the presence of edge defects. Furthermore, our results suggest that defective ribbons could be applied as tunneling diodes.

4.1 Model and Methods

Our TB model is based on the Slater-Koster (SK) Approach for the LCAO method [132], considering first neighbors only. A sp^3d^5 basis set is chosen to represent the atomic orbitals. The hamiltonian and overlap matrices are generated with our in-house program, and our calculations are based in the method as described in Ref. [133]. The SK parameters required for the hopping and overlap integrals for MoS_2 are the same published previously [133]. In order to study the electronic transport in our systems we take either a 8z-MoS_2NR or 14z-MoS_2NR. This nomenclature is further explained in Ref. [134], as the semi-infinite contacts attached to the left(L) and right (R) of the scattering region, a schematic representation of this setup is shown in Figure 25. Each L - R lead is composed by eight primitive cells of the nanoribbon. The conductance calculations are performed within the Green's functions formalism using the Landauer-Büttiker approach for the coherent electronic transport [102]. For this we have used the TRANSFOR code, which has been successfully employed in previous works [101]. Further information about the method may be found in refs. [100, 105] and in the references therein.

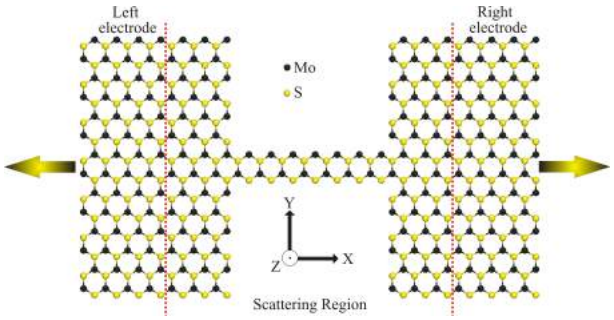

Figure 25: Schematic representation for a scattering region attached to semi-infinite electrodes, left (L) and right (R).

For comparison, DFT calculations were carried out for a defect-free 14z-MoS_2NR using the SIESTA [49] method employing the generalized gradient approximation (GGA) as proposed by Perdew–Burke–Ernzerhof (PBE) for the exchange-correlation term [135]. For these calculations, a double zeta plus polarization orbitals basis set (DZP) is employed in order to expand the wave functions. The mesh -cutoff is set to 200 Ry in order to solve the numerical integrals. A distance of at least 15 Å is kept in the non-periodic directions in order minimize spurious contributions from the mirror images. A Monkhorst-Pack like grid [136] with 20 k-points in the periodic direction was adopted, the calculation were considered converged when the difference in energy in the minimization steps drops below 10^{-4} eV.

4.2 Results

In order to validate our in-house program, we first perform a band structure calculation (using the same methodology as in Ref. [133]), for both single layer (1L) and bi-layer (2L)MoS_2, as depicted in Figure 26. In this figure the Fermi level is shifted to zero and represented by a blue doted line. In Figs. 26 a) and d) the full red lines represent the respective energy dispersion for 1L and 2L as calculated using our sp^3d^5 tight-binding approach, while the full blue line represents the energy dispersion calculated with DFT-HSE. As previously published. The agreement by DFTB and DFT methodologies is excellent [133]. As expected, for 1L the band gap of approximately 1.79 eV is located at the K point, in a very good agreement with the DFT-HSE calculated value of 1.78 eV. However it is still underestimated in comparison to the experimental value of 1.90 eV, [137] this discordance between measured and calculated band gaps, are due to the well known problem related to the exchange therms used in DFT calculations [138]. For 2L-MoS_2 the TB calculated band gap is 1.51 eV also slightly below the experimental value, measured at 1.60 eV Ref. [137]. The Figures 26 b) and e) depict the density of states (DOS) for 1L and 2L, while Figures c) and f) represents the conductance spectra for 1L and 2L, respectively. In both cases, the conductance presents a gap, as expected. However, the conductance for the bi-layer case shows conductance peaks approximately twice as large as in the mono-layer case. This is expected since for the 2L case the conductance channels are doubled in relation to the 1L case. The transmissions shown in Figures 26 c) and f) indicate the potential of application of both arrangements as electronic devices such as field effect transistors, or in the mono-layer case also applications in optoelectronic devices and as active elements in solar cells [139, 140]. Finally, in the inset g) the band structure for the WSe_2 monolayer is shown. The direct band gap at the K point of the Brillouin zone is calculated with our approach as being 1.74 eV, on the other hand the spin coupling

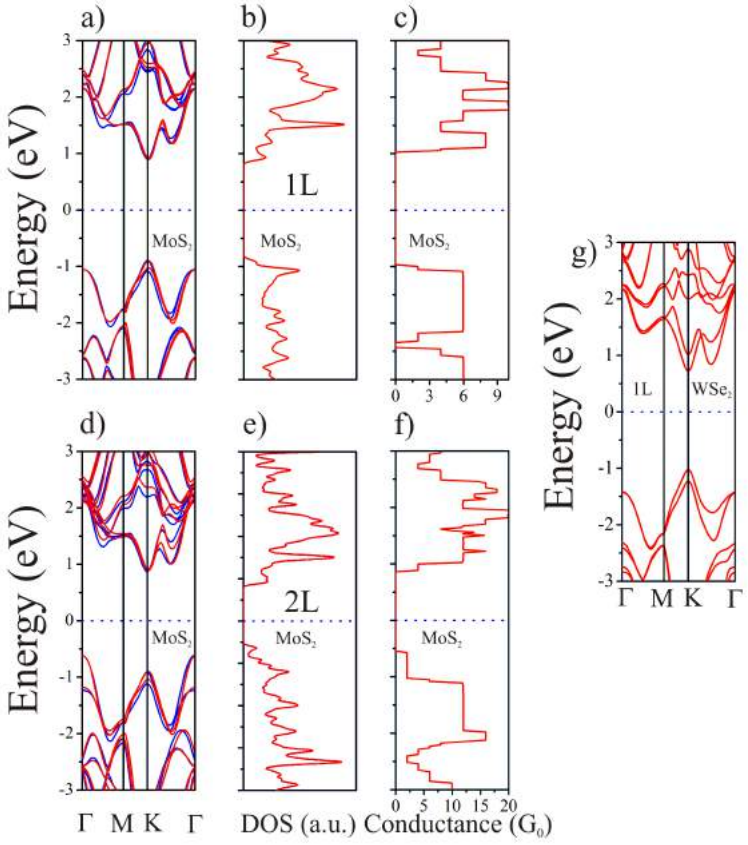

Figure 26: Band structure, density of states and conductance spectra for MoS_2 monolayer a), b) and c) in this same order, and for a MoS_2 bi-layer d), e) and f). The Fermi energy is placed in zero, being represented by a blue dotted line. The inset g) depicts the band structure calculated for WSe_2 monolayer.

splitting is calculated as 203 meV.

Figure 27 shows the DOS of a 14z-MoS_2NR calculated using both a full DFT calculation with a GGA-PBE functional (solid blue line) and our DFTB model (solid black lines). It can be seen that for the region near the Fermi energy (defined at 0 eV) the two curves are in good agreement, both predicting a metallic behavior for the 14z-MoS_2NR with a nearly constant density of states. This indicates that our tight-binding model can be used to properly investigate the transport properties of these systems. We also show in Fig. 27 the partial density of states (PDOS), calculated using DFT, for the atoms in the edges (light red shaded area) and for the atoms at the center of the ribbon (light blue shaded area). It can be seen that the states near the Fermi energy are mainly due to the atoms located in the edges, while the atoms at the center only contributes with electronic states far from the Fermi energy. Such significant feature predicted within the DFT theory is also captured by our TB method, which shows that the local current in these systems always flows along the edges, as it will be discussed later.

The proposed DFTB approach can then be used for calculating the quan-

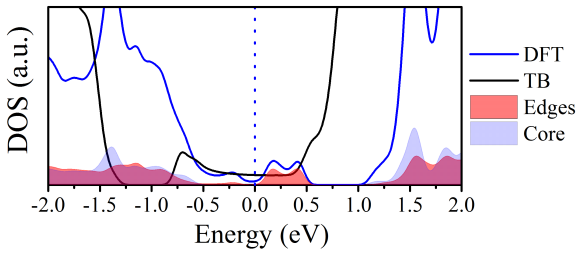

Figure 27: Density of states calculated by DFT (solid blue line) and using our TB method (solid black line). DFT calculated Partial density of states (PDOS) for atoms at the edges of the ribbon (light red area) and at the center of the ribbon (light blue area) are also shown. The dotted blue line represents the Fermi level in this plot, as well as in the following Figures.

tum conductance properties of MoS_2 nanoribbons. For that, we start by calculating the conductance of a pristine 14z-MoS_2NR which is displayed in Figure 29, and subsequent figures, as a black doted line. This result is obtained considering the semi-infinite leads to be composed of the same MoS_2 ribbon structure and is taken as reference for the calculations of the defective ribbons discussed below.

Figure 29 a) shows the quantum conductance plot for a defective NR on which one MoS_2 triplet is removed from one of the edges. There are, however, two possible structures. In the first, the defect triplet is removed from the metal-terminated edge, labelled as T1 (red line). The other structure is obtained by introducing the triplet vacancy on the chalcogen-terminated edge , labelled as T2 (blue line). Figure 28 show in detail the respective geometries. Our results show that lack of inversion symmetry in the pristine ribbon leads to different shapes for the defective conductances depending on the position of the defect in either of the edges. The conductance curve associated to the pristine ribbon exhibits a conductance plateau at $4G_0$ for energies near the Fermi level corresponding to contributions from both edges. This is evidenced by the local current plots for -0.25 and 0.25 V shown in Figure 29 d) and e), respectively, showing high current densities along both edges. Furthermore, as discussed above, the current flow is localized near the edges, which agrees well to the PDOS results in Fig. 27, where we observed that the charge carriers for energies close to the Fermi level are due to edge states. It can be seen that the conductance for the defective systems shown in Figure 29 a) is always higher than $2G_0$ since for both structures one of the edges remains intact. A small conductance peak is observed at -0.32 eV for the T1 system and -0.50 for T2 structure. These conductance peaks are due to resonant states associated to the triplet vacancy, causing a constructive interference with the electronic states on the leads.

The basic defective devices considered in this paper for MoS_2/WSe_2 nanoribbons are depicted in Fig. 28. Inset a) depicts the pristine ribbon, in b) the lack of a triplet

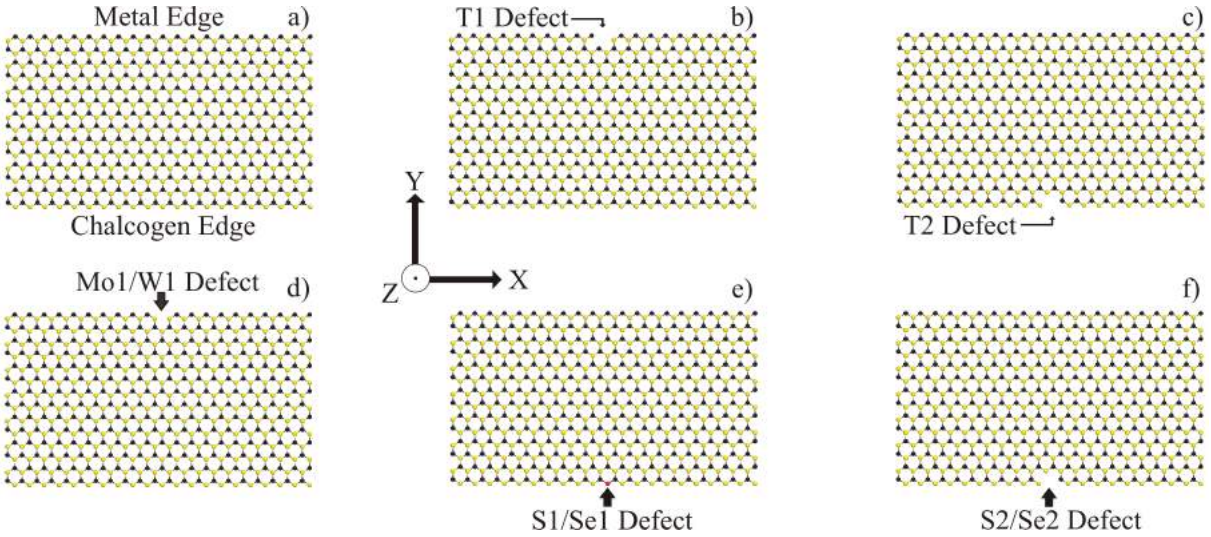

Figure 28: Pristine ribbon and basic defective geometries considered in this paper, for either MoS_2 or WSe_2

in the metal edge of the ribbon (T1) is shown, the opposite triplet vacancy is shown in c) at the chalcogen edge. In d) the monoatomic vacancy in the metal edge is represented, while e) and f) are standing for the monoatomic vacancy in the chalcogen edge, and the diatomic vacancy of the chalcogen in the edge. The red sphere in e) stands for the bottom layer of chalcogen, which is kept unchanged for this defect. In our calculations the periodic boundary conditions are applied in the periodic axis of the ribbon.

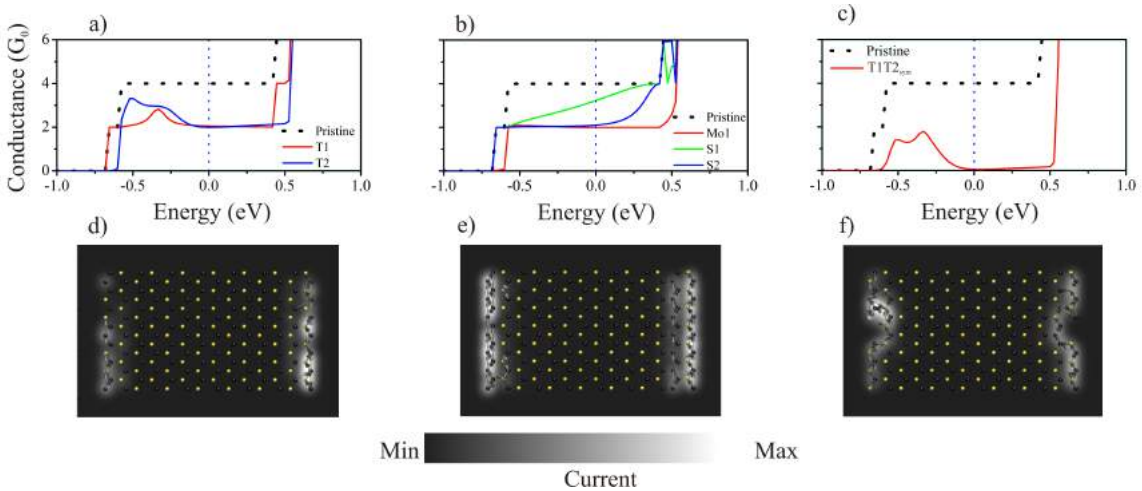

Figure 29: (a) Conductance curves for triplet defects in the metal edge of the ribbon (T1-red line) and in the chalcogen edge (T2-blue line). (b) Conductance curves for the vacancy of a single Mo atom at the metal edge and the single vacancy and di-vacancy of S atoms in the chalcogen edge are considered, these defects are labeled as Mo1, S1 and S2 in this same order.(c) Conductance curves for a system with the T1 and T2 defects symmetrically combined ($T1T2_{sym}$). In (a), (b) and (c) the quantum conductance for pristine 14z-MoS_2NR is shown as a black dotted line, for comparison. (d) and (e) show the local current for the pristine conductance (black doted line) for -0.25 and 0.25 V. (f) shows the local current for the systems containing MoS_2 triplet vacancies in both sides in the voltage of 0.33 V.

In Figure 29 b) three different types of defects are considered. First of all we consider a defect consisting of the removal of a single Mo atom from the metal-terminated edge (shown as red line and labeled as Mo1). For this defect, we observe that the absence of a single Mo atom in the edge already strongly reduces the conductance plateau to $2G_0$. Furthermore, the conductance peaks found for the T1 system are also absent in this case. Secondly, we have considered a structure on which only a single sulfur atom has been removed from the calcogen-terminated edge, shown as a green line in Fig. 29 b) and labeled as S1. For this system, although we observe a decrease in the conductance curve when compared to the pristine case, the effect is much less than that observed for the T1, T2 and Mo1 cases. Finally, we consider the removal of two symmetric S atoms in the chalcogen edge, thus creating defects on both the top and the bottom sulfur layers of the MoS_2 ribbon. This defect is labeled as S2 and the conductance curve is plotted in Figure 29 b) as a blue line. Similar to the Mo1 defect, the conductance has been strongly suppressed, also showing values of $2G_0$ for energies close to E_f. The conductance peak due to constructive interference also vanished in this case.

In Figure 29 c) we show the results for a combination of the T1 and T2 defects in the same device. The conductance curve for this case does not show the step-like shape seen in the previous cases, instead, it presents discrete conductance peaks, at -0.50 and 0.32 eV, which corresponds to the same energy peaks observed for the T1 and T2 cases. This change in the conductance shape is clearly due to the fact that in this case the conductance along both edges are seriously compromised. The two conductance peaks corresponding to molecular-like conductances involving the localized defect states. The local current plot for this configuration is shown in Figure 29 f), corresponding to the charge flow associated to the resonance peak at 0.33 eV.

Now we turn our discussion to the study of zigzag WSe_2 nanoribbons (z-WSe_2NRs). In Figure 30 we first observe that for the pristine 14z-WSe_2NR (black dotted line) the quantum conductance in the energy range between -0.50 and 0.50 eV is non-symmetric, presenting two conductance plateaus. One plateau going from around -0.5 eV to the Fermi energy (0.0 eV) with a quantum conductance of $2G_0$, and another plateau in the range between 0.0 to 0.5 eV with a conductance step of $4G_0$. It is interesting to note that the $2G_0$ plateau corresponds to a current which flows only along the metal-terminated edges, as can be seen in the local current density plot in Fig. 30 d), which was evaluated for an energy of -0.5 V. A similar current plot (not shown here) indicates that for a voltage of 0.5 V both edges are contributing to the current.

In Figure 30 a) we also show the conductance curve (red line) for a T1 defect, where a WSe_2 triplet has been removed from the metal-terminated edge of the ribbon.

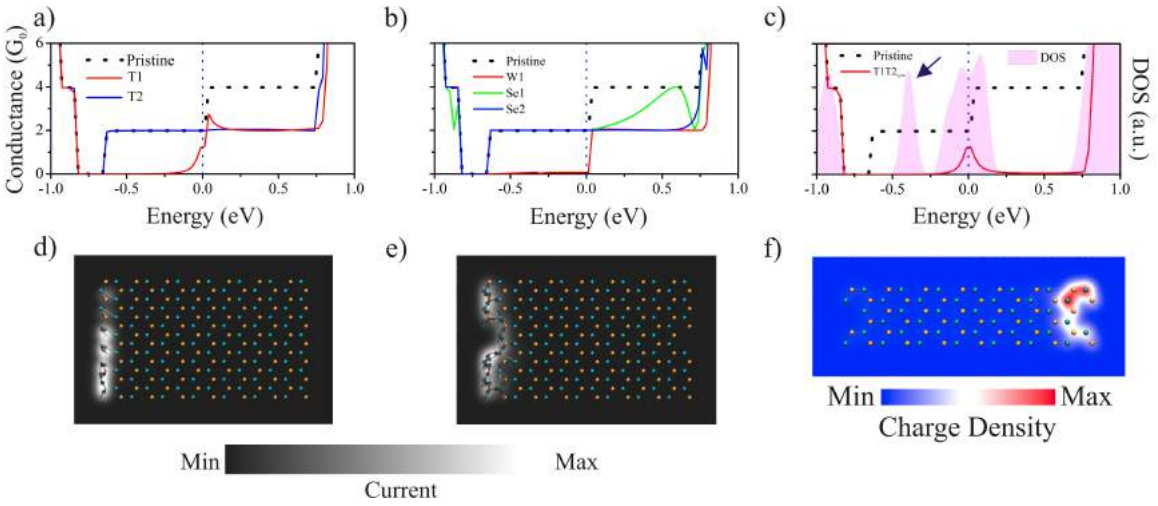

Figure 30: (a) Conductance curves for triplet defects in the metal edge of the ribbon (T1-red line) and in the chalcogen edge (T2-blue line). (b) Conductance curves for the vacancy of a single W atom at the metal edge and the single vacancy and di-vacancy of Se atoms in the chalcogen edge are considered, these defects are labeled as W1, Se1 and Se2 in this same order.(c) Conductance curves for a system with the T1 and T2 defects symmetrically combined ($T1T2_{sym}$). In (a), (b) and (c) the quantum conductance for pristine 14z-WSe_2NR is shown as a black dotted line, for comparison. (d) show the local current for the pristine conductance (black doted line) for -0.50 V. (e) The local current for the combined system in the range between -2mV and 2mV. (f) show the charge density associated to the DOS peak pointed by the blue arrow in (c).

It can be seen that for this type of defect the conductance plateau in the energy range between -0.50 and 0.0 eV has been completely suppressed, while for the 0.0 to 0.5 eV range, the conductance decreased to $2G_0$, except for the presence of a conductance peak at 0.04 eV with maximum conductance of $3G_0$. This result is analogous to the one observed for the MoS_2 case and corresponds to the suppression of the conductance along the metal-terminated edge due to the presence of the triplet-defect, with the presence of a resonant peak. These results suggest the possibility of employing such defective structure as a tunnelling diode, on which a small gate voltage can be employed to turn the conductivity on and off. Recent results on MoS_2NRs suggest similar applications for these types of systems [141]. On the other hand, the removal of a WSe_2 triplet from the chalcogen-terminated edge of the ribbon (T2) only changes the conductance in the interval from 0.0 to 0.5 eV, leaving a single plateau between -0.5 and 0.5 eV (blue line in Fig 30 a). This result can be understood from the perspective that the presence of a triplet-defect on the chalcogen-terminated edge completely suppresses the current along that edge.

We also analyse the effects of defects consisting of the removal of a single atom from one of the edges of the WSe_2 nanoribbon, as was done for the MoS_2 system. In Figure 30 b), we show the conductance curves for a system where a single W (red line) atom was removed from the metal-terminated edge, together with the conductance curves

for systems on which either one (Se1 - green line) or two (Se2 - blue line) Selenium atoms are removed from the chalcogen terminated edge. The subtraction of a W atom leads to a similar result as in T1 case but without the presence of the resonant conductance peak near the Fermi level, similar to what was observed for the MoS_2 system. As also observed above, the presence of defects at the chalcogen-terminated edge only affects the conductance for positive energy values near E_f. In the case of a single Se vacancy, the conductance curve shows a smooth decrease from $4G_0$ to $2G_0$ while for the case when both Se atoms are removed the result is similar to that of the T2 defect: a partial suppression of the conductance for energies between 0 and 0.5 eV.

Finally, we consider the case of a combination of the T1 and T2 defects on the WSe_2 nanoribbons. The conductance for this set-up is depicted in Figure 30 c) together with the calculated DOS (shaded area) for these systems. The conductance for energies close to the Fermi level is characterized by a sharp peak at E_f, similar to that of MoS_2 case. The local current density for the energy range between -2 and 2 meV is plotted in Figure 30 e), which clearly shows that the transmission channel is localized only in the metal-terminated edge of the system. It interesting to note that although the DOS shows several peaks near the Fermi energy, not all of these states contribute to the nanoribbon conductance. For instance, in Fig. 30 f) we show that the charge density associated the DOS peak at -0.4 eV (blue arrow in Fig. 30 c) is localized at the chalcogen-terminated edge of the system. Since all the contribution to the conductance seem to be coming from the metal-terminated edge, we can conclude that these localized states do not contribute on the conductance of this system.

In order to improve the analysis of triplet vacancies on z-WSe_2NRs, we turn now to the effects of double vacancies on the edges of the ribbon. In Figure 31 a) the quantum conductance for the system where only one triplet vacancy is inserted (T1) is compared to the systems in which a second WSe_2 triplet is removed from the metal-terminated edge of the ribbon N unit-cells away from the first defect (T1T1). What we observe is that the quantum conductance does not change significantly. The main change observed when the second defect is added is in the resonant conduction peaks. For the T1 system a single resonance peak is observed near the Fermi energy while for the T1T1 system, three resonance peaks are observed, one slightly below the Fermi energy, one slightly above and a third one near 0.7 eV. The position and intensity of these conductance peaks is extremely sensitive to the distance between the two defects (not shown here). The geometry for this case may be seen in Figure 32. In Fig. 31 b) we show the conductance for a system on which the two defects are introduced on the chalcogen-terminated edge (T2T2). WSe_2 triplets are taken off from the chalcogen edge of the ribbon (T2B). It

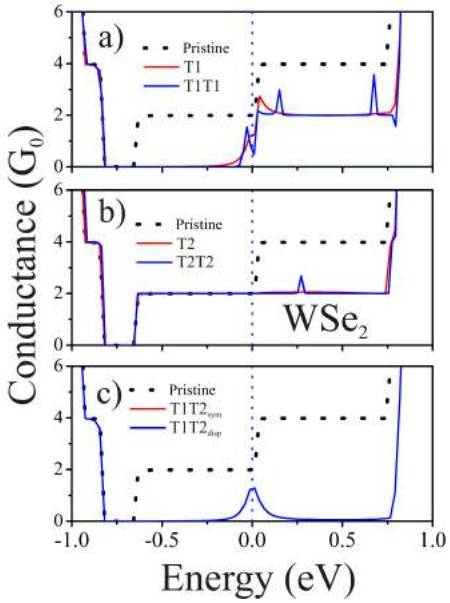

Figure 31: a) Quantum conductance for a single triplet defect at the metal edge (T1) of the z-WSe_2NR compared to a double triplet defective edge (T1B). b) Quantum conductance for a single triplet defect at the chalcogen edge (T2) of the z-WSe_2NR compared to a double triplet defective edge (T2B). c) Conductance for two symmetric triplet vacancies at the edges of z-WSe_2NR ($T1T2_{sym}$) and for the non-symmetric lack of the same triplets ($T1T2_{disp}$), the conductance curves are identical.

can be seen that the change in conductance due to the addition of another T2 defect is minimal, consisting of the appearance of a small conductance peak at 0.26 eV. Finally in c), a single WSe_2 triplet is removed from each edge of the ribbon. Here, we consider two cases, in the first case ($T1T2_{sym}$), the defects are symmetrically opposite (red line), while in the second ($T1T2_{disp}$), case the defects are displaced from each other by 4 unit cells in the translational direction of the ribbon (see figure S4). Both cases show the exact same conductance spectrum, characterized by a single resonance peak at the Fermi energy, as observed before. Similar results are also observed for the MoS_2 systems, indicating that the presence of a single triplet defect on either of the edges is sufficient to completely suppress the conductance along that edge, such that the introduction of other defects along the same edge cause only small deviations in the conductance properties of the system.

4.2.1 MoS2 Nanoribbons

We now study the effects of a simple defect at the edges of a 14z-MoS_2NR. This simple defect consists of removing a single MoS_2 triplet from the edge of the nanoribbon, in a given region of the ribbon's edge. Other types of defects, such as a single S vacancy, are also possible and will be the subject of further studies. As seen in Fig. 33, the vacancies are inserted in several positions along the borders of the ribbon. Fig. 33

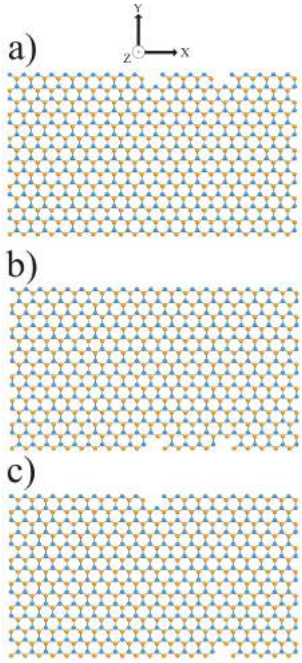

Figure 32: a) Two WSe_2 triplets taken off from the metal edge of the ribbon (T1T1 defect), b) shows the lack of two triplets in the chalcogen edge of the ribbon (T2T2 defect), c) Depicts the T1T2 defects combined, and the position of the defects is displaced ($T1T2_{disp}$ defect).

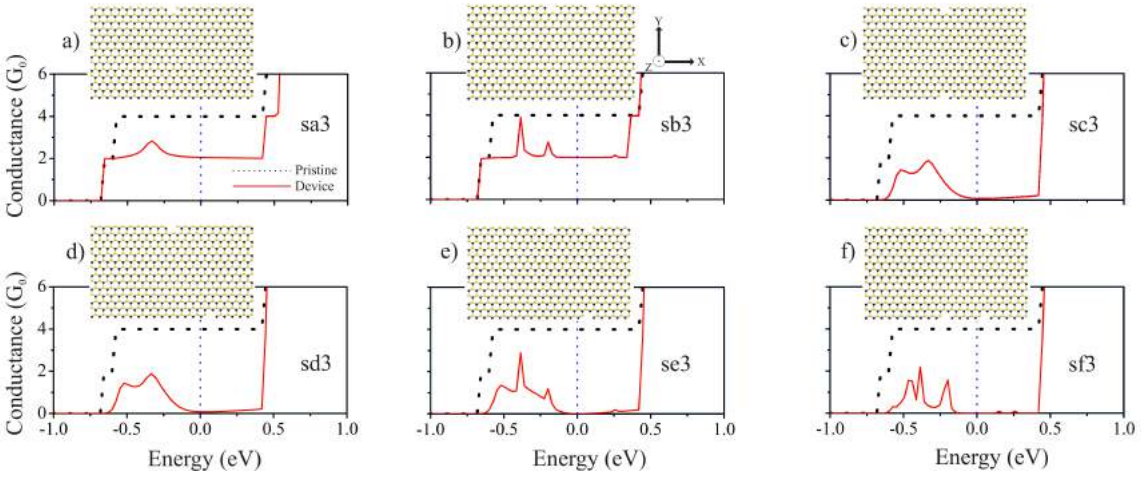

Figure 33: Quantum conductance (red line) for simple defects inserted on the edges of a 14z-MoS_2NR. Those defects consists of a simple vacancy of a MoS_2 triplet, as indicated in the geometry representation, above the conductance graphs. The black dotted line represents the quantum conductance of a pristine 14z-MoS_2NR.

a) shows the geometry of a device with a single vacancy on one of the edges and its corresponding quantum conductance plot. For comparison we also show as black dotted lines the quantum conductance of the pristine nanoribbon system. What we see is that the presence of a single defect is enough to strongly affect the conductance of the system when it is compared to the pristine nanoribbon case. It can be seen that for the red curve the quantum conductance near the Fermi energy has decreased to about a half of

its original value. This result indicates that the quantum transport for such ribbons is strongly dependent on the device's edge integrity. In panel b) two similar defects are inserted in the same edge. The second defect is placed at a distance of 5 unit cells from the first one, corresponding to a separation of approximately 15 Å . This defect led to a higher conductance peak at around -0.25 eV which is of about $4G_0$, and a smaller peak at around 0.25 eV. However, except for the presence of these two features, the quantum conductance in this case is very similar to that observed for the system with a single edge vacancy, shown in Fig. 33 a).

Figures 33 c) and d), show the conductance of the system when the second defect is placed on the opposite edge. We study two cases with strikingly similar results: in Fig. 33 c) we focus on the case when the second defect is exactly opposite the first one, while in d) we show the case on which the defect is displaced by 15 Å in one of the directions. Both configurations show a conductance decrease when compared to both the pristine system and the system with two defects on the same edge. For both cases, we observe two broad peaks on the conductance curve that have maximums for energies immediately bellow the Fermi level. Figures. 33 e) and f) show the results for the case of having three and four defects, located in both edges. In e) the conductance curve in the range -0.5 to 0.5 eV features a strong peak at around -0.25 eV with a conductance of about $3G_0$. The results in Fig. 33 can be summarized on the following way: The presence of a single defect in either of the edges is enough to suppress a large part of the conductance on that edge, leaving only the contribution from electronic states near the Fermi level. Each edge seems to be acting independently. The presence of other defects on the same edge lead to interference effects which suppress the conductance for some energy ranges and enhances it for specific values of energy, leading to the appearance of sharp conductance peaks. The intensity and position of these peaks depend on the exact geometrical configuration of the defects.

4.3 Conclusions of This Chapter

In summary we have studied the electronic transport properties of nanometric molybdenum disulphide and tungsten diselenide zigzag ribbons by using a density functional based tight-binding (DFTB) approach. Our results indicated that the quantum transport in z-MoS_2 and z-WSe_2 nanoribbons is strongly edge dependent. Simple defects in one of the edges, like the vacancy of a MoS_2/WSe_2 triplet, leads to a significant decrease in the quantum conductance of the system. Moreover, the removal of a single Mo or Se atom in the metal-terminated edge results in a very similar behavior as that obtained for the removal of the whole MoS_2 or WSe_2 triplet from the same edge. Simi-

larly, the removal of one the chalcogen atoms in the chalcogen-terminated edge leads to a drop in the conductance along that edge and the removal of both chalcogen atoms leads to results similar to those obtained with the removal of a TMDC triplet from that edge. Also, two similar defects added in the same side, didn't change the quantum conductance of the system in relation to the one containing only one triplet lack. We also observed that defects in both sides of the ribbon, strongly affected the quantum conductance of the system, which showed conductance peaks located at different energy values. This suggests that such defective ribbons can be applied as tunneling diodes. The rectifying properties of MoS_2 based systems have been proposed in the literature very recently [141]. In this sense, our calculations, associated to the newly developed etching techniques, suggest the applicability of MoS_2/WSe_2 nanoribbons as an active agent on electronic devices.

CONCLUSIONS AND PERSPECTIVES

In summary our work showed that graphene/boron nitride hetero-junctions are plenty for spintronics explorations, due to the high spin resistance in the C/BN interface. Moreover doping the BN domains with carbon atoms enhances the spin polarization, since localized charges are found nearby the dopant, which create regions for selective scattering. Also, spin polarization may be induced in armchair edged systems by carbon doping. Furthermore, we have showed that doped BNC systems may be employed as high sensitive molecular sensors, as well as spin dependent sensors. Besides, these devices might have it switching controlled by adsorbents. We also emphasize the fact the the SIESTA method is reliable for studding the spin behaviour in hybrid BNC system, specially for the treatment of large supercells.

On the other hand, the study of electronic transport for TMDCs nanoribbons has revealed the strong dependence on the edge morphology for the electronic transport. Our local current plots shows that even for a defective edge the electrons flows though the edges. We also conclude that the geometry of the defect is not determinant for the suppression of the quantum conductance. Even a simple vacancy of an atomic triplet has the same effect of multiple sequential vacancies. The atomic layers which compose the entire TMDC structure, also plays an important role in the electronic transport picture. It is because the quantum conductance is strongly associate with these layers. The set of Slater-Koster parameters proposed by Zahid *et al* [133] describes sufficiently well the physical properties of these ribbons.

The study of the effects of adsorption of different molecular systems over the doped boron nitride cluster is left as a perspective for future investigations.

Also, different arrangements of the dopants over the BN cluster is a perspective for the future, as well as the study of BN island of different sizes positioned between graphene nanoribbons.

New molecular dynamics calculations are also left for future studies, in order to verify the melting temperature of those doped systems.

For the tight binding study on TMDCs, the analysis of effects due to single atomic vacancies is left as a perspective to this project.

Also, the study of other species, such as $MoSe2$, $WS2$ and $WSe2$ beyond the $MoS2$ case is left for the future.

The fitting of new Salter-Koster parameters for hybrid systems involving $MoSe2$, $WS2$, $WSe2$ and $MoS2$ is our next goal in this area.

The parametrization for TMDCs system hybridized with graphene systems is also a step left for the future, as well as the study of optoelectronics in such devices.

Finally, studies on hybrid one dimensional BNC systems are being carried out, at this time, and they also are left as perspectives related to this thesis.

APPENDIX A – THE SLATER-KOSTER INTEGRALS

$$\langle s|s\rangle = ss\sigma$$

$$\langle p_x|p_x\rangle = l^2pp\sigma + (1-l^2)pp\pi$$

$$\langle p_y|p_y\rangle = m^2pp\sigma + (1-m^2)pp\pi$$

$$\langle p_z|p_z\rangle = n^2pp\sigma + (1-n^2)pp\pi$$

$$\langle 3z^2-r^2|3z^2-r^2\rangle = \left[n^2 - \frac{1}{2}(l^2+m^2)\right]^2 dd\sigma + 3n^2(l^2+m^2)dd\pi + \frac{3}{4}(l^2+m^2)^2dd\delta$$

$$\langle xz|xz\rangle = 3l^2n^2dd\sigma + (l^2+n^2-4l^2n^2)dd\pi + (m^2+l^2n^2)dd\delta$$

$$\langle yz|yz\rangle = 3m^2n^2dd\sigma + (m^2+n^2-4m^2n^2)dd\pi + (l^2+m^2n^2)dd\delta$$

$$\langle xy|xy\rangle = 3l^2m^2dd\sigma + (l^2+m^2-4l^2m^2)dd\pi + (n^2+l^2m^2)dd\delta$$

$$\langle x^2-y^2|x^2-y^2\rangle = \frac{3}{4}(l^2-m^2)^2dd\sigma + [l^2+m^2-(l^2-m^2)^2]dd\pi + \left[n^2+\frac{1}{4}(l^2-m^2)^2\right]dd\delta$$

$$\langle s|p_x\rangle = lsp\sigma$$

$$\langle p_x|s\rangle = -\langle s|p_x\rangle$$

$$\langle s|p_y\rangle = msp\sigma$$

$$\langle p_y|s\rangle = -\langle s|p_y\rangle$$

$$\langle s|p_z\rangle = nsp\sigma$$

$$\langle p_z|s\rangle = -\langle s|p_z\rangle$$

$$\langle s|3z^2 - r^2\rangle = \left[n^2 - \frac{1}{2}(l^2 + m^2)\right] sd\sigma$$

$$\langle 3z^2 - r^2|s\rangle = \langle s|3z^2 - r^2\rangle$$

$$\langle s|xz\rangle = \sqrt{3}lnsd\sigma$$

$$\langle xz|s\rangle = \langle s|xz\rangle$$

$$\langle s|yz\rangle = \sqrt{3}mnsd\sigma$$

$$\langle yz|s\rangle = \langle s|yz\rangle$$

$$\langle s|xy\rangle = \sqrt{3}lmsd\sigma$$

$$\langle xy|s\rangle = \langle s|xy\rangle$$

$$\langle s|x^2 - y^2\rangle = \frac{\sqrt{3}}{2}(l^2 - m^2)sd\sigma$$

$$\langle x^2 - y^2|s\rangle = \langle s|x^2 - y^2\rangle$$

$$\langle p_x|p_y\rangle = lmpp\sigma - lmpp\pi$$

$$\langle p_y|p_x\rangle = \langle p_x|p_y\rangle$$

$$\langle p_x|p_z\rangle = lnpp\sigma - lnpp\pi$$

$$\langle p_z|p_x\rangle = \langle p_x|p_z\rangle$$

$$\langle p_x|3z^2 - r^2\rangle = l\left[n^2 - \frac{1}{2}(l^2 + m^2)\right] pd\sigma - \sqrt{3}ln^2pd\pi$$

$$\langle 3z^2 - r^2|p_x\rangle = -\langle p_x|3z^2 - r^2\rangle$$

$$\langle p_x|xz\rangle = \sqrt{3}l^2npd\sigma + n(1-2l^2)pd\pi$$

$$\langle xz|p_x\rangle = -\langle p_x|xz\rangle$$

$$\langle p_x|yz\rangle = \sqrt{3}lmnpd\sigma - 2lmnpd\pi$$

$$\langle yz|p_x\rangle = -\langle p_x|yz\rangle$$

$$\langle p_x|xy\rangle = \sqrt{3}l^2mpd\sigma + m(1-2l^2)pd\pi$$

$$\langle xy|p_y\rangle = -\langle p_x|xy\rangle$$

$$\langle p_x|x^2-y^2\rangle = \frac{\sqrt{3}}{2}l(l^2-m^2)pd\sigma + l(1-l^2+m^2)pd\pi$$

$$\langle x^2-y^2|p_x\rangle = -\langle p_x|x^2-y^2\rangle$$

$$\langle p_y|p_z\rangle = mnpp\sigma - mnpp\pi$$

$$\langle p_z|p_y\rangle = \langle p_y|p_z\rangle$$

$$\langle p_y|3z^2-r^2\rangle = m\left[n^2 - \frac{1}{2}(l^2+m^2)\right]pd\sigma - \sqrt{3}mn^2pd\pi$$

$$\langle 3z^2-r^2|p_y\rangle = -\langle p_y|3z^2-r^2\rangle$$

$$\langle p_y|xz\rangle = \sqrt{3}lmnpd\sigma - 2lmnpd\pi$$

$$\langle xz|p_y\rangle = -\langle p_y|xz\rangle$$

$$\langle p_y|yz\rangle = \sqrt{3}m^2npd\sigma + n(1-2m^2)pd\pi$$

$$\langle yz|p_y\rangle = -\langle p_y|yz\rangle$$

$$\langle p_y|xy\rangle = \sqrt{3}lm^2pd\sigma + l(1-2m^2)pd\pi$$

$$\langle xy|p_y\rangle = -\langle p_y|xy\rangle$$

$$\langle p_y|x^2-y^2\rangle = \frac{\sqrt{3}}{2}m(l^2-m^2)pd\sigma - m(1+l^2-m^2)pd\pi$$

$$\langle x^2-y^2|p_y\rangle = -\langle p_y|x^2-y^2\rangle$$

$$\langle p_z|3z^2-r^2\rangle = n\left[n^2-\frac{1}{2}(l^2+m^2)\right]pd\sigma + \sqrt{3}n(l^2+m^2)pd\pi$$

$$\langle 3z^2-r^2|p_z\rangle = -\langle p_z|3z^2-r^2\rangle$$

$$\langle p_z|xz\rangle = \sqrt{3}n^2lpd\sigma + l(1-2n^2)pd\pi$$

$$\langle xz|p_z\rangle = -\langle p_z|xz\rangle$$

$$\langle p_z|yz\rangle = \sqrt{3}n^2mpd\sigma + m(1-2n^2)pd\pi$$

$$\langle yz|p_z\rangle = -\langle p_z|yz\rangle$$

$$\langle p_z|xy\rangle = \sqrt{3}lmnpd\sigma - 2lmnpd\pi$$

$$\langle xy|p_z\rangle = -\langle p_z|xy\rangle$$

$$\langle p_z|x^2-y^2\rangle = \frac{\sqrt{3}}{2}n(l^2-m^2)pd\sigma - n(l^2-m^2)pd\pi$$

$$\langle 3z^2-r^2|xz\rangle = \sqrt{3}ln\left[n^2-\frac{1}{2}(l^2+m^2)\right]dd\sigma+\sqrt{3}ln(l^2+m^2-n^2)dd\pi-\frac{\sqrt{3}}{2}ln(l^2+m^2)dd\delta$$

$$\langle xz|3z^2-r^2\rangle = \langle 3z^2-r^2|xz\rangle$$

$$\langle 3z^2-r^2|yz\rangle = \sqrt{3}mn\left[n^2-\frac{1}{2}(l^2+m^2)\right]dd\sigma+\sqrt{3}mn(l^2+m^2-n^2)dd\pi-\frac{\sqrt{3}}{2}mn(l^2+m^2)dd\delta$$

$$\langle yz|3z^2-r^2\rangle = \langle 3z^2-r^2|yz\rangle$$

$$\langle 3z^2 - r^2|xy\rangle = \sqrt{3}lm\left[n^2 - \frac{1}{2}(l^2+m^2)\right]dd\sigma - 2\sqrt{3}lmn^2dd\pi + \frac{\sqrt{3}}{2}lm(1+n^2)dd\delta$$

$$\langle xy|3z^2 - r^2\rangle = \langle 3z^2 - r^2|xy\rangle$$

$$\langle x^2 - y^2|p_z\rangle = -\langle p_z|x^2 - y^2\rangle$$

$$\langle 3z^2 - r^2|x^2 - y^2\rangle = \frac{\sqrt{3}}{2}(l^2-m^2)\left[n^2-\frac{1}{2}(l^2+m^2)\right]dd\sigma+\sqrt{3}n^2(m^2-l^2)dd\pi+\frac{\sqrt{3}}{4}(1+n^2)(l^2-m^2)dd\delta$$

$$\langle x^2 - y^2|3z^2 - r^2\rangle = \langle 3z^2 - r^2|x^2 - y^2\rangle$$

$$\langle xz|yz\rangle = 3lmn^2dd\sigma + lm(1-4n^2)dd\pi + ml(n^2-1)dd\delta$$

$$\langle yz|xz\rangle = \langle xz|yz\rangle$$

$$\langle xz|xy\rangle = 3l^2mnddd\sigma + mn(1-4l^2)dd\pi + mn(l^2-1)dd\delta$$

$$\langle xy|xz\rangle = \langle xz|xy\rangle$$

$$\langle xz|x^2 - y^2\rangle = \frac{3}{2}nl(l^2-m^2)dd\sigma + nl[1-2(l^2-m^2)]dd\pi - nl\left[1-\frac{1}{2}(l^2-m^2)\right]dd\delta$$

$$\langle x^2 - y^2|xz\rangle = \langle xz|x^2 - y^2\rangle$$

$$\langle yz|xy\rangle = 3lm^2ndd\sigma + ln(1-4m^2)dd\pi + ln(m^2-1)dd\delta$$

$$\langle xy|yz\rangle = \langle yz|xy\rangle$$

$$\langle yz|x^2 - y^2\rangle = \frac{3}{2}mn(l^2-m^2)dd\sigma - mn[1+2(l^2-m^2)]dd\pi + mn\left[1+\frac{1}{2}(l^2-m^2)\right]dd\delta$$

$$\langle x^2 - y^2|yz\rangle = \langle yz|x^2 - y^2\rangle$$

$$\langle xy|x^2 - y^2\rangle = \frac{3}{2}lm(l^2-m^2)dd\sigma + 2lm(m^2-l^2)dd\pi + \frac{1}{2}lm(l^2-m^2)dd\delta$$

$$\langle x^2 - y^2 | xy \rangle = \langle xy | x^2 - y^2 \rangle$$

REFERENCES

[1] Sumio Iijima. Helical microtubules of graphitic carbon. *Nature*, 354(6348):56–58, November 1991.

[2] Jinming Cai, Pascal Ruffieux, Rached Jaafar, Marco Bieri, Thomas Braun, Stephan Blankenburg, Matthias Muoth, Ari P. Seitsonen, Moussa Saleh, Xinliang Feng, Klaus Mullen, and Roman Fasel. Atomically precise bottom-up fabrication of graphene nanoribbons. *Nature*, 466(7305):470–473, July 2010.

[3] Kenji Watanabe, Takashi Taniguchi, and Hisao Kanda. Direct-bandgap properties and evidence for ultraviolet lasing of hexagonal boron nitride single crystal. *Nature Materials*, 3(6):404–409, May 2004.

[4] H. W. Kroto, J. R. Heath, S. C. O'Brien, R. F. Curl, and R. E. Smalley. C60: Buckminsterfullerene. *Nature*, 318(6042):162–163, November 1985.

[5] Alberto Bianco, Kostas Kostarelos, Charalambos D. Partidos, and Maurizio Prato. Biomedical applications of functionalised carbon nanotubes. *Chemical Communications*, (5):571, 2005.

[6] Sander J. Tans, Alwin R. M. Verschueren, and Cees Dekker. Room-temperature transistor based on a single carbon nanotube. *Nature*, 393(6680):49–52, May 1998.

[7] Mark Johnson and R. H. Silsbee. Interfacial charge-spin coupling: Injection and detection of spin magnetization in metals. *Phys. Rev. Lett.*, 55:1790–1793, Oct 1985.

[8] K. S. Novoselov, A. K. Geim, S. V. Morozov, D. Jiang, Y. Zhang, S. V. Dubonos, I. V. Grigorieva, and A. A. Firsov. Electric field effect in atomically thin carbon films. *Science*, 306(5696):666–669, October 2004.

[9] M. S. Dresselhaus R. Saito, G. Dresselhaus. Physical properties of carbon nanotubes. *Imperial College Press*, 1998.

[10] S. Canuto J. D. M. Vianna, A. Fazzio. Teoria quântica de moléculas e sólidos. *Livraria da Física*, 2004.

[11] A. K. Geim and K. S. Novoselov. The rise of graphene. *Nat Mater*, 6(3):183–191, March 2007.

[12] Yuanbo Zhang, Yan-Wen Tan, Horst L. Stormer, and Philip Kim. Experimental observation of the quantum Hall effect and Berry's phase in graphene. *Nature*, 438(7065):201–204, November 2005.

[13] K. S. Novoselov, Z. Jiang, Y. Zhang, S. V. Morozov, H. L. Stormer, U. Zeitler, J. C. Maan, G. S. Boebinger, P. Kim, and A. K. Geim. Room-Temperature Quantum Hall Effect in Graphene. *Science*, 315(5817):1379–1379, March 2007.

[14] Claire Berger, Zhimin Song, Xuebin Li, Xiaosong Wu, Nate Brown, Cécile Naud, Didier Mayou, Tianbo Li, Joanna Hass, Alexei N. Marchenkov, and others. Electronic confinement and coherence in patterned epitaxial graphene. *Science*, 312(5777):1191–1196, 2006.

[15] I. W. Frank, D. M. Tanenbaum, A. M. van der Zande, and P. L. McEuen. Mechanical properties of suspended graphene sheets. *Journal of Vacuum Science & Technology B: Microelectronics and Nanometer Structures*, 25(6):2558, 2007.

[16] A. King, G. Johnson, D. Engelberg, W. Ludwig, and J. Marrow. Observations of Intergranular Stress Corrosion Cracking in a Grain-Mapped Polycrystal. *Science*, 321(5887):382–385, July 2008.

[17] Alexander A. Balandin, Suchismita Ghosh, Wenzhong Bao, Irene Calizo, Desalegne Teweldebrhan, Feng Miao, and Chun Ning Lau. Superior Thermal Conductivity of Single-Layer Graphene. *Nano Letters*, 8(3):902–907, March 2008.

[18] Keun Soo Kim, Yue Zhao, Houk Jang, Sang Yoon Lee, Jong Min Kim, Kwang S. Kim, Jong-Hyun Ahn, Philip Kim, Jae-Young Choi, and Byung Hee Hong. Large-scale pattern growth of graphene films for stretchable transparent electrodes. *Nature*, 457(7230):706–710, February 2009.

[19] Katsunori Wakabayashi. Electronic transport properties of nanographite ribbon junctions. *Phys. Rev. B*, 64:125428, Sep 2001.

[20] Verónica Barone, Oded Hod, and Gustavo E. Scuseria. Electronic Structure and Stability of Semiconducting Graphene Nanoribbons. *Nano Letters*, 6(12):2748–2754, December 2006.

[21] Melinda Y. Han, Barbaros Özyilmaz, Yuanbo Zhang, and Philip Kim. Energy band-gap engineering of graphene nanoribbons. *Phys. Rev. Lett.*, 98:206805, May 2007.

[22] S. Aigner, L. D. Pietra, Y. Japha, O. Entin-Wohlman, T. David, R. Salem, R. Folman, and J. Schmiedmayer. Long-Range Order in Electronic Transport Through Disordered Metal Films. *Science*, 319(5867):1226–1229, February 2008.

[23] Kyoko Nakada, Mitsutaka Fujita, Gene Dresselhaus, and Mildred S. Dresselhaus. Edge state in graphene ribbons: Nanometer size effect and edge shape dependence. *Phys. Rev. B*, 54:17954–17961, Dec 1996.

[24] W. Auwärter, T. J. Kreutz, T. Greber, and J. Osterwalder. XPD and STM investigation of hexagonal boron nitride on Ni (111). *Surface science*, 429(1):229–236, 1999.

[25] Martin ENGLER, Christoph LESNIAK, Ralf DAMASCH, Bernd RUISINGER, and Jens EICHLER. Hexagonal boron nitride (hbn) : Applications from metallurgy to cosmetics. *Göller, Baden-Baden, ALLEMAGNE (1980) (Revue)*, 84(12), 2007.

[26] T. Greber. Handbook of nanophysics: Functional nanomaterials. *CRC Press*, 5, 2010.

[27] Hugh O. Pierson. Boron nitride composites by chemical vapor deposition. *Journal of Composite Materials*, 9(3):228–240, July 1975.

[28] M.T. Paffett, R.J. Simonson, P. Papin, and R.T. Paine. Borazine adsorption and decomposition at pt(111) and ru(001) surfaces. *Surface Science*, 232(3):286 – 296, 1990.

[29] S Azevedo and R. de Paiva. Structural stability and electronic properties of carbon-boron nitride compounds. *Europhysics Letters (EPL)*, 75(1):126–132, July 2006.

[30] M. Modarresi, M.R. Roknabadi, and N. Shahtahmasbi. Transport properties of an armchair boron-nitride nanoribbon embedded between two graphene electrodes. *Physica E: Low-dimensional Systems and Nanostructures*, 43(9):1751 – 1754, 2011.

[31] Shen-Lin Chang, Bi-Ru Wu, Po-Hua Yang, and Ming-Fa Lin. Curvature effects on electronic properties of armchair graphene nanoribbons without passivation. *Physical Chemistry Chemical Physics*, 14(47):16409, 2012.

[32] Ruiqi Zhao, Jinying Wang, Mingmei Yang, Zhongfan Liu, and Zhirong Liu. Graphenequantum dots embedded in a hexagonal BN sheet: identical influences of zigzag/armchair edges. *Phys. Chem. Chem. Phys.*, 15(3):803–806, 2013.

[33] Manish Chhowalla, Hyeon Suk Shin, Goki Eda, Lain-Jong Li, Kian Ping Loh, and Hua Zhang. The chemistry of two-dimensional layered transition metal dichalcogenide nanosheets. *Nature Chemistry*, 5(4):263–275, March 2013.

[34] A. Kuc, N. Zibouche, and T. Heine. Influence of quantum confinement on the electronic structure of the transition metal sulfide T S 2. *Physical Review B*, 83(24), June 2011.

[35] Andrea Splendiani, Liang Sun, Yuanbo Zhang, Tianshu Li, Jonghwan Kim, Chi-Yung Chim, Giulia Galli, and Feng Wang. Emerging Photoluminescence in Monolayer MoS $_2$. *Nano Letters*, 10(4):1271–1275, April 2010.

[36] Yuqiang Ma, Bilu Liu, Anyi Zhang, Liang Chen, Mohammad Fathi, Chenfei Shen, Ahmad N. Abbas, Mingyuan Ge, Matthew Mecklenburg, and Chongwu Zhou. Reversible Semiconducting-to-Metallic Phase Transition in Chemical Vapor Deposition Grown Monolayer WSe $_2$ and Applications for Devices. *ACS Nano*, 9(7):7383–7391, July 2015.

[37] Hsun-Jen Chuang, Xuebin Tan, Nirmal Jeevi Ghimire, Meeghage Madusanka Perera, Bhim Chamlagain, Mark Ming-Cheng Cheng, Jiaqiang Yan, David Mandrus, David Tománek, and Zhixian Zhou. High Mobility WSe $_2$ p - and n - Type Field-Effect Transistors Contacted by Highly Doped Graphene for Low-Resistance Contacts. *Nano Letters*, 14(6):3594–3601, June 2014.

[38] Rajesh Kappera, Damien Voiry, Sibel Ebru Yalcin, Brittany Branch, Gautam Gupta, Aditya D. Mohite, and Manish Chhowalla. Phase-engineered low-resistance contacts for ultrathin MoS2 transistors. *Nat Mater*, 13(12):1128–1134, December 2014.

[39] M. Born and R. Oppenheimer. Zur quantentheorie der molekeln. *Annalen der Physik*, 389(20):457–484, 1927.

[40] N. W. Ashcroft and N. D. Mermin. Física do estado sólido. *Cengage Learning*, 2011.

[41] A. Szabo and N. S. Ostlund. Modern quantum chemistry. *McGraw-Hill*, 1989.

[42] Koichiro Umemoto, Renata M. Wentzcovitch, and Philip B. Allen. Dissociation of MgSiO3 in the Cores of Gas Giants and Terrestrial Exoplanets. *Science*, 311(5763):983–986, February 2006.

[43] P. Hohenberg and W. Kohn. Inhomogeneous electron gas. *Phys. Rev.*, 136:B864–B871, Nov 1964.

[44] W. Kohn and L. J. Sham. Self-consistent equations including exchange and correlation effects. *Phys. Rev.*, 140:A1133–A1138, Nov 1965.

[45] L. H. Thomas. The calculation of atomic fields. *Mathematical Proceedings of the Cambridge Philosophical Society*, 23:542–548, 1 1927.

[46] R.G. Parr and W. Yang. Density-functional theory of atoms and molecules. *Oxford: Oxford University Press*, 1989.

[47] D. M. Ceperley and B. J. Alder. Ground state of the electron gas by a stochastic method. *Phys. Rev. Lett.*, 45:566–569, Aug 1980.

[48] J. P. Perdew and Alex Zunger. Self-interaction correction to density-functional approximations for many-electron systems. *Phys. Rev. B*, 23:5048–5079, May 1981.

[49] John P. Perdew, Kieron Burke, and Matthias Ernzerhof. Generalized gradient approximation made simple. *Phys. Rev. Lett.*, 77:3865–3868, Oct 1996.

[50] Chengteh Lee, Weitao Yang, and Robert G. Parr. Development of the colle-salvetti correlation-energy formula into a functional of the electron density. *Phys. Rev. B*, 37:785–789, Jan 1988.

[51] G. B. Bachelet, D. R. Hamann, and M. Schlüter. Pseudopotentials that work: From h to pu. *Phys. Rev. B*, 26:4199–4228, Oct 1982.

[52] Norman Troullier and José Luriaas Martins. Efficient pseudopotentials for plane-wave calculations. *Physical Review B*, 43(3):1993, 1991.

[53] D. R. Hamann, M. Schlüter, and C. Chiang. Norm-conserving pseudopotentials. *Phys. Rev. Lett.*, 43:1494–1497, Nov 1979.

[54] David Vanderbilt. Optimally smooth norm-conserving pseudopotentials. *Phys. Rev. B*, 32:8412–8415, Dec 1985.

[55] S. Goedecker and K. Maschke. Transferability of pseudopotentials. *Phys. Rev. A*, 45:88–93, Jan 1992.

[56] Leonard Kleinman and D. M. Bylander. Efficacious form for model pseudopotentials. *Phys. Rev. Lett.*, 48:1425–1428, May 1982.

[57] Eduardo Anglada, José M. Soler, Javier Junquera, and Emilio Artacho. Systematic generation of finite-range atomic basis sets for linear-scaling calculations. *Phys. Rev. B*, 66:205101, Nov 2002.

[58] Javier Junquera, Óscar Paz, Daniel Sánchez-Portal, and Emilio Artacho. Numerical atomic orbitals for linear-scaling calculations. *Phys. Rev. B*, 64:235111, Nov 2001.

[59] Pablo Ordejón, Emilio Artacho, and José M. Soler. Self-consistent order-n density-functional calculations for very large systems. *Phys. Rev. B*, 53:R10441–R10444, Apr 1996.

[60] Sigeru Huzinaga. Basis sets for molecular calculations. *Computer Physics Reports*, 2(6):281 – 339, 1985.

[61] José M. Soler, Emilio Artacho, Julian D. Gale, Alberto García, Javier Junquera, Pablo Ordejón, and Daniel Sánchez-Portal. The siesta method for ab initio order-n materials simulation. *Journal of Physics: Condensed Matter*, 14(11):2745, 2002.

[62] Felix Bloch. Über die quantenmechanik der elektronen in kristallgittern. *"Zeitschrift für Physik"*, 52(7):555–600, 1929.

[63] J. C. Slater and G. F. Koster. Simplified lcao method for the periodic potential problem. *Phys. Rev.*, 94:1498–1524, Jun 1954.

[64] R. Landauer. Spatial variation of currents and fields due to localized scatterers in metallic conduction. *IBM J. Res. Dev.*, 32(3):306–316, May 1988.

[65] Marco Buongiorno Nardelli. Electronic transport in extended systems: Application to carbon nanotubes. *Phys. Rev. B*, 60:7828–7833, Sep 1999.

[66] S. Datta. Electronic transport in mesoscopic systems. *Cambridge University Press, Cambridge*, July 1995.

[67] Ki Kang Kim, Allen Hsu, Xiaoting Jia, Soo Min Kim, Yumeng Shi, Mario Hofmann, Daniel Nezich, Joaquin F. Rodriguez-Nieva, Mildred Dresselhaus, Tomas Palacios, and Jing Kong. Synthesis of Monolayer Hexagonal Boron Nitride on Cu Foil Using Chemical Vapor Deposition. *Nano Letters*, 12(1):161–166, January 2012.

[68] Haibo Zeng, Chunyi Zhi, Zhuhua Zhang, Xianlong Wei, Xuebin Wang, Wanlin Guo, Yoshio Bando, and Dmitri Golberg. "White Graphenes": Boron Nitride Nanoribbons via Boron Nitride Nanotube Unwrapping. *Nano Letters*, 10(12):5049–5055, December 2010.

[69] Kin Fai Mak, Changgu Lee, James Hone, Jie Shan, and Tony F. Heinz. Atomically thin mos_2: A new direct-gap semiconductor. *Phys. Rev. Lett.*, 105:136805, Sep 2010.

[70] H. S. S. Ramakrishna Matte, A. Gomathi, Arun K. Manna, Dattatray J. Late, Ranjan Datta, Swapan K. Pati, and C. N. R. Rao. MoS2 and WS2 Analogues of Graphene. *Angewandte Chemie International Edition*, 49(24):4059–4062, June 2010.

[71] Boubekeur Lalmi, Hamid Oughaddou, Hanna Enriquez, Abdelkader Kara, Sébastien Vizzini, Bénidicte Ealet, and Bernard Aufray. Epitaxial growth of a silicene sheet. *Applied Physics Letters*, 97(22):223109, 2010.

[72] Jack R. Brent, Nicky Savjani, Edward A. Lewis, Sarah J. Haigh, David J. Lewis, and Paul O'Brien. Production of few-layer phosphorene by liquid exfoliation of black phosphorus. *Chem. Commun.*, 50(87):13338–13341, September 2014.

[73] Likai Li, Yijun Yu, Guo Jun Ye, Qingqin Ge, Xuedong Ou, Hua Wu, Donglai Feng, Xian Hui Chen, and Yuanbo Zhang. Black phosphorus field-effect transistors. *Nat Nano*, 9(5):372–377, May 2014.

[74] Feng-feng Zhu, Wei-jiong Chen, Yong Xu, Chun-lei Gao, Dan-dan Guan, Can-hua Liu, Dong Qian, Shou-Cheng Zhang, and Jin-feng Jia. Epitaxial growth of two-dimensional stanene. *Nat Mater*, advance online publication, August 2015.

[75] Marco Bernardi, Maurizia Palummo, and Jeffrey C. Grossman. Optoelectronic properties in monolayers of hybridized graphene and hexagonal boron nitride. *Phys. Rev. Lett.*, 108:226805, Jun 2012.

[76] Roland Yingjie Tay, Mark H. Griep, Govind Mallick, Siu Hon Tsang, Ram Sevak Singh, Travis Tumlin, Edwin Hang Tong Teo, and Shashi P. Karna. Growth of large single-crystalline two-dimensional boron nitride hexagons on electropolished copper. *Nano Letters*, 14(2):839–846, February 2014.

[77] Lijie Ci, Li Song, Chuanhong Jin, Deep Jariwala, Dangxin Wu, Yongjie Li, Anchal Srivastava, Z. F. Wang, Kevin Storr, Luis Balicas, Feng Liu, and Pulickel M. Ajayan. Atomic layers of hybridized boron nitride and graphene domains. *Nature Materials*, 9(5):430–435, May 2010.

[78] Gang Hee Han, Julio A. Rodrígues-Manzo, Chan-Woo Lee, Nicholas J. Kybert, Mitchell B. Lerner, Zhengqing John Qi, Eric N. Dattoli, Andrew M. Rappe, Marija Drndic, and A. T. Charlie Johnson. Continuous growth of hexagonal graphene and boron nitride in-plane heterostructures by atmospheric pressure chemical vapor deposition. *ACS Nano*, 7(11):10129–10138, November 2013.

[79] Zheng Liu, Lulu Ma, Gang Shi, Wu Zhou, Yongji Gong, Sidong Lei, Xuebei Yang, Jiangnan Zhang, Jingjiang Yu, Ken P. Hackenberg, Aydin Babakhani, Juan-Carlos Idrobo, Robert Vajtai, Jun Lou, and Pulickel M. Ajayan. In-plane heterostructures of graphene and hexagonal boron nitride with controlled domain sizes. *Nature Nanotechnology*, 8(2):119–124, January 2013.

[80] Robert W Keyes. Physical limits of silicon transistors and circuits. *Reports on Progress in Physics*, 68(12):2701–2746, December 2005.

[81] Frank Schwierz. Graphene transistors. *Nature Nanotechnology*, 5(7):487–496, July 2010.

[82] Arieh Aviram and Mark A. Ratner. Molecular rectifiers. *Chemical Physics Letters*, 29(2):277–283, 1974.

[83] B. Xu. Measurement of single-molecule resistance by repeated formation of molecular junctions. *Science*, 301(5637):1221–1223, August 2003.

[84] Young-Woo Son, Marvin L. Cohen, and Steven G. Louie. Energy Gaps in Graphene Nanoribbons. *Physical Review Letters*, 97(21), November 2006.

[85] Bhagawan Sahu, Hongki Min, and Sanjay K. Banerjee. Edge saturation effects on the magnetism and band gaps in multilayer graphene ribbons and flakes. *Physical Review B*, 84(7), August 2011.

[86] Alejandro Lopez-Bezanilla, Jingsong Huang, Humberto Terrones, and Bobby G. Sumpter. Boron nitride nanoribbons become metallic. *Nano Letters*, 11(8):3267–3273, August 2011.

[87] L. Pisani, J. Chan, B. Montanari, and N. Harrison. Electronic structure and magnetic properties of graphitic ribbons. *Physical Review B*, 75(6), February 2007.

[88] Young-Woo Son, Marvin L. Cohen, and Steven G. Louie. Half-metallic graphene nanoribbons. *Nature*, 444(7117):347–349, November 2006.

[89] Jun Nakamura, Toshihiro Nitta, and Akiko Natori. Electronic and magnetic properties of bnc ribbons. *Phys. Rev. B*, 72:205429, Nov 2005.

[90] Veronica Barone and Juan E. Peralta. Magnetic boron nitride nanoribbons with tunable electronic properties. *Nano Letters*, 8(8):2210–2214, August 2008.

[91] Fawei Zheng, Gang Zhou, Zhirong Liu, Jian Wu, Wenhui Duan, Bing-Lin Gu, and S. Zhang. Half metallicity along the edge of zigzag boron nitride nanoribbons. *Physical Review B*, 78(20), November 2008.

[92] Sudipta Dutta and Swapan K. Pati. Novel properties of graphene nanoribbons: a review. *Journal of Materials Chemistry*, 20(38):8207, 2010.

[93] Yi Lin and John W. Connell. Advances in 2d boron nitride nanostructures: nanosheets, nanoribbons, nanomeshes, and hybrids with graphene. *Nanoscale*, 4(22):6908, 2012.

[94] Simon Mutien-Marie Dubois, Xavier Declerck, J.-C. Charlier, and Michael C. Payne. Spin filtering and magneto-resistive effect at the graphene/ h -BN ribbon interface. *ACS Nano*, 7(5):4578–4585, May 2013.

[95] Paulo V. C. Medeiros, G. K. Gueorguiev, and S. Stafström. Benzene, coronene, and circumcoronene adsorbed on gold, and a gold cluster adsorbed on graphene: Structural and electronic properties. *Physical Review B*, 85(20), May 2012.

[96] B. Aradi, B. Hourahine, and Th. Frauenheim. DFTB+, a Sparse Matrix-Based Implementation of the DFTB Method †. *The Journal of Physical Chemistry A*, 111(26):5678–5684, July 2007.

[97] Marcus Elstner, Dirk Porezag, G. Jungnickel, J. Elsner, M. Haugk, Th Frauenheim, Sandor Suhai, and Gotthard Seifert. Self-consistent-charge density-functional tight-binding method for simulations of complex materials properties. *Physical Review B*, 58(11):7260, 1998.

[98] J. Frenzel, A. F. Oliveira, N. Jardillier, T. Heine, and G. Seifert. Semi-relativistic, self-consistent charge slater-koster tables for density-functional based tight-binding (dftb) for materials science simulations. *TU-Dresden*, 2004-2009.

[99] Hendrik J. Monkhorst and James D. Pack. Special points for brillouin-zone integrations. *Phys. Rev. B*, 13:5188–5192, Jun 1976.

[100] Eduardo Costa Girão and Vincent Meunier. Patchwork algorithm for the parallel computation of the green's function in open systems. *Journal of Computational Electronics*, 12(2):123–133, June 2013.

[101] Eduardo Costa Girão, Eduardo Cruz-Silva, and Vincent Meunier. Electronic Transport Properties of Assembled Carbon Nanoribbons. *ACS Nano*, 6(7):6483–6491, July 2012.

[102] Horacio M. Pastawski. Classical and quantum transport from generalized landauer-büttiker equations. *Physical Review B*, 44(12):6329, 1991.

[103] C. Caroli, Ro Combescot, Ph Nozieres, and D. Saint-James. Direct calculation of the tunneling current. *Journal of Physics C: Solid State Physics*, 4(8):916, 1971.

[104] S. Datta. Quantum transport: Atom to transistor. *Cambridge University Press, Cambridge*, July 2005.

[105] K. Kazymyrenko and X. Waintal. Knitting algorithm for calculating green functions in quantum systems. *Phys. Rev. B*, 77:115119, Mar 2008.

[106] Shuichi Nosé. A unified formulation of the constant temperature molecular dynamics methods. *The Journal of Chemical Physics*, 81(1):511, 1984.

[107] Young-Woo Son, Marvin L. Cohen, and Steven G. Louie. Energy gaps in graphene nanoribbons. *Physical Review Letters*, 97(21), November 2006.

[108] E. Cruz-Silva, Z. M. Barnett, B. G. Sumpter, and V. Meunier. Structural, magnetic, and transport properties of substitutionally doped graphene nanoribbons from first principles. *Physical Review B*, 83(15), April 2011.

[109] Shilong Li, Zhaoyu Ren, Jiming Zheng, Yixuan Zhou, Yun Wan, and Ling Hao. Band gap engineering of graphene/h-BN hybrid superlattices nanoribbons. *Journal of Applied Physics*, 113(3):033703, 2013.

[110] Prashant P. Shinde and Vijay Kumar. Direct band gap opening in graphene by BN doping: *Ab initio* calculations. *Physical Review B*, 84(12), September 2011.

[111] Marcos G. Menezes and Rodrigo B. Capaz. Half-metallicity induced by charge injection in hexagonal boron nitride clusters embedded in graphene. *Physical Review B*, 86(19), November 2012.

[112] Oleg V. Yazyev and Alfredo Pasquarello. Magnetoresistive junctions based on epitaxial graphene and hexagonal boron nitride. *Physical Review B*, 80(3), July 2009.

[113] V. M. Karpan, P. A. Khomyakov, G. Giovannetti, A. A. Starikov, and P. J. Kelly. Ni(111) | graphene | h -BN junctions as ideal spin injectors. *Physical Review B*, 84(15), October 2011.

[114] Y. Taur. Cmos design near the limit of scaling. *IBM Journal of Research and Development*, 46(2.3):213–222, March 2002.

[115] Hui Fang, Steven Chuang, Ting Chia Chang, Kuniharu Takei, Toshitake Takahashi, and Ali Javey. High-performance single layered wse2 p-fets with chemically doped contacts. *Nano Letters*, 12(7):3788–3792, 2012. PMID: 22697053.

[116] K. S. Novoselov, A. K. Geim, S. V. Morozov, D. Jiang, Y. Zhang, S. V. Dubonos, I. V. Grigorieva, and A. A. Firsov. Electric field effect in atomically thin carbon films. *Science*, 306(5696):666–669, October 2004.

[117] Qing Hua Wang, Kourosh Kalantar-Zadeh, Andras Kis, Jonathan N. Coleman, and Michael S. Strano. Electronics and optoelectronics of two-dimensional transition metal dichalcogenides. *Nature Nanotechnology*, 7(11):699–712, November 2012.

[118] Manish Chhowalla, Hyeon Suk Shin, Goki Eda, Lain-Jong Li, Kian Ping Loh, and Hua Zhang. The chemistry of two-dimensional layered transition metal dichalcogenide nanosheets. *Nature Chemistry*, 5(4):263–275, March 2013.

[119] Nourdine Zibouche, Agnieszka Kuc, Janice Musfeldt, and Thomas Heine. Transition-metal dichalcogenides for spintronic applications. *Annalen der Physik*, 526(9-10):395–401, 2014.

[120] Z. Y. Zhu, Y. C. Cheng, and U. Schwingenschlögl. Giant spin-orbit-induced spin splitting in two-dimensional transition-metal dichalcogenide semiconductors. *Phys. Rev. B*, 84:153402, Oct 2011.

[121] Andrea Splendiani, Liang Sun, Yuanbo Zhang, Tianshu Li, Jonghwan Kim, Chi-Yung Chim, Giulia Galli, and Feng Wang. Emerging Photoluminescence in Monolayer MoS $_2$. *Nano Letters*, 10(4):1271–1275, April 2010.

[122] Wencan Jin, Po-Chun Yeh, Nader Zaki, Datong Zhang, Jerzy T. Sadowski, Abdullah Al-Mahboob, Arend M. van der Zande, Daniel A. Chenet, Jerry I. Dadap, Irving P. Herman, Peter Sutter, James Hone, and Richard M. Osgood. Direct measurement of the thickness-dependent electronic band structure of mos_2 using angle-resolved photoemission spectroscopy. *Phys. Rev. Lett.*, 111:106801, Sep 2013.

[123] Ajit Srivastava, Meinrad Sidler, Adrien V. Allain, Dominik S. Lembke, Andras Kis, and A. Imamoglu. Valley zeeman effect in elementary optical excitations of monolayer wse2. *Nat Phys*, 11(2):141–147, Feb 2015. Letter.

[124] Ajit Srivastava, Meinrad Sidler, Adrien V. Allain, Dominik S. Lembke, Andras Kis, and A. Imamoğlu. Optically active quantum dots in monolayer WSe2. *Nature nanotechnology*, 10(6):491–496, 2015.

[125] J. M. Riley, F. Mazzola, M. Dendzik, M. Michiardi, T. Takayama, L. Bawden, C. Granerod, M. Leandersson, T. Balasubramanian, M. Hoesch, T. K. Kim, H. Takagi, W. Meevasana, Ph Hofmann, M. S. Bahramy, J. W. Wells, and P. D. C. King. Direct observation of spin-polarized bulk bands in an inversion-symmetric semiconductor. *Nat Phys*, 10(11):835–839, Nov 2014. Letter.

[126] Yuan Huang, Jing Wu, Xiangfan Xu, Yuda Ho, Guangxin Ni, Qiang Zou, Gavin Kok Wai Koon, Weijie Zhao, A. H. Castro Neto, Goki Eda, Chengmin Shen, and Barbaros Özyilmaz. An innovative way of etching MoS2: Characterization and mechanistic investigation. *Nano Research*, 6(3):200–207, March 2013.

[127] Xiaofei Liu, Tao Xu, Xing Wu, Zhuhua Zhang, Jin Yu, Hao Qiu, Jin-Hua Hong, Chuan-Hong Jin, Ji-Xue Li, Xin-Ran Wang, Li-Tao Sun, and Wanlin Guo. Top-down fabrication of sub-nanometre semiconducting nanoribbons derived from molybdenum disulfide sheets. *Nat Commun*, 4:1776, Apr 2013. Article.

[128] B. Radisavljevic, A. Radenovic, J. Brivio, V. Giacometti, and A. Kis. Single-layer MoS2 transistors. *Nature Nanotechnology*, 6(3):147–150, March 2011.

[129] Zongyou Yin, Hai Li, Hong Li, Lin Jiang, Yumeng Shi, Yinghui Sun, Gang Lu, Qing Zhang, Xiaodong Chen, and Hua Zhang. Single-layer mos2 phototransistors. *ACS Nano*, 6(1):74–80, 2012. PMID: 22165908.

[130] Wei Liu, Jiahao Kang, Deblina Sarkar, Yasin Khatami, Debdeep Jena, and Kaustav Banerjee. Role of metal contacts in designing high-performance monolayer n-type wse2 field effect transistors. *Nano Letters*, 13(5):1983–1990, 2013. PMID: 23527483.

[131] Jinhua Hong, Zhixin Hu, Matt Probert, Kun Li, Danhui Lv, Xinan Yang, Lin Gu, Nannan Mao, Qingliang Feng, Liming Xie, Jin Zhang, Dianzhong Wu, Zhiyong Zhang, Chuanhong Jin, Wei Ji, Xixiang Zhang, Jun Yuan, and Ze Zhang. Exploring atomic defects in molybdenum disulphide monolayers. *Nat Commun*, 6:6293, Feb 2015. Article.

[132] J. C. Slater and G. F. Koster. Simplified lcao method for the periodic potential problem. *Phys. Rev.*, 94:1498–1524, Jun 1954.

[133] Ferdows Zahid, Lei Liu, Yu Zhu, Jian Wang, and Hong Guo. A generic tight-binding model for monolayer, bilayer and bulk MoS2. *AIP Advances*, 3(5):052111, 2013.

[134] Yafei Li, Zhen Zhou, Shengbai Zhang, and Zhongfang Chen. MoS $_2$ Nanoribbons: High Stability and Unusual Electronic and Magnetic Properties. *Journal of the American Chemical Society*, 130(49):16739–16744, December 2008.

[135] Javier Junquera, Óscar Paz, Daniel Sánchez-Portal, and Emilio Artacho. Numerical atomic orbitals for linear-scaling calculations. *Phys. Rev. B*, 64:235111, Nov 2001.

[136] Hendrik J. Monkhorst and James D. Pack. Special points for brillouin-zone integrations. *Phys. Rev. B*, 13:5188–5192, Jun 1976.

[137] Kin Fai Mak, Changgu Lee, James Hone, Jie Shan, and Tony F. Heinz. Atomically thin mos_2: A new direct-gap semiconductor. *Phys. Rev. Lett.*, 105:136805, Sep 2010.

[138] John P. Perdew. Density functional theory and the band gap problem. *International Journal of Quantum Chemistry*, 28(S19):497–523, 1985.

[139] Meng-Lin Tsai, Sheng-Han Su, Jan-Kai Chang, Dung-Sheng Tsai, Chang-Hsiao Chen, Chih-I Wu, Lain-Jong Li, Lih-Juann Chen, and Jr-Hau He. Monolayer MoS $_2$ Heterojunction Solar Cells. *ACS Nano*, 8(8):8317–8322, August 2014.

[140] L. Z. Hao, W. Gao, Y. J. Liu, Z. D. Han, Q. Z. Xue, W. Y. Guo, J. Zhu, and Y. R. Li. High-performance n-MoS $_2$ /i-SiO $_2$ /p-Si heterojunction solar cells. *Nanoscale*, 7(18):8304–8308, 2015.

[141] Li Peng, Kailun Yao, Sicong Zhu, Yun Ni, Fengxia Zu, Shuling Wang, Bin Guo, and Yong Tian. Spin transport properties of partially edge-hydrogenated MoS2 nanoribbon heterostructure. *Journal of Applied Physics*, 115(22):223705, June 2014.